University Mohamed Boudiaf-M'sila

FACULTY OF TECHNOLOGY

DEPARTEMENT OF MECHANICAL ENGINEERING

Serial number :.....

Registration number :.....

Thesis

Presented for obtaining the diploma of

LMD DOCTORATE

Sector: Mechanical Engineering

Specialty: mechanical construction

THEME

Contribution to the dynamic study of a rotor by finite elements

Presented by:

AIMEUR Noureddine

Supported on: ../../..

Examining Committee Members:

Moussa Zaoui	Professor	Univ of M'sila	President
Noureddine Menasri	Professor	Univ of M'Sila	advisor
Salah Amroune	Professor	Univ of M'Sila	Examiner
Farsi Chouki	MCA	Univ of Msila	Examiner
Ahmed Chellil	Professor	Univ of Boumerdes	Examiner
Noureddine Chikh	MCA	Univ of Bordj Bou Arreridj	Examiner

Academic year 2023-2024

Acknowledgments

Completing this doctoral thesis has been a journey of personal and academic growth, continuous learning, and discovery. I would like to thank those who made this endeavor possible, especially the advisors of **Prof. Noureddine Menasri,** for their unwavering support and guidance, which contributed significantly to shaping this research. And I was lucky that I worked under his supervision. His dedication throughout this journey was irreplaceable.

I express sincere thanks to **Mr. Zaoui Moussa**, a professor at the University of M'sila, for graciously agreeing to preside over the thesis committee. My gratitude also extends to **Mr. Amroune Salah,** a professor at the University of M'sila, **Mr. Farsi Chouki** a professor at the University of M'sila, for his willingness to evaluate this work, and to **Mr. Chellil Ahmed**, Professor at the University of Boumerdes, for his willingness to evaluate this work, and **Mr. Chikh Noureddine**, Professor at the Univ of Bordj Bou Arreridj, for his thoughtful assessment of the research.

I value the academic environment and collaborative opportunities provided by my colleagues and fellow researchers at the University of M'sila. Their support has been crucial in the development of this research.

I am especially grateful to my family for their constant encouragement. Their unwavering support has been my mainstay through the challenges of this academic journey. I also thank all my friends from near and far for their support and encouragement.

Contents

List of Figures

List of Tables

Nomenclature

T	Kinetic energy
U	Strain energy
δW	Virtual Works
$\dot{q}_i$	Generalized coordinate
$\dot{F}_i$	Generalized forces vector
Ω	Rotational speed
(x_g, y_g, z_g)	Galilean coordinate system
(x, y, z)	referent local coordinate system
ρ	Density
E	Young Module
ν	Poisson's ratio
K	Stiffness
C	Damping
M_D	Mass of disk
M_s	Mass of shaft
m_u	Mass unbalance
T_D	Kinetic energy of the disk
T_s	Kinetic energy of the shaft
T_u	Kinetic energy of the mass unbalance
$(\{u\}, \{w\})$	Displacement vector
$\{\dot{u}\}, \{\dot{w}\}$	Speed vector
$\{\ddot{u}\}, \{\ddot{w}\}$	Accelerations vector
$\{\theta\}$	Angular displacement
$[M]$	Matrix matrix
$[C]$	Damping matrix
$[B]$	Rotating damping matrix
$[C_cori]$	Coriolis matrix
$[K]$	Stiffness matrix
$[K_spin]$	Spin softening matrix
$[C_gyro]$	Gyroscopic matrix
$[H]$	Circulatory matrix
$\{f\}$	External force vector

General introduction

Structural dynamics holds an important position in the field of scientific research today. Among its branches is rotary structural dynamics, which is a specialized field within mechanics focusing on the study of the dynamic and vibration behavior of rotating structures. The study of the dynamic behavior of rotating machines and various mechanical structures, such as centrifuges, pumps, compressors, turbines, and wind turbines, makes it possible to solve problems related to the operation of rotating machines. Rotating machines are defined as any element that rotates around a fixed axis.

For example, geostationary satellites are powered by free rotation according to the definition of rotors, these rotors are called free rotors, as opposed to fixed rotors supported by bearings. Stationary rotors are found in many areas: aviation, automotive, nuclear, or even the oil industry. In our study, we will focus on stationary rotors, more precisely on those with a horizontal axis.

The main purpose of rotors is to convert the power pattern according to their intended applications. They usually consist of several sections and are exposed to different pressures; however, current trends aim to research and develop lighter and therefore more flexible cycles in order to reach very high speeds by reducing the ratio of power and weight and controlling the balance of operating speeds, as well as reducing the clearance of the stationary and rotating parts for better service life and reliability. The rotor shaft is also considered a continuous body with inertia and mass characteristics distributed along its length, especially at very high speeds, so different types of vibrations appear and often limit performance and endanger the safety of operation, so dynamic analysis of continuous rotary machines is necessary to ensure proper operation of rotary machines.

To study the behavior of the dynamics of the rotor, it is possible to write the equations of motion either in a rotating frame of reference, where it rotates at the same rotational speed as the rotor, or in a fixed frame of reference, which was used in this thesis because it is the most appropriate. Euler angles are used to describe the motion of the rotating element in the equation of motion. These equations include many nonlinearities. For dynamic studies of vertigo, the small displacement hypothesis is conventionally advanced. It is assumed that the rotational speed is constant, which allows for obtaining linear equations of motion.

The basic studies of the dynamics of rotors related to the Campbell diagram, which represents the evolution of natural frequencies as a function of rotational speed, and the calculation of unbalanced responses are mainly focused, especially during critical speeds.

To conduct such studies, various modeling tools are available, including the transfer matrix method, the finite element method, the generalized polynomial expansion method, and distributed transfer functions. These methods allow us to consider the unique properties of rotary dynamics compared to stationary structures, such as the presence of gyroscopic moments responsible for the natural frequency change based on rotational speed.

Problems

The fan centrifugal draft cement is face to many diverse problems, including vibrations, various mechanical problems, and noise. Most of the common causes that lead to these problems are misalignment and bearing errors such as worn or defective bearings, lack of lubrication, and foundation problems that can lead to the transmission of vibrations from the rotating machine to the surrounding devices. An unbalance can lead to excessive vibrations that can cause a failure in the operation of the rotor. An unbalance occurs due to the accumulation of foreign substances. And the blades or the broken rotor, in addition to the wear of the components, as all cycles have a life span and eventually wear out over time.

Objective of thesis

There are many objective that can be achieved from studying the dynamic behavior of the rotor by finite elements. The main purpose of this thesis is to study the dynamic behavior of the FN280 centrifugal fan installed in the cement plant and study the effect of blade wear on the dynamic behavior.

In addition, a preliminary assessment was carried out on the effect of fluids on:

- Design of cement fan parts
- Perform numerical simulations of modal analysis and harmonic response analysis to predict natural frequencies and determine the rotor mode shapes.
- And to find the critical speeds, in or near the field of operating speed and the effect of the wear of the fan blades on these speeds.
- Development of numerical simulations FSI to estimate the aerodynamic forces on the fan and make a preliminary estimate of the fatigue limit and the life of the fan.
- Perform simulation transient analysis to calculate the deformations and stresses resulting from fluid pressure on the rotor over time.

Thesis Organization

The dissertation is divided into five chapters:

The first chapter

The first chapter of the thesis provides an overview of the development of technologies in the field of rotary dynamics based on biographic research. Summarizes the progress of scientific research and the knowledge gained from analytical models or finite elements. In this chapter, some important phenomena in rotor dynamics are described, along with the identification of the main important points. Some types of rotors have also been touched upon.

The second chapter

The chapter is devoted to mathematical modeling and the analysis of the dynamic behavior of rotors. The second section presents the development of finite element modeling, where procedures and means were presented for a thorough study of the analysis of the dynamic and vibrational behavior of columns or rotating systems, with an example of a model to show the general matrix. In the assembly of the rotating system, mathematical models were developed using both Euler beam theories and Reynolds equations.

The third chapter

This chapter provides a brief description of the rotor model to be studied, represented by the FN 208 centrifugal fan installed in the cement plant, and presents most of the fan parts designed using the SOLIDWORKS SOFTWAR 2022. A general description of the reverse engineering technique that was used to create a CAD model of the fan blade was also provided due to the lack of design data for it and the inability to take measurements manually for its complexity, so reverse engineering was used as an analysis of the validity of the model that was built using the GEOMAGIC CONTROL X program.

Fourth chapter

In Chapter Fourth, a numerical simulation is presented to study the behavior of dynamic analysis of the FN280 centrifugal fan using the Ansys 2022 Workbench program, which uses the finite element method to calculate natural frequencies, mode shapes, pressures, and vibration responses due to imbalance or external excitation. An overview of some possible types of analysis of rotor dynamics was also discussed, and the chapter also presented the effect of worn blades as a result of wear on critical speeds. Finally, we conclude by clarifying some results specific to each simulation.

The fifth chapter

In this chapter, the simulation workflow is explained, and an overview is given of the simulation of the structure of liquids using the ANSYS Workbench 2023 program, the methods of solving these simulations, and the operating conditions applied to the fan. The FN280 centrifugal fan and the computational domain of liquids associated with it are also described.

In addition, detailed descriptions of the structural and fluid simulations were discussed. The procedure for transferring data between the liquid and solid domains was

determined. The simulation results were presented and explained. They are divided into the results of finite element analysis and the results of computational fluid dynamics (CFD).

CHAPTER I

Bibliographic Research

Contents

I.1 Introduction

Since we are going to be interested in the dynamic behavior of rotating machines, it is appropriate to start introducing this category. Rotor dynamics is a branch of system dynamics that deals with mechanical machines where there is at least one part rotating around a fixed axis by means of cylindrical bearings or hinges that allow it to rotate freely [1]. Its rotational motions are characterized by certain phenomena, and they require an external power supply provided by the engine. Figure I.1 shows the basic components of the rotary machines.

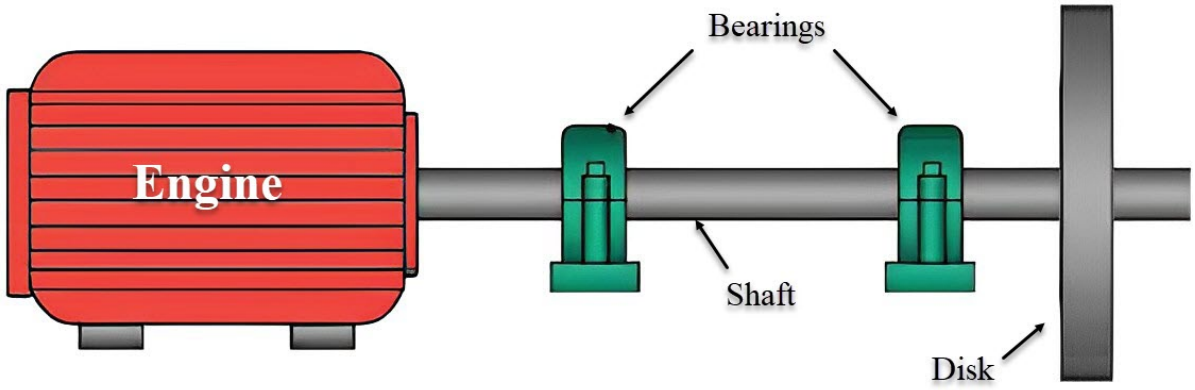

Figure I.1: Basic components of a rotating machine

There are different types of rotating machines that we find in different industry sectors, and they differ in size, complexity, and general configuration according to the applications for which they are intended [2]. Basic rotating machines can be found in many systems and products, such as electric motors, gas turbines, and steam turbines. They also include centrifuges, vacuum pumps, and helicopters. Figure I.2 shows examples of some rotating machines.

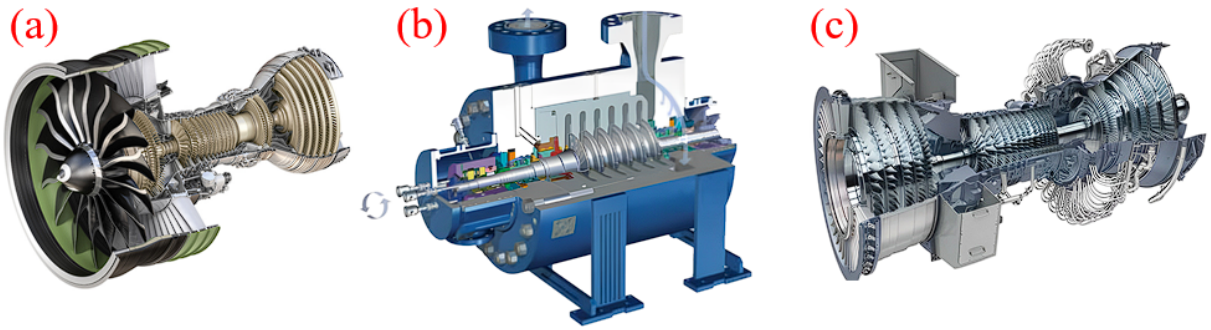

Figure I.2: Example of rotating machines (a) Turbojet [3], (b) Centrifugal compressors [4], (c) Gas turbine [5].

In recent decades, new problems have emerged due to the rapid increase in the operating speeds of rotating machines. The increase in the rotation speed has led to the exposure of the shafts to increased vibrations, which can be dangerous and have disastrous consequences if not handled well.

I.2 Background

Rotor dynamics is a field of mechanical focused on the study of the vibration behavior of axially symmetrical rotating structures. This includes systems using modern equipment, such as rotors in high-speed turbomachines. The term «rotors» refers to structures that rotate at high speeds around their axis. Rotors with high speeds can develop the phenomenon of resonance, causing excessive vibration that may lead to permanent failures and collisions with neighboring parts, causing irreparable damage. Therefore, determining the characteristics of rotational dynamics is extremely important. On the other hand, the history of rotor dynamics reveals the fundamental nature of the various problems encountered during the design and development of rotor systems, as well as clarifies phenomena that contradict intuition. The discrepancy between the simple conception of making the rotating part rotate steadily and smoothly on bearings and the reality of engineering challenges also appears. Balancing stability and dynamics is a big challenge, so knowing the history of this field is a source of inspiration and learning. Many authors have written about the history of rotor dynamics, we mention some of them: Hongrui Cao et al. [6], Matthew B. Wagner et all. [7], Cyrus B. Meher-Homji [8], and A.D. Dimarogonas [9].

The history of rotor dynamics begins in the second half of the nineteenth century, when the first problems encountered in rotor dynamics appeared, namely, the critical speed proposed by William John Macqueen Rankine. In 1869, Rankine published the first investigation of rotating machines [10]. In this article, the author tried to explain the behavior of rotating machines when exceeding the critical speed, in which the vibration caused by the unbalance of the moving part is amplified so that velocities higher than the critical speeds would be unstable, because of which he neglected the Coriolis in the model and considered the centrifugal force to be a reel force.

Due to Rankin's erroneous conclusions that confused engineers and caused the emergence of the philosophy of maintaining operating speeds below critical speeds, this philosophy was challenged by the experiments of the Swedish engineer Gustav Patrick De Laval at the end of the nineteenth century, who operated the first steam turbine of equal pressure with a rotation speed about seven times higher than the critical speed. He solved the equations experimentally, as it turned out the center of gravity of the disc folded inside after the resonance point [11], but this position is a constant direction of turbulence (Coriolis force ensure stability). at first be built a solid rotor but later used a flexible rotor and showed that it is possible to work above the critical speed, explained Stodola and Föppl [12], the only theoretical evidence that the supercritical flow is stable after a decade or several decades. It was at that point that the thinking of researches and designers of rotating machines was occupied by predicting critical speeds to avoid resonance. In 1894, Dunkerley [13] published an article in which he showed that the critical velocities of a regular rotor shaft on simple supports are the same as the natural frequencies of transverse vibration. He was the first to use the term «critical speed» for the speed of rotation of the resonance. He also gives a simple equation for calculating the minimum critical speed with a large amplitude and synchronous cycles.

In the first quarter of the twentieth century, many rotating machine failures were associated with vibrations that were occurring. The Royal Society of London commissioned Henry Homan Jeffcott to make an analysis of rotor rotation and critical speeds.

In 1919, Jeffcott [14] published a paper devoted entirely to rotor dynamics, where Jeffcott confirmed FÖPPL'S predictions of the existence of a stable state of the rotor and proposed a simple model known as the Jeffcott model, also sometimes known as the Laval-Vaupl Jeffcott model. Jeffcott's analysis also showed that synchronous rotation can be fluctuated by balancing the rotor, adding damping if it is close to the critical speeds, or operating at speeds above or below the critical speed. DeLaval and engineers conducted experiments and analyses on the design of rotating machines with flexible shafts for supercritical operation. However, this philosophy led to problems of dynamic instability at speeds above critical speeds, which are unrelated to the response to unbalance. In the twenties of the twentieth century, some rotating machines that were designed according to this philosophy (violent asynchronous rotation) were exposed. The frequency of rotation was so low that it could be seen with the naked eye that there was a problem with the oscillation of the shaft. The first to work on the problem were Newkirk and Kimball [15], where Kimball assumed the internal friction, or damping in the rotor [16], could produce internal moments at supercritical speeds that would push the rotor. Kimball published a paper in 1924 [17], in which he favored the vibrations of team turbines.

In 1933, D.M. Smith [18], published a research paper containing valid models of the rotor-bearing system, which included shaft elasticity, bearing support elasticity, and internal friction. The paper provided mathematical solutions to all the problems of basic rotational dynamics involving friction, particularly in self-excitation vibration, which caught the attention of researchers. Newkirk and Taylor [19], wrote an article titled «Shaft Whipping Due to Oil Action in Journal Bearings». Many researchers, such as S. Timoshenko [20], VV Bolotin [21], and Gunter EJ [22], have provided insights into the effects of physical damping on high-speed rotor performance. C. Hummel [23], and Newkirk confirmed through experimental studies the destabilizing rote caused by oil-film bearings. Specifically, when the bearing is light, the shaft is moved by a preset movement with a frequency close to half the rotational speed, while when the bearing is heavy, the system becomes stable again.

Torsional vibration is another type of rotor dynamics problem that causes early failures, especially in reciprocating-motor drive trains. In 1921, Holzer [24], published a thesis aimed at being able to pre-calculate the deviations of torsional of a given damping by finding an intelligent interactive method for solving the natural frequencies of torsional vibration without the use of matrices.

During the period, the bearings in almost all rotating machines were simple supports at the bearing locations (oil-lubricated cyclic bearings with a simple circular geometry). Because early researchers did not realize the importance of bearing properties, the common opinion was that the oil reduced the sliding fraction between the shaft and the bearing. After the Beauchamp Tower experiments on oil bearings and the accompanying theoretical development conducted by Osborne Reynolds [25], the importance of the bearings was gradually recognized. Reynolds produced a partial differential equation for oil pressure on a circular bearing that was impossible be solve (without computer), to solve this problem Sommerfeld and Harrison [26], using simplified assumptions were able to solve the pressure the produce the impact force on the shaft, the results from the point of view of bearing life were that the force can be large enough to support the load preventing metal-to-metal contact between the bearing and the shaft and from point of view rotary

dynamics the results was that the support force of the oil film is not in line with the deviation of the radial shaft from the axis of the bearing and this produces asynchronous instability at supercritical speeds now known as the oil whip before the oil cavity was identified, the integration of the pressure filed calculated by Robertson [27], produced a force that was completely normal for the radial determination of the shaft, this was the reason for his inaccurate predictions that the rotor would be unstable in asynchronous rotation at all speeds.

In the middle of the twentieth century, Horie succeeded in explaining the various basic characteristics of the oil whip. The name «oil-whip» spiral was associated with the problems of instability in oil bearings that were identified and analyzed for the first time throughout history. Additionally, other forms of rotor instability related to liquids were identified and reported. This means that oil, as a lubricant, is not solely responsible for rotor instability. Consequently, the word «oil» was replaced with the word «liquid», and other names for fluid bearing, such as «tourbillon», have recently become popular [28–31].

Currently, rotor dynamics is a very active field of research. Many researchers are working not only on linear rotor dynamics but also on nonlinear rotor dynamics at variable speeds and in the active control of rotating machines. In recent years, many researchers have conducted research and published many research papers in the field of the vibrational behavior of bearing-support cycles, which has led to the emergence of many developments and research results. Nan et al. [32], analyses the vibration properties of a horizontal machining center through the use of experimental model tests, which made it possible to obtain reliable model parameters and dynamic characteristics of the machining center. As done by Khan et al. [33], Khemari et al. [34], to confirm the natural frequencies and harmonic analysis that are used in drawing stress and deviation at critical speeds by performing a morphological analysis accordingly.

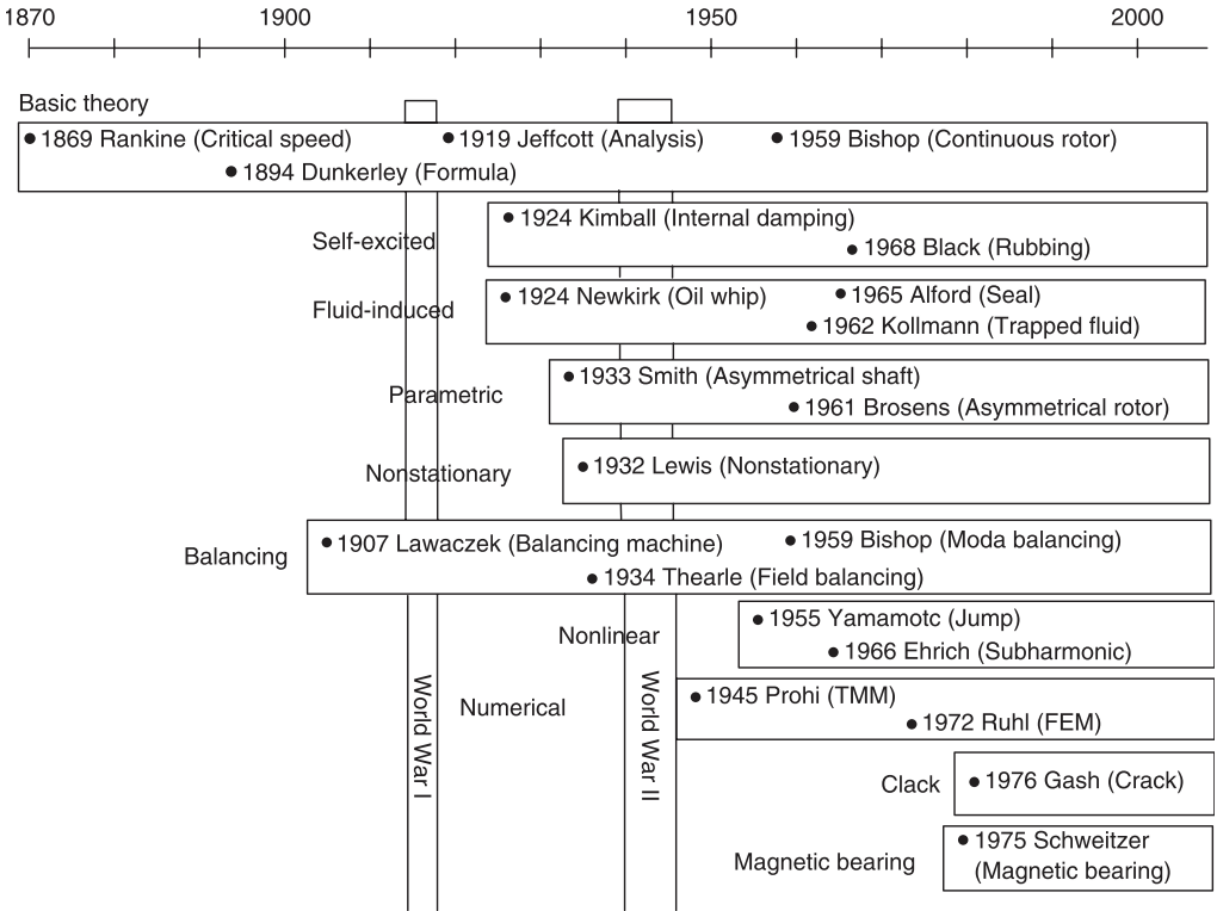

Figure I.3: History of rotor dynamics [35]

I.3 Classification of rotor systems

In the analysis of vibrations, the complex system is simplified and a suitable mathematical model is used. For this reason, the rotor can consist of shafts of different diameters and lengths, the bearings are located in different locations, and discs of different shapes are classified according to their characteristics as follows:

I.3.1 Rigid rotor

A rotor can be considered rigid if the curvature of the rotor shaft is negligible when it rotates at a speed well below the critical speed. The dynamic load is transmitted completely due to the fact that the rotating elements do not deform. Many researchers have studied this model. For example, the work done by Rui Yang et al. [36], verified the fault frequencies, resonance, and harmonic resonance by creating a rigid spherical bearing system. Han-Qing Guan et al. [37], verified the rotational properties of a solid rotor supported by an active protrusion type chip bearing (ABFB), and others studied the solid rotor [38–41].

I.3.2 Flexible rotor

The rotor is considered elastic when the rotor shaft is noticeably deformed when operating near or above the critical speed. The basic rule so that we can say that the rotor is flexible is if it is operating at 70% of the critical first speed or faster. By R. Siva Srinivas and other [42] presented a critical review of the literature on applications of magnetic-active bearing systems is dynamic rotor-elastic systems, and there are many studies of the rotor-elastic [43–48].

I.3.3 Free rotor

This rotor is unique among other models due to the lack of bearings, making it ideal for studying the dynamic behavior of geostationary missiles and satellites. P. Hughes [49], is considered one of the first researchers to study the dynamic behavior of this type of rotor. In the last decade, most research on this model has been conducted using numerical simulation methods. Due to the complexity of conducting experimental tests, the validity of the results is still being investigated.

I.3.4 The system of grouped

In some systems, the disk is considered solid, and the distributed mass of the flexible shaft is concentrated in the disk position. Such a system is called a system of grouped parameters.

I.3.5 Continuous rotor system

If the presence of an elastic rotor with distributed mass and rigidity is taken into account, then this model is called a distributed parameter system or a continuous rotor system.

I.3.6 Jeffcott rotor

In 1919, Jeffcott published a research paper in which he described the theory of unbalanced cycles, although it did not contain any reference to internal damping. He also explained the possibility of exceeding rotary machines for critical speeds [50]. However, the Jeffcott model cannot explain the properties of a rigid body on an elastic rotating shaft due to the representation of mass as a particle (point mass). [51].

The name Delaval and Jeffcott is still used as the name of the rotor model, and the Jeffcott rotor consists of a flexible shaft with negligible mass in order to neglect gyroscopic effects. The rotor is mounted on simple (rigid) bearings that allow it to rotate around the central axis of the shaft, in addition to a hard disc placed in the middle of the shaft extension. Also, in the presence of unbalance, its center of gravity does not coincide with the geometric center. Researchers use this model because it allows a more direct explanation of the influence of some phenomena on the dynamic behavior of the rotor [52–55]. Figure I.4 shows a Laval/Jeffcott rotor model.

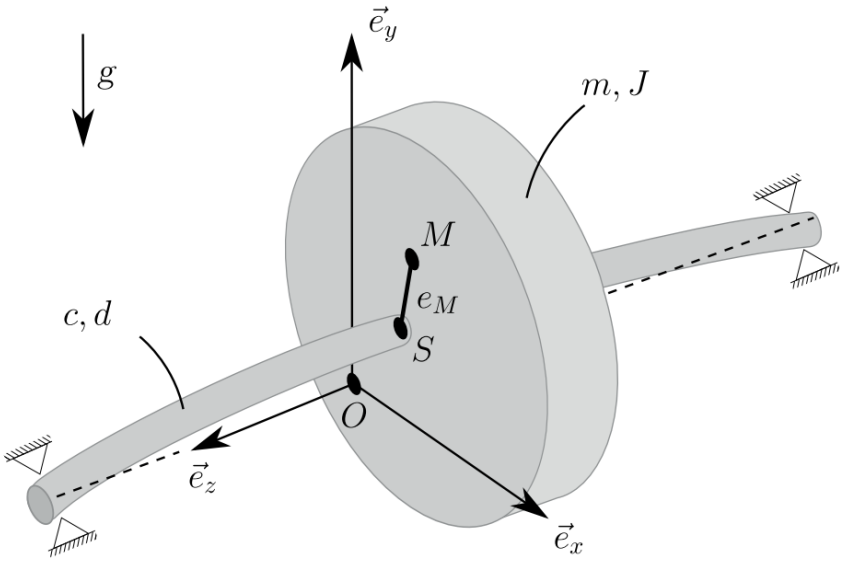

Figure I.4: Laval-Jeffcott rotor model [56]

I.4 Advantages of rotary machines

The dynamics of rotors are a special case of the dynamics of structure, even if there is a similarity in general, since rotating machines present some phenomena that are directly related to their rotational motion. The main difference is in the face that rotating machines represent continuous force, while in structures, they do not. Below we will address some important aspects of rotor dynamics.

I.4.1 Unbalance

An unbalance causes an excitation force (vibrational force) to be produced with a frequency directly proportional to the rotational speed, and it is assumed that all rotating machines have an unbalance. The excitation force is centrifugal force, it acts on the vibrational behavior in bending the rotor, and it becomes important at very high speeds, hence the importance of balancing the rotating machines and the reason for the appearance of unbalance [57].

- The difference between the center of mass and the center of rotation is a result of an uneven distribution around the geometric axis of the system.
- Deflection of the shaft is due to the weight of the moving part, resulting in an increase in the distance between the center of rotation and the center of mass.
- As a result of the rotation of the shaft around its center, fixed defects are amplified.
- Bearings that are not aligned with the geometric axis of the rotor.

I.4.2 Critical speed

The critical speed is defined as the speed at which the vibrations of the machine reach lage levels, which resembles the resonance of a non-rotating elastic structure [58]. This

definition dates back to one of the first quotations related to the concept of critical speed at the end of the nineteenth century while Dunkerley was conducting experimental tests, and at the moment the concept has developed in such a way that it can be linked to the concept of eigenvalues of a rotating system from a theoretical point of view: the critical speed corresponds to the speed at which the excitation due to unbalance coincides with one of the Eigen frequencies of the system. Critical speeds can also be called peak response speeds.

In 1996, the American Petroleum Institute published in the publication APIA the first edition, in which he defined the concept of critical speed as the speed of rotation of the shaft that corresponds to the peak of the resonance of the non-critical damper rotor (amplification factor >2.5). The location of the critical velocity frequency is defined as the frequency of the peak response to vibration as determined by the Bodé scheme (for unbalanced excitation) [59]. These special speeds correspond to the operating system that introduces the rotary machine into resonance. Resonance is defined as the natural frequency of the rotor, which may represent the risk of a malfunction associated with amplifying lateral vibrations, and this risk is increased by the presence of weak dampers in the rotor. In the absence of damping, rotary machines are designed to operate at speeds below the first critical speed, which we find in rotary machines supported by bearings of great rigidity, small size, and low mass.

I.4.3 Gyroscopic effect

The gyroscopic effect is an important term in rotary machines, and it is the one that distinguishes rotary dynamics from classical dynamics. The gyroscopic effect resulting from the rotational speed and the moment of inertial polar mass causes the coupling of displacements perpendicular to the axis of rotation, which leads to the division of each normal frequency of rotation into two frequencies: the direct mode (forward vortex FW) is direct when the direction of rotation of the rotor is the same as the direction of motion of the orbits, and the indirect mode (rear vortex BW) is direct when the direction of rotation of the rotor is opposite to the direction of motion of the orbit. see Figure I.5.

When the rotational speed increases, the gyroscopic effect strengthens the rotor stiffness of the front vortices and weakens the rear.

The gyroscopic coupling inherent in rotating structures induces the movement of the prefix. When the moment of inertia of the polar mass of the disc is greater than that of the shaft, the gyroscopic effect is especially prominent [60].

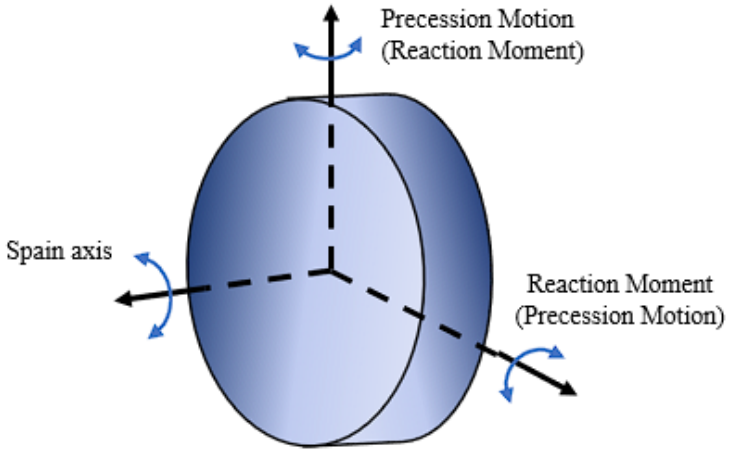

Figure I.5: Gyroscopic effect

I.4.4 Campbell's Diagram

The Campbell diagram is a graphical representation of the evolution of the natural frequencies of the rotating system as a function of the rotational speed and is plotted to predict the critical speeds of rotating machines. The rotation speed is plotted on the x-axis and the natural frequencies on the y-axis see Figure I.6.

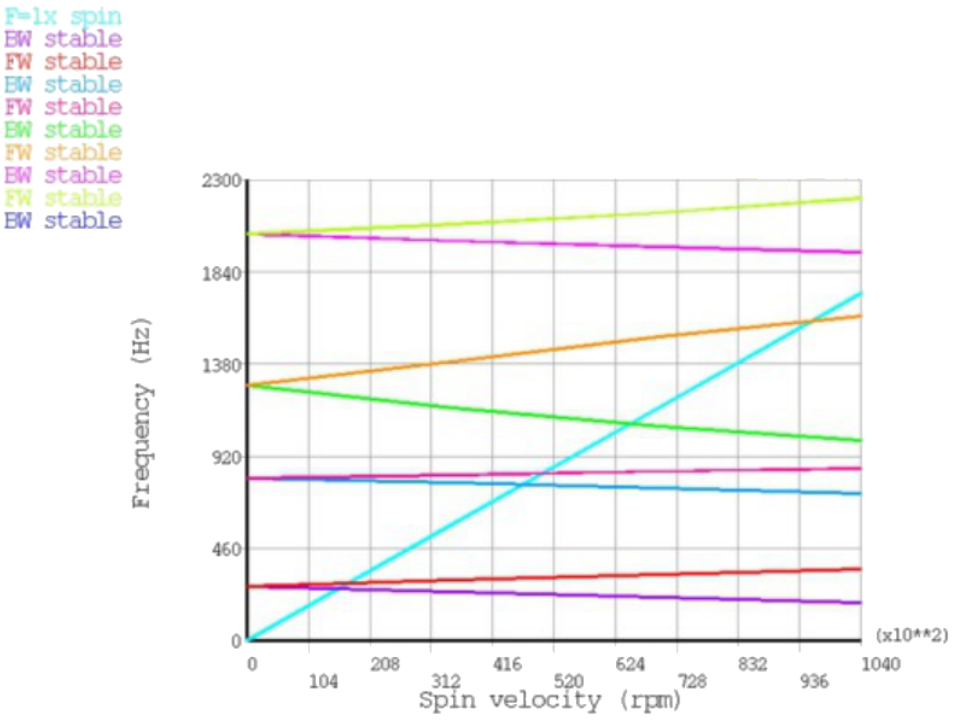

Figure I.6: Campbell Diagram [61]

Since the gyroscopic effects are proportional to the rotation speed, so the diagram represents the positions in the front and rear vortex, the difference between each mode pair is more important due to the importance of gyroscopic effects. In the Campbell diagram, an additional line called the main excitation line (the main excitations are the forces of simultaneous unbalance) can be seen, which enables us to detect the phenomena

of resonance, and the points of intersection of the line with lines of natural frequencies provide critical speeds.

I.4.5 Damping

Damping is the ability of the system to reduce the amplitude of the response to excitation from natural frequencies by dissipating the energy [62]. Negative damping leads to vibration instability, which should be avoided due the installation. One of the main difficulties in rotor dynamics in obtaining a large damping, and the damping of a rotor system is classified into two categories :

The first type is internal damping (rotary damping), which in some cases can lead to reducing the stability of the rotor, which is undesirable, which is the damping provided by the rotating part of the structure, and the second type is external damping, which serves to increase the critical speed somewhat and reduce the response to the stability of the system, which is the damping provided by bearings and coupling to the surrounding fluid and the fixed part of the structure, etc.

I.4.6 Mode shapes

The so-called mode shapes (vibration form) are a certain movement pattern followed by each natural frequency and refer to this for the movement of the components associated with the rotor when the structure begins to vibrate. The mode shapes help to visualize the rotor vibration at separate natural frequencies, for rotary systems the mode shapes are effects by a greater ratio of bearing stiffness of the shaft becomes less compared to the stiffness of the bearing, the bending contribution increases.

I.5 Rotor vibration

The rotor may tend to vibrate in any different directions and these vibrations can be classified depending on the direction of vibration and movement, they fall three types lateral vibration, torsional vibration and axial vibration.

I.5.1 Lateral rotor vibration

The vibration of the side rotor is also called transverse vibration. Lateral vibration can be considered the main reason for the failure of rotary machines. It is defined as an oscillation that occurs in the radial plane of the axis of rotation and as a result causes dynamic bending of the shaft in two mutually perpendicular lateral planes and the rotor can become unstable as the natural frequencies of lateral vibration are affected by the speed of rotation. Figure I.7 shows the direction of lateral vibration.

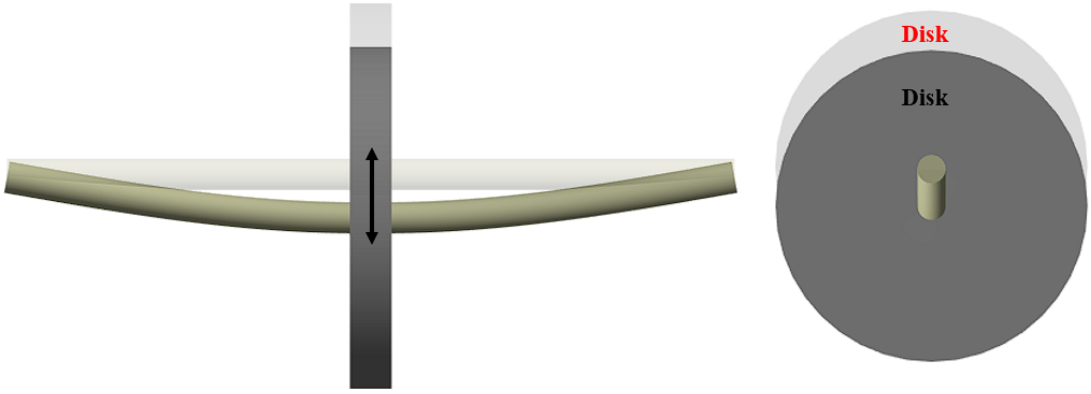

Figure I.7: Lateral vibration

N.A.Saeed and M.Kamel [63] publishing a research paper in which they proposed a device to control the lateral vibrations in the Jeffcott model by employing positive feedback. Additionally, Ali Alsaleh et all [64] explored the lateral vibrations both experimentally and theoretically for the unbalanced Jeffcoat rotor thet operates in many cases of non-compliance balance. Numerous other researchers have also studied the lateral vibrations of rotary machines [65–67]. However, when studying the balancing of the movable member, the effects often neglected, and less attention is given to other types of vibration. This woks also focuses on lateral vibrations.

I.5.2 Vibration of the torsional rotor

Torsional vibrations are a potential problem in very long rotors coupled with rigidity and are found in modern large steam turbines. They are known as angular vibratory torsion [62]. It can also be said to be the rotational motion of the rotating sections relative to each other around the axis of rotation, and there are researcher who have studied torsional vibrations. Chao Liu and Dongxiang Jiang [68] conducted a dynamic analysis and experimental study of a rotor system with inclined and transverse slits in order to simulate torsional oscillation in reality. Based on the characteristics of the lateral and torsional vibrations off the rotor, there are many studies on torsional vibration [69–71]. Figure I.8 shows the direction of torsional vibration.

Figure I.8: Torsional vibrations

I.5.3 Axial vibration

Vibration problems are not a potential problem. Axial vibration is defined as an oscillation that occurs along the axis of the rotor as a result of the compression of the moving part along the axis. Mutated studies are rare in scientific practice [72]. Hiroya Sugimoto et al. [73] have published a research paper in which they present a new method of damping axial vibration in permanent magnet motors that do not carry any magnets with two active positions. Figure I.9 shows the direction of Axial vibration.

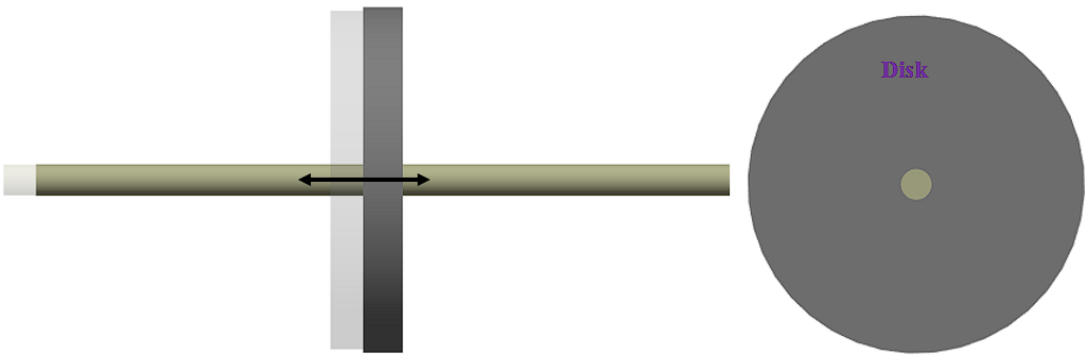

Figure I.9: Axial vibration

I.6 Bearing effect

due to the existence of a direct correlation between the rotating shaft and the bearing, the influence of the geometric and mechanical properties of the bearings on the dynamic behavior of rotors has been the subject of many researches for a long time, parameters that can determine the bearing characteristics, including the effect of asymmetry, bearing movement, nature and types of bearings, there are many bearings and each type differs on the other, but there are bearings that often store a target for researchers spherical bearings, thrust bearings, magnetic bearings and pressure film type damping.

I.6.1 Ball bearings

Ball bearings are used in many applications due to their low friction and their ability to withstand large transient overloads. Most researchers in the study of the dynamic behavior of a composite rotor rely on ball-type bearings, and due to the pressure of an internal clearance between the rolling elements and the races, this often shows a non-linear dynamic property hold [74]. The figure I.10 shows a photo of spherical roller bearings.

Explained by T. Yamamoto in an analytical study of the vibrational behavior of a rotor support on spherical bearings with radial clearance, the critical speed and vibration levels decrease when the value of the radial clearance increases [75].

Prashant H. Tain [76] explains the effects of radial summation, radial load, disc deflection, and rotor speed on the vibration amplitude and that radial load has a misleading effect on the vibration response of the rotor bearing system. Jean-Jacques Sinou and Fabric Thouverez [77] also conducted an experimental study of the effects of the temperature

of ball bearings on the rotor unbalance response and its effect on critical speeds. The results show that when the temperature of the rolling element bearing decreases, the first and rear critical speeds increase slightly.

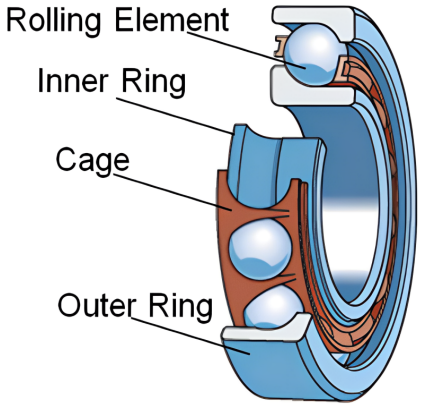

Figure I.10: Ball bearings [78]

I.6.2 Thrust bearings

The name of the thrust is given to axial load acting on the shaft, and the bearing that supports the thrust is called the Michell bearing or Kingsbury bearing. Thrust bearings were invented as an application of theory of hydrodynamic lubrication [79]. These bearings are adapted to withstand relatively high stresses between friction surface [80]. They are also used to support axial vibrations in rotary machines and widely in turbine machines to support axial loads [81]. Confirm S. Berger and colleagus [82] on the fact that the addition of a thrust bearing provides additional rigidity and additional damping of the moving part in addition to increasing the first critical speed and leading to a deduction in rotational capacity, as S. emphasized.Berger stressed the need to take into account the axial vibrations of the shaft. Zhang Yuanchao et al. [83] also carried out an analytical study of the existing difficulties in controlling the vibration of the thrust bearing.

Figure I.11: Thrust bearings [83]

I.6.3 Magnetic bearing

Magnetic bearing are used in many rotary machines that rotate at very high speeds and high temperature, such as turbochargers, the aviation industry in particular was interested in applying magnetic bearings to jet turbine engines due to the disposal of the oil tank,... etc [84], and with special and increasing demands with bearings used today such as ball bearing... [85] , magnetic bearing technology has opened up new possibilities for the design of rotating machines and represents an alternative solution to conventional bearings due to its advantages, there are also disadvantages, some disadvantages are increased cost and weight compared to other types of bearings and there are problems associated with the behavior of the landing as well as complexity [86]. There are four main categories, namely

- Permanent Magnetic Bearing (PMB).
- Active magnetic bearing (AMB).
- Superconducting bearing (SCB).
- Electrodynamics Bearing (EDB)

Take up Steven Marx and C. Nataraj [87]. Rotary systems suffering from harmonic base excitation on magnetic bearings were controlled by choosing to reduce the performance index. The results showed that by applying the control, the vibration of the rotating shaft was reduced to amplitudes much less than the amplitude of the disturbance. I.Arredondo [88] performed a modeling operation and controlled a rotating shaft that was lifted through magnetic bearings.

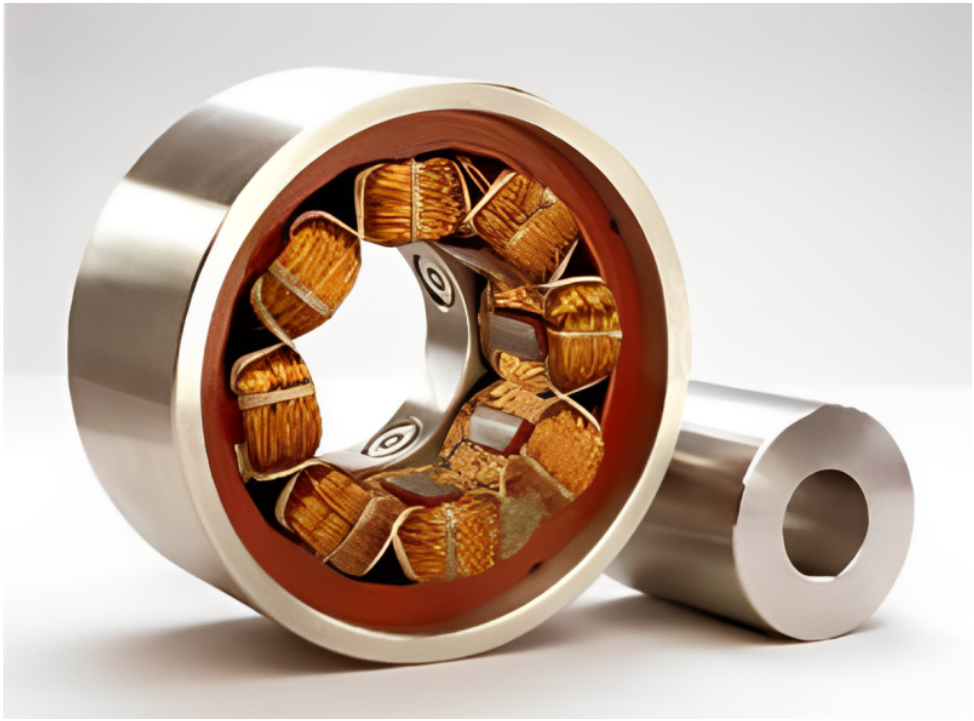

Figure I.12: Magnetic Bearings [89]

I.6.4 Pneumatic bearings

In the past decades, aerodynamics bearings (air and gas) have received increasing attention, and we find them in applications the require low loads, accuracy, and high speeds. They also have several advantages. They are insensitive to high temperatures, have low speeds, and also have disadvantages such as design and manufacturing problems and instability of rotor movements. B. bou-Saïd et al. [90] conducted a simulation to analyze the dynamic behavior of a rotor of a vehicle with pneumatic bearings by using nonlinear time-dependent calculations.

I.7 The digital aspect

in light of the great progress in computer technologies, it that become necessary to analyze the dynamic behavior of rotating machines using digital techniques, and most often two methods are used for the dynamic analysis of the rotor the element method and the transfer Matrix method.

Finite elements method (FEM)

The FEM is a numerical method used to solve difficult problems that we cannot solve analytically. The method is based on the decomposition of complex geometry into a number of simple geometric forms, assuming that each simple geometric form behaves as a continuous structural member [91]. Alexander Hrinkov and Richard Courant are considered the founders of the FEM regardless of priority, and both are credited with the beginnings of modern FEM For structure.

The impact of the appearance of the FEM on the field of dynamics of structures in general and rotary Dynamics was that at first the method could not be used due to the lack of gyroscopic effects, but later the gyroscopic Matrix was taken into account. Nelson and McVaugh [92] published the first works using the type of modeling, where a procedure for dynamic modeling of rotor bearing systems was introduced, confirming the development and reliability of the method.

Transfer matrix method

The Transfer matrix method was originally developed based on methods of dynamic analysis proposed by Hoizer (1921) [94], and Myklestad (1944) [95], to calculate the natural frequencies and self-forms of a rotor in a critical situation. The advantage of this method is its simplicity. Since this tabular method can be implemented by inexperienced calculators, it does not require storing and processing large system matrices. Introduced in 1967, W. Lund performed a procedure using this method to analyze the behavior of rotor dynamics [96].

I.8 Conclusion

the history of the dynamics of rotary machines has been studied, in addition to reminders and definitions of the basic concepts related to rotors, in order to give a broad vision to the work done. Various important works of researchers on various phenomena and

problems related to rotor dynamics and their properties have been mentioned. A number of instabilities that can arise due to rotation have been shown.

CHAPTER II

Modeling of rotor systems

Contents

II.1 Introduction

The development of equations of motion is necessary for predicting the dynamic behavior and stability of objects. In this chapter, we will describe the aspects of dynamic modeling for bodies and further develop these concepts to create equations of motion for rotors. This will enable us to predict their dynamic behavior and stability using Lagrange's equation. To create a model suitable for simple cases, we employed the Rayleigh-Ritz method. Additionally, this method helps to elucidate fundamental phenomena and their treatment within the system. To address more complex scenarios, a finite element model was formulated. Due to the intricacies of the problem, the finite element model stands out as the most effective mathematical approach, allowing us to determine the system's properties.

II.2 Methodology and Modeling Assumptions

The rotor generally consists of several elements of the shaft and bearings on which the shaft depends, also consists of one or several discs, and also involves an imbalance or other source of external forces. Figure II.1. The presence of inevitable imperfections can lead to the excitation of disturbing forces during rotation. These imperfections are inconsistencies that cannot be avoided and may have mechanical or thermal origins. They must be taken into account in the modeling process. Each rotor component requires specific modeling, which is then integrated into the overall rotor modeling [97].

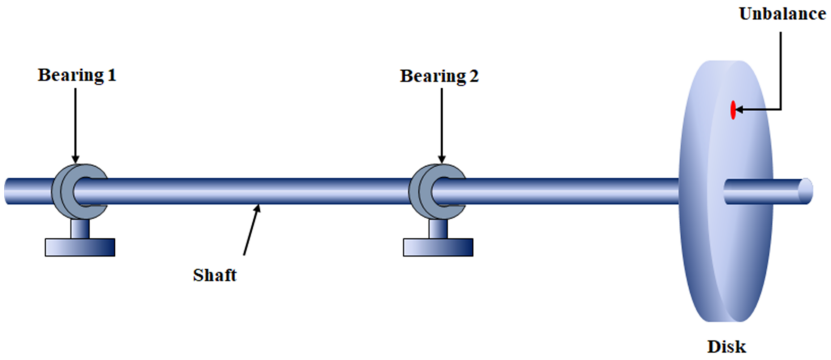

Figure II.1: Example of a single-rotor

Before embarking on the dynamic modeling of the rotor, the key steps involve defining the modeling assumptions. Clear delineation of these assumptions is crucial as it allows users to have a good understanding of the application limits for obtaining a simulation. The following assumptions are accepted for rotor modeling:

- The shift is flexible (Deformable).
- The disk is rigid.
- The rotor rotates at a constant speed Ω.
- The possible asymmetries of the shaft and the disks are not considered.

The assumptions are in line with the majority of industrial rotors. when the disk is flexible, rapid changes in velocity can lead to specific developments that have not been

addressed in this study.

Expressions of kinetic energies are necessary. In addition, the hypothetical action of forces due to bearings is calculated [98].
The general rotor equations are obtained by following the following steps:

- Calculation of the kinetic energy T of all elements.
- Calculation of the strain energy U for the shaft.
- Calculation of the working default W for the forces due to bearings in order to make the determination of generalized forces possible.
- Use Lagrange equations to obtain the equations of motion.

Either:

$$\frac{d}{dt}\left(\frac{\partial T}{\partial \dot{q}_i}\right) - \frac{\partial T}{\partial q_i} + \frac{\partial U}{\partial q_i} = F_i \tag{II.1}$$

$N\,(1 \leq i \leq N)$: Represents the number of degrees of freedom.
$\dot{q}_i$: are the independent generalized coordinates.

$\dot{F}_i$: is the generalized forces vector.

II.3 Transformations of reference frames and rotation vector

To simplify the study, it is necessary to define the reference frames that allow us to determine the energies and positions of the components of the rotor. Therefore, it is necessary to use multiple reference frames. The use of multiple reference frames involves investigating the relationships between different specified systems to perform transformations between reference frames in Figure II.2. There are three primary Cartesian coordinate systems.

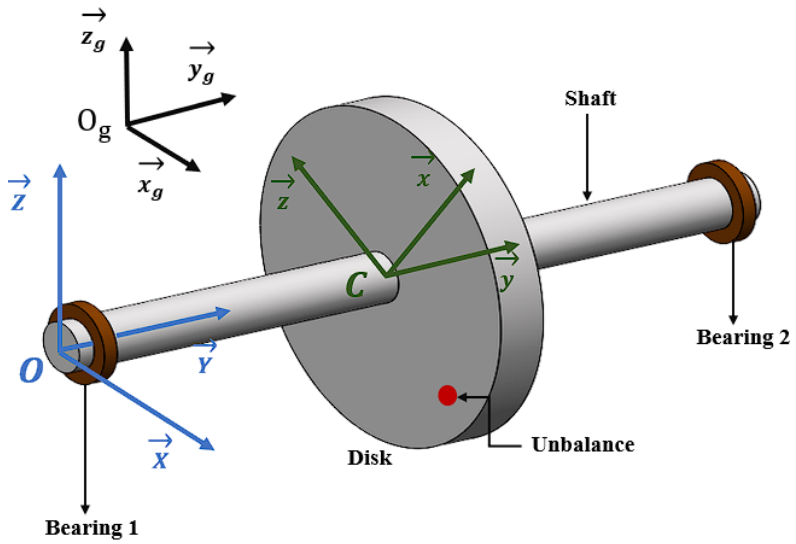

Figure II.2: The reference frames used in modeling the rotor

(x_g, y_g, z_g) represents the Galilean coordinate system associated with the Earth (fixed). (X, Y, Z) is the coordinate system associated with the direction of the bearing, and (x, y, z) refers to the local coordinate system associated with the center of mass of the rigid disk or the geometric center of the shaft at any time during its deformation.

The points (O_g), (O), and (C) represent the origins of the reference frames (R_g), (R_b), and (R_C), respectively. Since the Support is considered rigid, it has been entirely designed within its own frame. The rotational movements of the Support are determined by three angles that allow the transition from the Galilean reference frame (R_g) to the frame (R_b).

Considering that the rotating shaft experiences no deformation when at rest, and that OY in the reference frame associated with the holder (R_b) coincides with its central axis, meaning that OY is the longitudinal axis of the shaft where the center of mass of the disk is located, then the axes OX, OY, and OZ in the reference frame (R_b) are the principal axes of inertia that coincide with the moments of inertia of the disk and the shaft.

Given that the rotating shaft experiences no deformation when at rest and that OY in the reference frame associated with the holder (R_b) coincides with its central axis, which is the longitudinal axis of the shaft where the center of mass of the disk is located, the axes OY, OY, and OY in the reference frame (R_b) are the principal axes of inertia that coincide with the moments of inertia of the disk and the shaft.

The ideal rotor (with no unbalance) rotates around the OY axis without any deformation at a constant velocity Ω, according to the assumptions mentioned earlier. However, in the general case of a real rotor, it rotates around the Cy axis due to different angular deformations that the shaft experiences. As a result, its central axis no longer coincides with the OY axis; instead, it becomes curved.

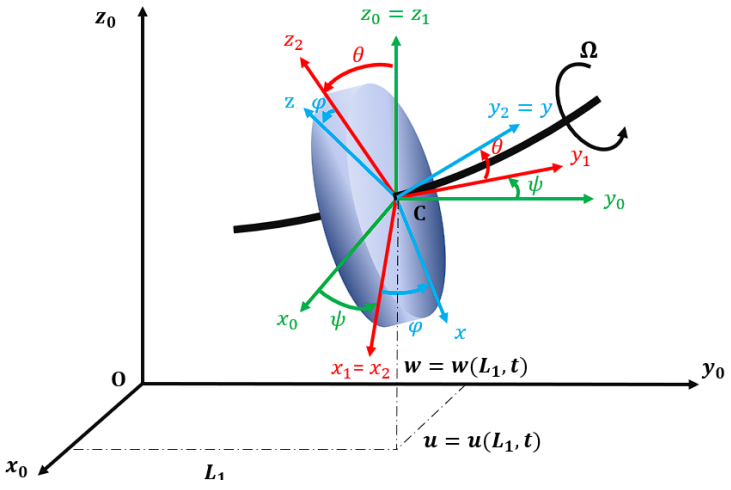

Figure II.3: Different marks related to the rigid disc and the flexible shaft.

The coordinate system $R_0(O, x_0, y_0, z_0)$ is related to the coordinate system $R(C, x, y, z)$ through three angles known as Euler angles ψ, θ, and φ. As represented in Figure II.3, these angles describe the motion of the disk. Figure II.4 illustrates a simple rotation about the axes to perform the transformation between references and establish transformation relationships through the following sequential rotations:

• 1^{st} rotation : the rotation of the angle ψ about the axis (C, z_0) «precession angle» which changes the reference $R_0(O, x_0, y_0, z_0)$ to $R_1(C, x_1, y_1, z_1)$.

• 2^{st} rotation : the rotation of the angle θ around the axis (C, x_1)«nutation angle» which changes the reference $R_1(C, x_1, y_1, z_1)$ to $R_2(C, x_2, y_2, z_2)$.

• 3^{st} rotation : the rotation of the angle φ about the axis (C, y_2)«proper rotation angle» which changes the reference $R_2(C, x_2, y_2, z_2)$ to $R(C, x, y, z)$.

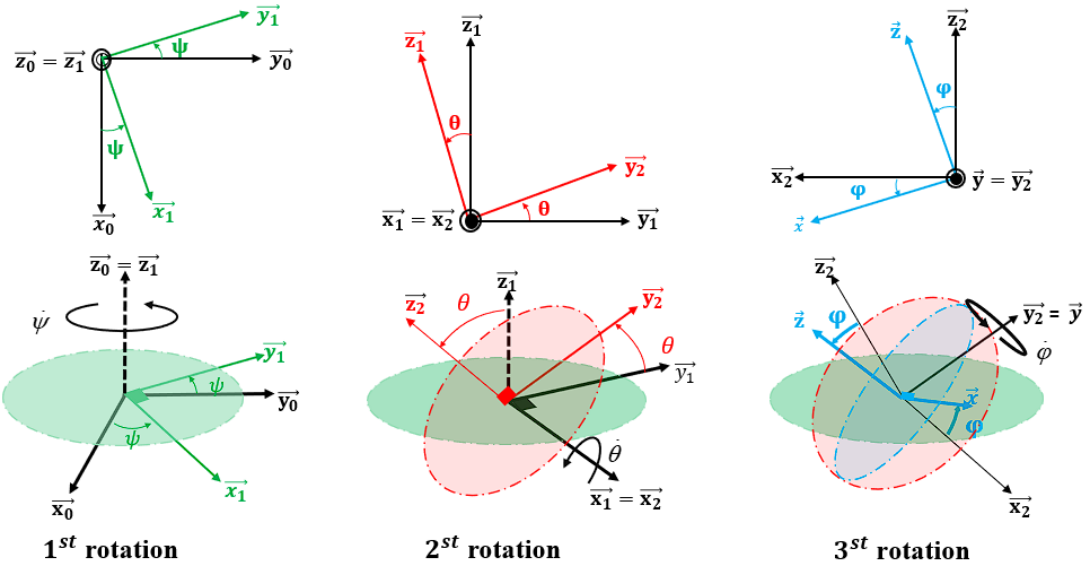

Figure II.4: Disc Rotation Details (Euler Angles).

Calculating the energies of various rotor components requires the preparation of angular velocity vectors for coordinate systems and position vectors for their origins. $\vec{\omega}(R/R_C)$ represents the angular velocity vector of the local frame (R_C) with respect to the frame fixed to the support (R) and expresses the position of (R_C) in (R). It can be written as follows:

$$\vec{\omega}(R/R_C) = \dot{\psi}\vec{z}_1 + \dot{\theta}\vec{x}_2 + \dot{\varphi}\vec{y} \tag{II.2}$$

$\vec{z}_1$,$\vec{x}_2$ and $\vec{y}$ are the unit vectors of the axes (C, z_1), (C, x_2) and (C, y).

The rotational velocity vector must be expressed in the coordinate system $R(C, x, y, z)$. To do this, the expressions for the unit vectors (z_1) and (x_2) must be determined as a function of the unit vectors in the coordinate system $R(C, x, y, z)$ using the representations given in Figure II.4.

1^{st} **rotation**:$(x_0, y_0 z_0) \xrightarrow{rot(\psi, z_0)} (x_1, y_1, z_1 = z_0)$

$$\begin{Bmatrix} \vec{x}_1 \\ \vec{y}_1 \\ \vec{z}_1 \end{Bmatrix} = \underbrace{\begin{bmatrix} \cos\psi & \sin\psi & 0 \\ -\sin\psi & \cos\psi & 0 \\ 0 & 0 & 1 \end{bmatrix}}_{[R_1]} \begin{Bmatrix} \vec{x}_0 \\ \vec{y}_0 \\ \vec{z}_0 \end{Bmatrix} \tag{II.3}$$

2^{st} **rotation**:$(x_1, y_1 z_1) \xrightarrow{rot(\theta, x_1)} (x_1 = x_2, y_2, z_2)$

$$\begin{Bmatrix} \vec{x}_2 \\ \vec{y}_2 \\ \vec{z}_2 \end{Bmatrix} = \underbrace{\begin{bmatrix} 1 & 0 & 0 \\ 0 & \cos\theta & \sin\theta \\ 0 & -\sin\theta & \cos\theta \end{bmatrix}}_{[R_2]} \begin{Bmatrix} \vec{x}_1 \\ \vec{y}_1 \\ \vec{z}_1 \end{Bmatrix} \tag{II.4}$$

3^{st} **rotation**:$(x_2, y_2 z_2) \xrightarrow{rot(\varphi, y)} (x, y_2 = y, z)$

$$\begin{Bmatrix} \vec{x} \\ \vec{y} \\ \vec{z} \end{Bmatrix} = \underbrace{\begin{bmatrix} \cos\varphi & 0 & -\sin\varphi \\ 0 & 1 & 0 \\ \sin\varphi & 0 & \cos\varphi \end{bmatrix}}_{[R]} \begin{Bmatrix} \vec{x}_2 \\ \vec{y}_2 \\ \vec{z}_2 \end{Bmatrix} \tag{II.5}$$

Cam here cam the rotation velocity victor **equation**. **II.2**

$$\begin{Bmatrix} \vec{x} \\ \vec{y} \\ \vec{z} \end{Bmatrix} = [R_3] \begin{Bmatrix} \vec{x}_2 \\ \vec{y}_2 \\ \vec{z}_2 \end{Bmatrix} \Rightarrow \begin{Bmatrix} \vec{x}_2 \\ \vec{y}_2 \\ \vec{z}_2 \end{Bmatrix} = [R_3]^T \begin{Bmatrix} \vec{x} \\ \vec{y} \\ \vec{z} \end{Bmatrix} = \begin{bmatrix} \cos\varphi & 0 & \sin\varphi \\ 0 & 1 & 0 \\ -\sin\varphi & 0 & \cos\varphi \end{bmatrix} \begin{Bmatrix} \vec{x} \\ \vec{y} \\ \vec{z} \end{Bmatrix} \tag{II.6}$$

From the **equation II.6** we get:

$$\vec{x}_2 = \cos\varphi \vec{x} + \sin\varphi \vec{z} \tag{II.7}$$

.

$$\begin{Bmatrix} \vec{x} \\ \vec{y} \\ \vec{z} \end{Bmatrix} = [R_3]\,[R_2] \begin{Bmatrix} \vec{x}_1 \\ \vec{y}_1 \\ \vec{z}_1 \end{Bmatrix} \Rightarrow \begin{Bmatrix} \vec{x}_1 \\ \vec{y}_1 \\ \vec{z}_1 \end{Bmatrix} = [R_2]^T [R_3]^T \begin{Bmatrix} \vec{x} \\ \vec{y} \\ \vec{z} \end{Bmatrix}$$
$$= \begin{bmatrix} 1 & 0 & 0 \\ 0 & \cos\theta & -\sin\theta \\ 0 & \sin\theta & \cos\theta \end{bmatrix} \begin{bmatrix} \cos\varphi & 0 & \sin\varphi \\ 0 & 1 & 0 \\ -\sin\varphi & 0 & \cos\varphi \end{bmatrix} \begin{Bmatrix} \vec{x} \\ \vec{y} \\ \vec{z} \end{Bmatrix} \tag{II.8}$$
$$= \begin{bmatrix} \cos\varphi & 0 & \sin\varphi \\ -\sin\theta\sin\varphi & \cos\theta & -\sin\theta\cos\varphi \\ -\cos\theta\sin\varphi & \sin\theta & \cos\theta\cos\varphi \end{bmatrix} \begin{Bmatrix} \vec{x} \\ \vec{y} \\ \vec{z} \end{Bmatrix}$$

From the **equation II.8** we get:

$$\vec{z}_1 = -\cos\theta\sin\varphi \vec{x} + \sin\theta \vec{y} + \cos\theta\cos\varphi \vec{z} \tag{II.9}$$

When replacing the **equations II.7** and **II.9** into **equation II.2**, the expression of rotational velocity victor in the coordinates (x, y, z) becomes written as follows:

$$\vec{\omega}(R/R_C) = \left(\dot{\varphi}\cos\theta - \dot{\psi}\cos\theta\sin\varphi\right)\vec{x} + (\dot{\varphi} + \sin\theta)\,\vec{y} + (\dot{\theta}\sin\varphi + \dot{\psi}\cos\theta\cos\varphi)\vec{z} \tag{II.10}$$

Based on that, we obtain:

$$\vec{\omega}(R/R_C) = \begin{Bmatrix} \omega_x \\ \omega_y \\ \omega_z \end{Bmatrix} = \begin{pmatrix} \dot{\theta}\cos\varphi - \dot{\psi}\cos\theta\sin\varphi \\ \dot{\varphi} + \dot{\psi}\sin\theta \\ \dot{\theta}\sin\varphi + \dot{\psi}\cos\theta\cos\varphi \end{pmatrix} \tag{II.11}$$

Given that the disk rotates as a constant velocity Ω around its main axis and therefor $\dot{\varphi} = \Omega$, in addition to that, the curvature of the shaft is low and is angles ψ and θ are small, so approximate estimates can be made $\cos\theta \approx 1$ and $\sin\theta \approx \theta$. The rotational velocity victor becomes:

$$\vec{\omega}(R/R_C) = \begin{Bmatrix} \omega_x \\ \omega_y \\ \omega_z \end{Bmatrix} = \begin{pmatrix} \dot{\theta}\cos\varphi - \dot{\psi}\sin\varphi \\ \Omega + \dot{\psi}\theta \\ \dot{\theta}\sin\varphi + \dot{\psi}\cos\varphi \end{pmatrix} \tag{II.12}$$

II.4 Equations of Motion: Algebraic Formulation

In this section, an analytical model for the dynamic behavior of the rotating member was developed. First, kinetic energy expressions were established for the disc, as well as kinetic and potential energy expressions for the shaft, and kinetic energy for the imbalance. Additionally, the virtual work for the load was formulated. Then, the equations of motion were derived by applying Lagrange's equations.

II.4.1 Calculating the energy of the rigid disk

It is assumed that the disk is rigidly attached to the coordinate system x, y, z at its center of mass C in order to formulate the equations of motion and calculate the kinetic energy of the disk. This kinetic energy T_D includes components associated with rotation and the displacement of its center of mass C. The position of C in the coordinate system (x_0, y_0, z_0) (see Figure II.3) is determined by:

$$\overrightarrow{OC} = \begin{bmatrix} u(y,t) \\ L_1 \\ w(y,t) \end{bmatrix} \tag{II.13}$$

$u(y,t)$ and $w(y,t)$ are displacement functions that depend solely on time t, as the studied motions are only related to the lateral deflection of the rotor.

The velocity of the disk's displacement is expressed as follows

$$\vec{V}\left(C/R_0\right) = \left[\frac{d\overrightarrow{OC}}{dt}\right]_{R_0} = \frac{d}{dt}\left(u\vec{x}_0 + L_1\vec{y}_0 + w\vec{z}_0\right) = \dot{u}\vec{x}_0 + \dot{w}\vec{z}_0 \tag{II.14}$$

By knowing the mass of the disk M_d, we can formulate the expression for the kinetic energy T_D^{tra} related to its translation motion as follows:

$$T_D^{tra} = 1/2 M_D\left(\vec{V}\left(C/R_0\right)\right)^2 = 1/2 M_D(\dot{u}^2 + \dot{w}^2) \tag{II.15}$$

The kinetic energy of rotation T_D^{rot} is obtained from the angular velocity of the disk, $\omega(R/R_C)$, and the moment of inertia expressed in the local coordinate system R_C, respectively, given by:

$$I_D = \begin{bmatrix} I_{Dx} & 0 & 0 \\ 0 & I_{Dy} & 0 \\ 0 & 0 & I_{Dz} \end{bmatrix}; \overrightarrow{\omega} = \begin{Bmatrix} \omega_x \\ \omega_y \\ \omega_z \end{Bmatrix} \tag{II.16}$$

I_{D_x}, I_{D_y}, and I_{D_z} are the moments of inertia along the x, y, and z axes, and the kinetic energy in rotation T_D^{rot} is thus calculated by the following expression:

$$T_D^{rot} = 1/2 I_D\omega^2 = 1/2\left(I_{D_x}\omega_x^2 + I_{D_y}\omega_y^2 + I_{D_z}\omega_z^2\right) \tag{II.17}$$

The total kinetic energy is obtained by combining translation and rotational kinetic energy as follows:

$$T_D = T_D^{tra} + T_D^{rot} \tag{II.18}$$

Substituting **equations II.15** and **II.17** into **equation II.18**, this allows us to write the expression for the total kinetic energy of the disk as follows:

$$T_D = {}^1\!/_2 M_D(\dot{u}^2 + \dot{w}^2) + {}^1\!/_2 \left(I_{D_x}\omega_x^2 + I_{D_y}\omega_y^2 + I_{D_z}\omega_z^2\right) \tag{II.19}$$

Substituting **equationII.12** into **equation II.19**, we get:

$$\begin{aligned} T_D &= {}^1\!/_2 M_D(\dot{u}^2 + \dot{w}^2) \\ &+ {}^1\!/_2 I_{D_x} \left(\underbrace{\dot{\theta}^2\cos^2\varphi + \dot{\psi}^2\sin^2\varphi - 2\dot{\theta}\dot{\psi}\cos\varphi\sin\varphi}_{\omega_x^2} \right) \\ &+ {}^1\!/_2 I_{D_y} \left(\underbrace{\Omega^2 + \dot{\psi}^2\dot{\theta}^2 + 2\Omega\dot{\psi}\theta}_{\omega_y^2} \right) \\ &+ {}^1\!/_2 I_{D_z} \left(\underbrace{\dot{\theta}^2\sin^2\varphi + \dot{\psi}^2\cos^2\varphi + 2\dot{\psi}\dot{\theta}\sin\varphi\cos\varphi}_{\omega_z^2} \right) \end{aligned} \tag{II.20}$$

The **equation II.20** can be simplified since the disk is symmetrical, which means that the moments of inertia about the x and y axes are equal, i.e., $I_{D_x} = I_{D_y}$. Additionally, we can neglect the term $\dot{\psi}^2\dot{\theta}^2$, which is of higher order, and this makes in Eq II.20 as follows:

$$T_D = \underbrace{\frac{1}{2}M_D(\dot{u}^2 + \dot{w}^2)}_{\text{Translation}} + \underbrace{\frac{1}{2}I_{D_x}\left(\dot{\theta}^2 + \dot{\psi}^2\right)}_{\text{Rotation}} + \underbrace{I_{D_y}\Omega\dot{\psi}\theta}_{\textbf{Gyroscopic Effect}} + \frac{1}{2}I_{D_y}\Omega^2 \tag{II.21}$$

Whereas the term $I_{D_y}\Omega\dot{\psi}\theta$ represents the gyroscopic effect, the latter term $\frac{1}{2}I_{D_y}\Omega^2$ which is a constant that does not affect the equations and represents the rotational energy of the disk.

II.4.2 Calculating the energy of the Shaft

The flexible shaft is depicted in the form of a cross-sectional girder and is characterized by kinetic energy and deformation energy.

II.4.2.1 Kinetic energy

The general formula for the kinetic energy of the shaft dT_s can be deduced by extending the kinetic energy of the disc through integration along the length of the shaft (see Figure II.5).

The kinetic energy of the shaft dT_a is calculated by selecting an element of the shaft and considering it as a thin disk with thickness dy, and a presumed constant circular cross-section. ρ represents the volumetric mass density, while I_x and I_y represents the diagonal moment of inertia.

The elementary mass dM_a and principal moments of inertia I_x and I_y are calculated in the local coordinate system using the following method:

$$dM_s = \rho s dy \tag{II.22}$$

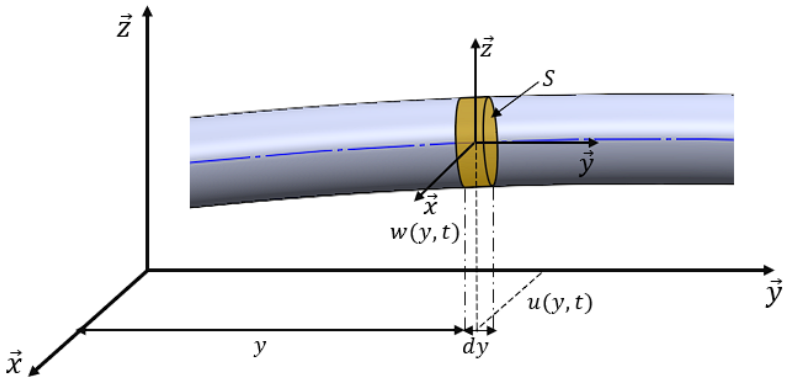

Figure II.5: Bending shaft element

$$\begin{cases} dI_{s_x} = \iiint\limits_{(V)} (y^2+z^2)\,dm = \left(\iint\limits_{(S)} z^2 dS\right)\rho dy = \rho I_x dy \\ dI_{s_y} = \iiint\limits_{(V)} (x^2+z^2)\,dm = \left(\iint\limits_{(S)} x^2 dS + \iint\limits_{(S)} z^2 dS\right)\rho dy = \rho(I_x+I_z)dy \\ dI_{s_z} = \iiint\limits_{(V)} (y^2+x^2)\,dm = \left(\iint\limits_{(S)} x^2 dS\right)\rho dy = \rho I_z dy \end{cases} \tag{II.23}$$

The initial kinetic energy of an extremely thin section of the rotating shaft is written as follows:

$$dT_s = \left(\tfrac{1}{2}\rho s(\dot{u}^2+\dot{w}^2) + \tfrac{1}{2}\left(\rho I_x\omega_x^2 + \rho\left(I_x+I_z\right)\omega_y^2 + \rho I_z\omega_z^2\right)\right)dy \tag{II.24}$$

Since the rotating shaft is symmetrical, $I_x = I_y = I$, the expression becomes as follows:

$$dT_s = \left(\tfrac{1}{2}\rho s(\dot{u}^2+\dot{w}^2) + \rho I/2\left(\omega_x^2 + 2\omega_y^2 + \omega_z^2\right)\right)dy \tag{II.25}$$

Then, to obtain the expression for the kinetic energy of the shaft with a length of L, we integrate along the length of the shaft as follows:

$$\begin{aligned} T_s &= \rho s/2 \int_0^L (\dot{u}^2+\dot{w}^2)dy + \rho I/2 \int_0^L \left(\omega_x^2 + 2\omega_y^2 + \omega_z^2\right)dy \\ &= \underbrace{\rho s/2 \int_0^L \left(\dot{u}^2+\dot{w}^2\right)dy}_{\text{Translation}} + \underbrace{\rho I/2 \int_0^L \left(\dot{\psi}^2+\dot{\theta}^2\right)dy}_{\text{Rotation}} + \underbrace{2\rho I\Omega \int_0^L \dot{\psi}\theta dy}_{\textbf{Gyroscopic effect}} + \rho I L\Omega^2 \end{aligned} \tag{II.26}$$

The first integral represents the classical expression for the kinetic energy of the beam in bending, while the second integral represents the secondary effect of rotational inertia. The third integral accounts for the gyroscopic effect, and term is the constant $\rho I L\Omega^2$.

II.4.2.2 Strain Energy

The deformation energy of the rotating shaft is calculated by considering it in its ideal state as a flexible beam in rotation without deformation due to lateral forces (only deformations due to bending are taken into account), and the effects of shear are neglected. It is also important to consider the geometric configuration illustrated in Figure 6, where C is the geometric center of the shaft, and point $B(x', z')$ is a typical point on the circular cross-section. u^* and w^* represent the displacements of the geometric center C with respect to the x^* and z^* axes, respectively.

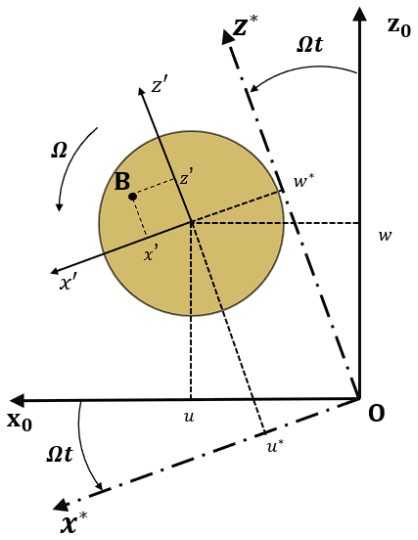

Figure II.6: Coordinates of the geometric center C and an arbitrary point B of the section of the rotor

According to the beam theory the deflections u*(y) and w*(y) are determined as follows:

- In the plan x^*Oy^*:

$$EI\frac{\partial^2 u^*}{\partial y^2} = -M_z\left(y\right) \tag{II.27}$$

- In the plan y^*Oz^*

$$EI\frac{\partial^2 w^*}{\partial y^2} = -M_x\left(y\right) \tag{II.28}$$

E: Young's modulus.
I: Quadratic moment of inertia of the section.
$M_z\left(y\right)$: Bending moment in plane x^*Oy^*.
$M_x\left(y\right)$: Bending moment in plane y^*Oz^*.

The stresses at point $B(x', z')$ are:

- In the plan x^*Oy^*:

$$\sigma_{yy}^{x'} = \frac{M_z\left(y\right)}{I}x' = E\varepsilon_{yy}^{x'} \tag{II.29}$$

- In the plan y^*Oz^*

$$\sigma_{yy}^{z'} = \frac{M_x\left(y\right)}{I}z' = E\varepsilon_{yy}^{z'} \tag{II.30}$$

By combining the equations II.27 and II.29 we get:

$$\varepsilon_{yy}^{x'} = -x' \frac{\partial^2 u^*}{\partial y^2} \tag{II.31}$$

Same thing with equations II.28 and II.30 we get:

$$\varepsilon_{yy}^{z'} = -z' \frac{\partial^2 w^*}{\partial y^2} \tag{II.32}$$

By adding Equation II.31 and II.32, we obtain the longitudinal deformation at point $M(x', z')$ as follows:

$$\varepsilon_{yy} = -x' \frac{\partial^2 u^*}{\partial y^2} - z' \frac{\partial^2 w^*}{\partial y^2} \tag{II.33}$$

The strain energy U_s is given by:

$$U_s = 1/2 \int_{(V)} \varepsilon_{yy} \sigma_{yy} dV \tag{II.34}$$

U: is the strain energy.
V: is the volume of the shaft.
σ: is the stress.
ε: is the strain

When referring to Hooke's law $\sigma = E\varepsilon$, we find the relationship between stresses and deformations, and from it the term strain energy becomes as follows :

$$U_s = 1/2 \int_{(V)} \varepsilon_{yy}^2 dV \tag{II.35}$$

Substituting equation II.33 into equation II.34, we get:

$$\begin{aligned} U_s &= 1/2 E \int_{(V)} \left(-x' \tfrac{\partial^2 u^*}{\partial y^2} - z' \tfrac{\partial^2 w^*}{\partial y^2} \right)^2 dV \\ &= 1/2 E \int_0^L \int_S \left[x'^2 \left(\tfrac{\partial^2 u^*}{\partial y^2} \right)^2 + z'^2 \left(\tfrac{\partial^2 w^*}{\partial y^2} \right)^2 + 2x'z' \tfrac{\partial^2 u^*}{\partial y^2} \tfrac{\partial^2 w^*}{\partial y^2} \right] ds dy \\ &= 1/2 E \int_0^L \left[\int_S x'^2 \left(\tfrac{\partial^2 u^*}{\partial y^2} \right)^2 ds + \int_S z'^2 \left(\tfrac{\partial^2 w^*}{\partial y^2} \right)^2 ds + 2 \int_S x'z' \tfrac{\partial^2 u^*}{\partial y^2} \tfrac{\partial^2 w^*}{\partial y^2} ds \right] dy \end{aligned} \tag{II.36}$$

Given the symmetry of the cross-section of the shaft, $\int_S x'z'ds = 0$, and by introducing the diagonal inertia of the cross-section we have:

$$\begin{cases} I_{x'} = \int_s z'^2 ds = I_a \\ I_{z'} = \int_s x'^2 ds = I_a \end{cases} \tag{II.37}$$

the stain energy of the shaft therefore has the expression :

$$U_s = EI_a/2 \int_0^L \left[\left(\frac{\partial^2 u^*}{\partial y^2} \right)^2 + \left(\frac{\partial^2 w^*}{\partial y^2} \right)^2 \right] dy \tag{II.38}$$

We will use the expressions u^* and w^* in terms of u and w to express the deformation energy U_a in the fixed frame (see figure II.6)

$$\begin{cases} u^* = u\cos\Omega t - w\sin\Omega t \\ w^* = u\sin\Omega t + w\cos\Omega t \end{cases} \tag{II.39}$$

By substituting equation II.39 in equation II.38, the expression becomes as follows:

$$U_s = {}^{EI_a}\!/_2 \int_0^L \left[\left(\cos\Omega t \frac{\partial^2 u}{\partial y^2} - \sin\Omega t \frac{\partial^2 w}{\partial y^2} \right)^2 + \left(\sin\Omega t \frac{\partial^2 u}{\partial y^2} + \cos\Omega t \frac{\partial^2 w}{\partial y^2} \right)^2 \right] dy \tag{II.40}$$

After simplifying equation II.40, we get the final expression for the strain energy of the rotating shaft as follows:

$$U_s = {}^{EI_a}\!/_2 \int_0^L \left[\left(\frac{\partial^2 u}{\partial y^2} \right)^2 + \left(\frac{\partial^2 w}{\partial y^2} \right)^2 \right] dy \tag{II.41}$$

Note: If the rotating shaft is subjected to a constant axial force F_0, the expression for the deformation energy of the shaft becomes as follows [98]:

$$U_s = {}^{EI_a}\!/_2 \int_0^L \left[\left(\frac{\partial^2 u}{\partial y^2} \right)^2 + \left(\frac{\partial^2 w}{\partial y^2} \right)^2 \right] dy + {}^{F_0}\!/_2 \int_0^L \left[\left(\frac{\partial^2 u}{\partial y^2} \right)^2 + \left(\frac{\partial^2 w}{\partial y^2} \right)^2 \right] dy \tag{II.42}$$

II.4.2.3 Calculating The Energy Of The Unbalance

Unbalance is a mass located at a distance from the axis of rotation of a rotor, causing the appearance of centrifugal self-balancing forces. Almost any part with imbalance has some degree of importance. In practice, Unbalance occurs along the axis of rotation of the shaft, as shown in Figure II.7.

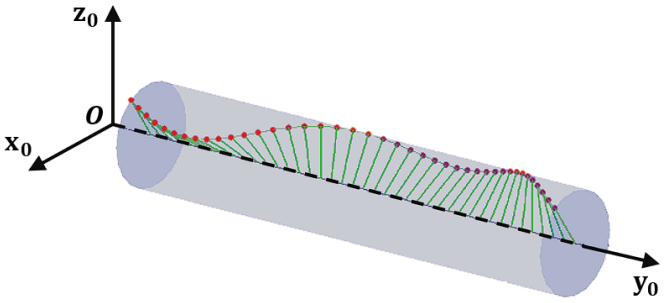

Figure II.7: Random unbalance distribution

To model such a case, we use the method of the centroidal mass, as depicted in Figure II.8.

In our case, the unbalance, denoted as m_b, is placed at point B on the disk section at a distance of d from the axis. It possesses kinetic energy T_u. The geometric center of the imbalance is assumed to be C. Unbalance is represented in Figure II.9.

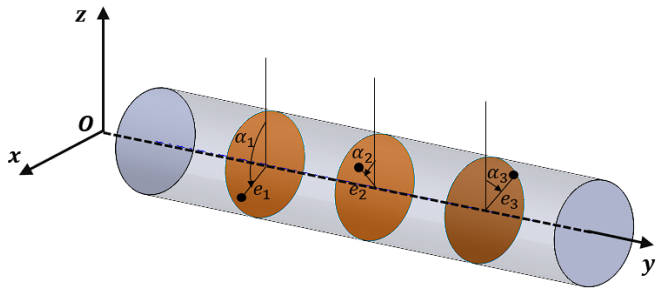

Figure II.8: Plane modeling of unbalances

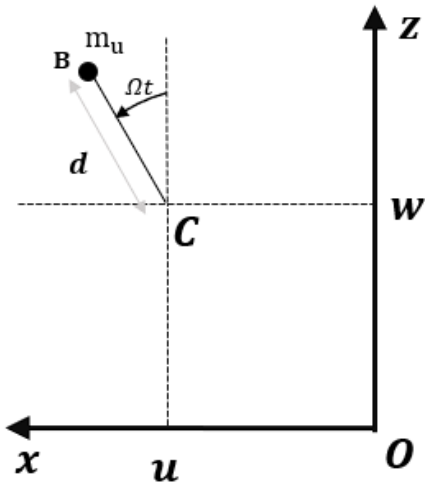

Figure II.9: representation of Unbalance

$$\begin{aligned}\overrightarrow{OB} &= \overrightarrow{OC} + \overrightarrow{CB} \\ &= \left\{\begin{array}{c} u \\ \mathrm{v} \\ w \end{array}\right\} + d\left\{\begin{array}{c} \cos\Omega t \\ \text{constant} \\ \sin\Omega t \end{array}\right\} \\ &= \left\{\begin{array}{c} u + d\cos\Omega t \\ \text{constant} \\ v + d\sin\Omega t \end{array}\right\}\end{aligned} \tag{II.43}$$

The unbalance kinetic energy has the expression:

$$T_u = {}^1\!/_2 m_u \left(\overrightarrow{V}(B)\right)^2 \tag{II.44}$$

where $V(B)$ is the velocity velocity of the unbalance and is written in the following form:

$$\overrightarrow{V}(B) = \frac{d\overrightarrow{OB}}{dt} = \left\{\begin{array}{c} \dot{u} + d\Omega\cos\Omega t \\ 0 \\ \dot{w} - d\Omega\sin\Omega t \end{array}\right\} \tag{II.45}$$

So the kinetic energy has the expression:

$$\begin{aligned}T_u &= {}^1\!/_2 m_u \left((\dot{u} + d\Omega\cos\Omega t)^2 + (\dot{w} - d\Omega\sin\Omega t)^2\right) \\ &= {}^1\!/_2 m_u \left(\dot{u}^2 + \dot{w}^2 + d^2\Omega^2 + 2\dot{u}d\Omega\cos\Omega t - 2\dot{w}d\Omega\sin\Omega t\right)\end{aligned} \tag{II.46}$$

The term $d^2\Omega^2$ is a constant that has no effect on the equations of motion (zero derivative Lagrangian equations). Since the mass of the unbalance m_u is small compared to the mass of the rotor (the mass of the shaft and the disk), the kinetic energy expression can be approximated as follows:

$$T_u \approx m_u \Omega d \left(\dot{u} \cos \Omega t - \dot{w} \sin \Omega t\right) \tag{II.47}$$

II.4.2.4 Virtual work of bearing forces

In general, the bearings are considered non-rigid (hydrodynamic bearings). The forces resulting from these bearings result from the displacement of the column, and these forces are of the nature of stiffness and damping. The bearing is represented by the Kelvin model in every direction perpendicular to the shaft axis, which includes the characteristics of stiffness and damping. Figure II.10.

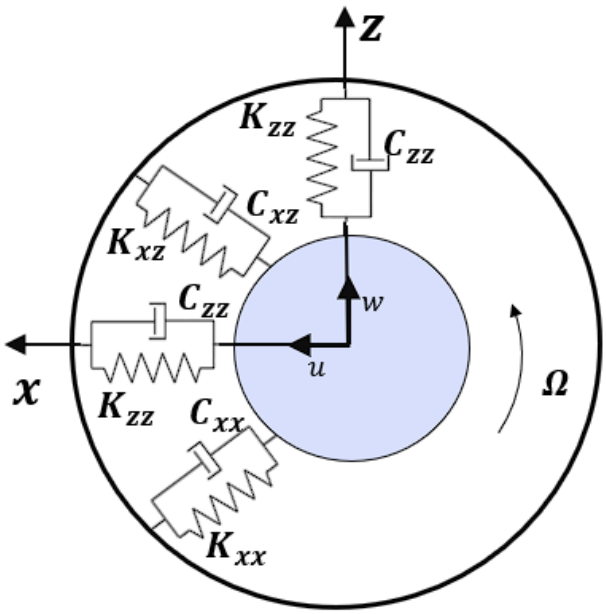

Figure II.10: Damping and bearing stiffnesses

The characteristics associated with these efforts are:

- $K_x x$, $K_z z$, $C_x x$, $C_z z$ Stiffness and damping according to the x and z directions of the shaft.
- $K_x z$, $K_z x$, $C_x z$, $C_z x$ are stiffnesses and dampings in one direction (x or z) but affected by the other direction. They represent coupling constants.

the virtual work of these forces:

$$\delta W = -K_{xx} u \delta u - K_{xz} w \delta u - K_{zz} w \delta w - K_{zx} u \delta w - c_{xx} \dot{u} \delta u - c_{xz} \dot{w} \delta u - c_{zz} \dot{w} \delta w - c_{zx} \dot{u} \delta w \tag{II.48}$$

or

$$\delta W = F_u \delta u + F_w \delta w \tag{II.49}$$

F_u and F_w The components of generalized forces
By using the two equations II.48 and II.49 it we get :

$$\left\{ \begin{array}{c} F_u \\ F_w \end{array} \right\} = - \left[\begin{array}{cc} K_{xx} & K_{xz} \\ K_{zx} & K_{zz} \end{array} \right] \left\{ \begin{array}{c} u \\ w \end{array} \right\} - \left[\begin{array}{cc} c_{xx} & c_{xz} \\ c_{zx} & c_{zz} \end{array} \right] \left\{ \begin{array}{c} \dot{u} \\ \dot{w} \end{array} \right\} \tag{II.50}$$

II.5 Analytical model: Simple model

To study and analyse the special phenomena that can occur in rotor dynamics, we developed a simple rotor model. Modelling is performed using the Rayleigh-Ritz method. The model considered consists of a symmetric shaft of length L and a symmetric disc located at y=l1 with unbalance and rotor support at both ends, and finally, the bearings are infinitely rigid (see Figure. II.11).

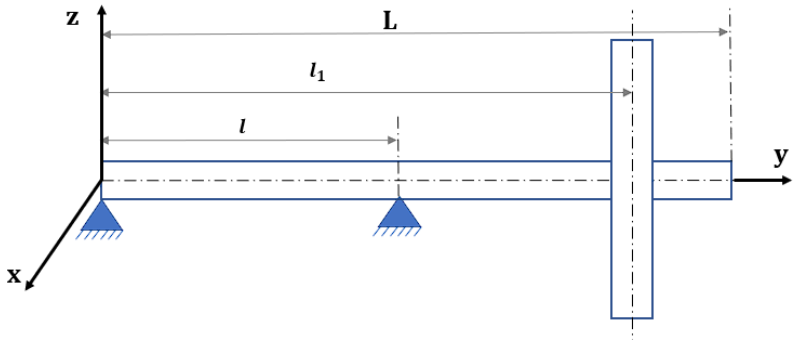

Figure II.11: Simple rotor model

II.5.1 Application of the Rayleigh-Ritz Method

The Rayleigh-Ritz method is based on the approximation of a continuous system by assuming that it can be represented as a system of one degree equivalent by assuming the existence of a single distortion form. The transformation of the continuous system into a multi-degree-of-freedom system is converted, the number of DOf is equivalent to the number of selected Ritz modes, this method is applied in this part as follows. The displacements in the direction of x and y can be expressed as follows [99]: ¨

$$\begin{cases} u(y,t) = f(y)\, q_1(t) = f(y)\, q_1 \\ u(y,t) = f(y)\, q_2(t) = f(y)\, q_2 \end{cases} \tag{II.51}$$

where $f(y)$ is the shape of the chosen mode and is equal to the dynamic deformation of the beam in the case of the supported rotor, and q_1 and q_2 are the independent generalised coordinates.

- The first mode $f(y) = \sin({}^{\pi y}/_{L})$
- The second mode $f(y) = \sin\left({}^{2\pi y}/_{L}\right)$

based on the assumption that the angles θ and ψ are small (see the figure II.12), they can be estimated as follows :

$$\begin{cases} \theta = \frac{\partial w}{\partial y} = \frac{df(y)}{dy} q_2 = g(y)\, q_2 \\ \psi = -\frac{\partial u}{\partial y} = -\frac{df(y)}{dy} q_1 = -g(y)\, q_1 \end{cases} \tag{II.52}$$

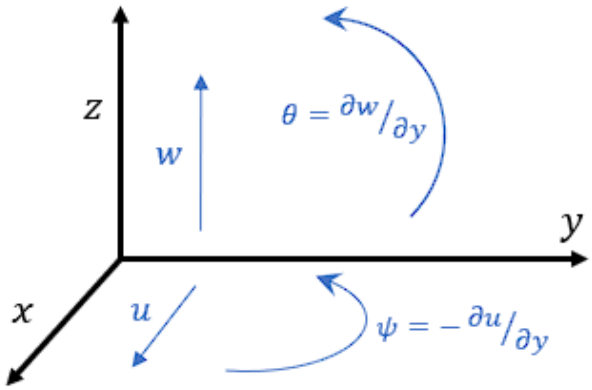

Figure II.12: Representation of displacements and angles

The second derivative of taking into account that the generalised coordinates q_1 and q_2 are independent of y gives:

$$\begin{cases} \frac{\partial^2 u}{\partial y^2} = \frac{d^2 f(y)}{dy^2} q_1 = h\left(y\right) q_1 \\ \frac{\partial^2 u}{\partial y^2} = \frac{d^2 f(y)}{dy^2} q_2 = h\left(y\right) q_2 \end{cases} \tag{II.53}$$

II.5.2 The Final Rotor Motion Equation

We replace the variables u, w, θ, and ψ with their functions defined in the kinetic energy of column, disk and unbalance expressions and produce the following expressions:

II.5.2.1 Rotor kinetic energy

- For a disk placed at position $y = l_1$, the kinetic energy T_D is written:

$$T_D = {}^1\!/_2 \left[M_D f^2\left(l_1\right) + I_{D_x} g^2\left(l_1\right)\right]\left(\dot{q}_1^2 + \dot{q}_2^2\right) - I_{D_y} \Omega g^2\left(l_1\right) \dot{q}_1 q_2 \tag{II.54}$$

- For the shaft, the kinetic energy T_s is written:

$$T_s = {}^1\!/_2 \left[\rho S \int_0^L f^2\left(y\right) dy + \rho I \int_0^L g^2\left(y\right) dy\right]\left(\dot{q}_1^2 + \dot{q}_2^2\right) - 2\rho I \Omega \int_0^L g^2\left(y\right) dy \dot{q}_1 q_2 \tag{II.55}$$

- For the unbalance, the kinetic energy T_u is written:

$$T_u = m_u d \Omega f\left(l_1\right)\left(\dot{q}_1 \cos \Omega t - \dot{q}_2 \sin \Omega t\right) \tag{II.56}$$

- The total kinetic energy T of the rotor is written:

$$\begin{aligned} T &= T_D + T_s + T_u \\ &= \underbrace{\left[M_D f^2\left(l_1\right) + I_{D_x} g^2\left(l_1\right) + \rho S \int_0^L f^2\left(y\right) dy + \rho I \int_0^L g^2\left(y\right) dy\right]}_{m}\left(\dot{q}_1^2 + \dot{q}_2^2\right) \\ &\quad - \underbrace{\left[I_{D_y} g^2\left(l_1\right) + 2\rho I \int_0^L g^2\left(y\right) dy\right]}_{a} \Omega \dot{q}_1 q_2 + m_u d \Omega f\left(l_1\right)\left(\dot{q}_1 \cos \Omega t - \dot{q}_2 \sin \Omega t\right) \end{aligned} \tag{II.57}$$

$$T = m\left(\dot{q}_1^2 + \dot{q}_2^2\right) - a \Omega \dot{q}_1 q_2 + m_u d \Omega f\left(l_1\right)\left(\dot{q}_1 \cos \Omega t - \dot{q}_2 \sin \Omega t\right) \tag{II.58}$$

II.5.2.2 Strain energy

The strain energy of the shaft U_s , is written

$$U_s = {}^{EI}/_{2} \int_0^L h^2(y)dy \left(q_1^2 + q_2^2\right) \tag{II.59}$$

II.5.2.3 Equations of motion

The application of Lagrange's equations.

$$\frac{d}{dt}\left(\frac{\partial T}{\partial \dot{q}_i}\right) - \frac{\partial T}{\partial \dot{q}_i} + \frac{\partial U}{\partial q_i} = \delta W_i \tag{II.60}$$

With $i = 1, 2$

Applying Lagrange's equations to obtain a system of rotor equations and solving this system makes it possible to obtain the deflections of the rotating shaft line at each of its points and also allows us to calculate the components of the rotor's acceleration. The initial conditions are chosen arbitrarily or as a result of a previous calculation given that the external solicitation is periodic in nature.

II.5.3 Generalization of equations to an industrial rotary model

An industrial rotor is a rotor that has several sections with different diameter in the shaft, which is the same case being studied, in addition, it can also have several disks (see figure II.13). From the Lagrange equations applied to the prototype in paragraphs II.4.1 and II.4.2, the equation can be easily generalized to the case of an industrial rotor.

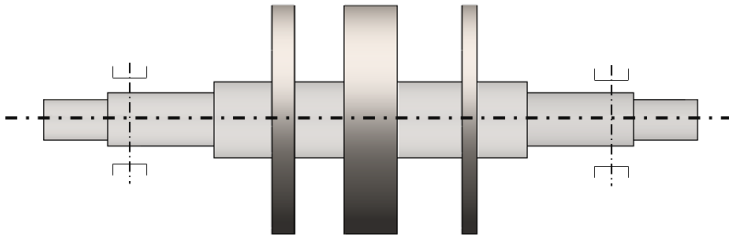

Figure II.13: Industrial rotor model

In the **equations** in paragraphs **II.4.1** and **II.4.2**, we replace the simple terms by the sum.

equation II.21 for the kinetic energy of a disk becomes when there are several disks, the equation of kinetic energy becomes as follows:

$$T_D = \sum_{i=1}^{n_D} \left(\frac{1}{2} M_{D_i}\left(\dot{u}_i^2 + \dot{w}_i^2\right) + \frac{1}{2} I_{D_{xi}}\left(\dot{\theta}_i^2 + \dot{\psi}_i^2\right) + I_{D_{yi}}\Omega\dot{\psi}_i\theta_i\right) \tag{II.61}$$

n_D: number of disks

equation II.26 for the kinetic energy of a shaft becomes when there are several sections with different diameters, the equation of kinetic energy of a shaft becomes as follows:

$$T_s = \sum_{j=1}^{n_s} \left(\rho S_i/2 \int_{L_{1j}}^{L_{2j}} \left(\dot{u}_i^2 + \dot{w}_i^2\right) dy + \rho I_i/2 \int_{L_{1j}}^{L_{2j}} \left(\dot{\theta}_i^2 + \dot{\psi}_i^2\right) dy + 2\rho I_i \Omega \int_{L_{1j}}^{L_{2j}} \dot{\psi}_i \theta_i dy \right) \quad \text{(II.62)}$$

n_s: number of sections.

As for the equations energy of a column containing several sections

$$U_s = \sum_{j=1}^{n_s} \left(EI_{s_i}/2 \int_{L_{1j}}^{L_{1j}} \left[\left(\frac{\partial^2 u}{\partial y^2} \right)^2 + \left(\frac{\partial^2 w}{\partial y^2} \right)^2 \right] \right) dy \quad \text{(II.63)}$$

II.6 Modeling of rotors by finite elements

The finite element method is widely used in the field of engineering sciences because it is considered one of the most important methods for modeling and solving complex problems, especially in rotor dynamics. In this part of the chapter, the finite element method has been applied to rotating elements, which makes it possible to develop general equations of motion and obtain a model that can deal with rotating industrial machines. This method provides a better understanding of the behavior of the rotor. The application of the method allows gyroscopic effects to be taken into account, and finite solution methods can be usefully used.

II.6.1 Finite elements for rotor components

It is necessary to identify the main elements that make it possible to model rotors effectively. These elements include discs, shafts, bearings, and the representation of external forces, especially those resulting from misalignments. These elements play a role in understanding and analysing the behaviour of rotors.

II.6.1.1 Disk

The disk has been modelled using finite element methods in the case of a disk when it is symmetric and rigid (inelastic). It is represented using a single node containing four degrees of freedom, including two glides u and W and two pairs of cycles and about the x and Y axes, respectively (see Figure 12).

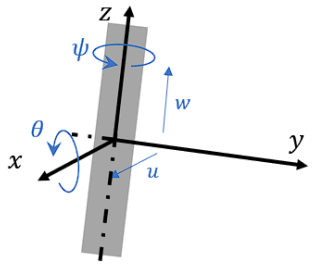

Figure II.14: DOF of a disk element

The displacement vector of the centre of the nodal disk is taken from the model:

$$\delta = [u, w, \theta, \psi]^T \tag{II.64}$$

By applying Lagrange's equation to equation II.21, we obtain:

$$\frac{d}{dt}\left(\frac{\partial T}{\partial \dot{\delta}}\right) - \frac{\partial T}{\partial \delta} = \underbrace{\begin{bmatrix} M_D & 0 & 0 & 0 \\ 0 & M_D & 0 & 0 \\ 0 & 0 & I_{D_x} & 0 \\ 0 & 0 & 0 & I_{D_x} \end{bmatrix}}_{M_D} \begin{Bmatrix} \ddot{u} \\ \ddot{w} \\ \ddot{\theta} \\ \ddot{\psi} \end{Bmatrix} + \Omega \underbrace{\begin{bmatrix} 0 & 0 & 0 & 0 \\ 0 & 0 & 0 & 0 \\ 0 & 0 & 0 & -I_{D_y} \\ 0 & 0 & I_{D_y} & 0 \end{bmatrix}}_{C_D} \begin{Bmatrix} \dot{u} \\ \dot{w} \\ \dot{\theta} \\ \dot{\psi} \end{Bmatrix} \tag{II.65}$$

With: M_D the Mass matrix and C_D the gyroscopic matrix.
Equation II.65 can therefore be written in the form:

$$\frac{d}{dt}\left(\frac{\partial T}{\partial \dot{\delta}}\right) - \frac{\partial T}{\partial \delta} = [M_D]\left\{\ddot{\delta}\right\} + \Omega\,[C_D]\left\{\dot{\delta}\right\} \tag{II.66}$$

II.6.1.2 Shaft

The symmetrical rotor shaft is designed using a beam with a fixed circular cross-section. The shaft was modelled using the classical finite element with two points and 4 DOF at each point (see Figure 14), which allows us to access 8x8-size basic element matrices.

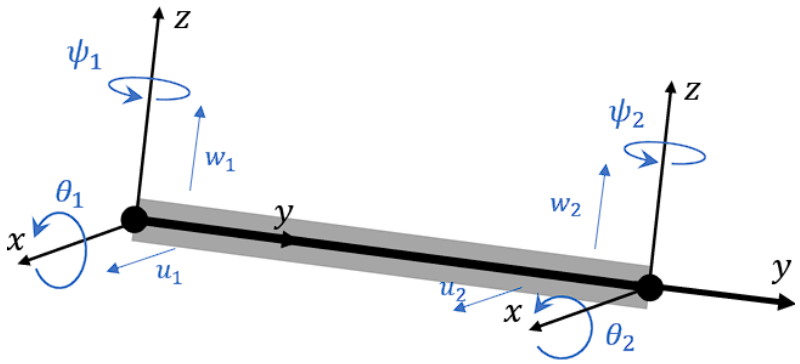

Figure II.15: DOF of a shaft element

The relationships between displacement and slopes are: ¨

$$\begin{cases} \psi = -\frac{\partial u}{\partial y} \\ \theta = \frac{\partial w}{\partial y} \end{cases} \tag{II.67}$$

and the vector of nodal displacements:

$$\delta = [u_1, w_1, \theta_1, \psi_1, u_2, w_2, \theta_2, \psi_2]^T \tag{II.68}$$

In addition, it includes the displacements δ_u and δ_w that correspond to movements in the x and y directions, respectively. ¨

$$\begin{cases} \delta_u = [u_1, \psi_1, u_2, \psi_2]^T \\ \delta_w = [w_1, \theta_1, w_2, \theta_2]^T \end{cases} \tag{II.69}$$

The finite element of the rotating shaft is constructed by expressing the displacements u and w as follows:

$$\begin{cases} u = N_1(y)\,\delta_u \\ w = N_2(y)\,\delta_w \end{cases} \tag{II.70}$$

where $N_1(y)$ and $N_2(y)$ are the vectors of the classical shape functions of a beam element in bending:

$$N_1(y) = \left[1 - \frac{3y^2}{L^2} + \frac{2y^3}{L^3}; -y + \frac{2y^2}{L} - \frac{y^3}{L^2}; \frac{3y^2}{L^2} - \frac{2y^3}{L^3}; \frac{y^2}{L} - \frac{y^3}{L^2}\right] \tag{II.71}$$

$$N_2(y) = \left[1 - \frac{3y^2}{L^2} + \frac{2y^3}{L^3}; y - \frac{2y^2}{L} + \frac{y^3}{L^2}; \frac{3y^2}{L^2} - \frac{2y^3}{L^3}; -\frac{y^2}{L} + \frac{y^3}{L^2}\right] \tag{II.72}$$

II.6.1.2.1 Shaft Kinetic Energy: The kinetic energy of the rotating shaft is expressed from equation II.26 which gives. in compact form.

$$\begin{aligned} T_s &= \tfrac{\rho S}{2}\int_0^L \left[\delta\dot{u}^T N_1^T N_1 \delta\dot{u} + \delta\dot{w}^T N_2^T N_2 \delta\dot{w}\right] dy \\ &+ \tfrac{\rho I}{2}\int_0^L \left[\delta\dot{u}^T \tfrac{dN_1^T}{dy}\tfrac{dN_1}{dy}\delta\dot{u} + \delta\dot{w}^T \tfrac{dN_2^T}{dy}\tfrac{dN_2}{dy}\delta\dot{w}\right] dy \\ &-2\rho I\Omega\int_0^L \delta\dot{u}^T \tfrac{dN_1^T}{dy}\tfrac{dN_2}{dy}\delta w dy + \rho I\Omega^2 \end{aligned} \tag{II.73}$$

Substituting equations II.71 and II.72 along with their derivatives into equation II.73 and performing integration, we obtain:

$$\begin{aligned} T_s &= {}^1\!/_2\delta\dot{u}^T M_1 \delta\dot{u} + {}^1\!/_2\delta\dot{w}^T M_2 \delta\dot{w} + {}^1\!/_2\delta\dot{u}^T M_3 \delta\dot{u} \\ &+ {}^1\!/_2\delta\dot{w}^T M_4 \delta\dot{w} + \Omega\delta\dot{u}^T M_5 \delta w + \delta I L\Omega^2 \end{aligned} \tag{II.74}$$

Where M_1 and M_2 represent the classical mass matrices, M_3 and M_4 represent the effects of rotational inertia, and the matrix M_5 represents the gyroscopic effect. Additionally, $\delta I L\Omega^2$ is the constant term. These matrices are as follows:

$$[M_1] = \frac{\rho SL}{420}\begin{bmatrix} 156 & -22L & 54 & 13L \\ -22L & 4L^2 & -13L & -3L^2 \\ 54 & -13L & 156 & 22L \\ 13L & -3L^2 & 22L & 4L^2 \end{bmatrix} \tag{II.75}$$

$$[M_2] = \frac{\rho SL}{420}\begin{bmatrix} 156 & 22L & 54 & -13L \\ 22L & 4L^2 & 13L & -3L^2 \\ 54 & 13L & 156 & -22L \\ -13L & -3L^2 & -22L & 4L^2 \end{bmatrix} \tag{II.76}$$

$$[M_3] = \frac{\rho I}{30L}\begin{bmatrix} 36 & -3L & -36 & -3L \\ -3L & 4L^2 & 3L & -L^2 \\ -36 & 3L & 36 & 3L \\ -3L & -L^2 & 3L & 4L^2 \end{bmatrix} \tag{II.77}$$

$$[M_4] = \frac{\rho I}{30L}\begin{bmatrix} 36 & 3L & -36 & 3L \\ 3L & 4L^2 & -3L & -L^2 \\ -36 & -3L & 36 & -3L \\ 3L & -L^2 & -3L & 4L^2 \end{bmatrix} \tag{II.78}$$

$$[M_5] = \frac{\rho L}{30L}\begin{bmatrix} -36 & -3L & 36 & -3L \\ 3L & 4L^2 & -3L & -L^2 \\ -36 & 3L & -36 & 3L \\ 3L & L^2 & -3L & 4L^2 \end{bmatrix} \tag{II.79}$$

Applying Lagrange's equations to express the kinetic energy of a rotating shaft, we find:

$$\frac{d}{dt}\left(\frac{\partial T}{\partial \dot{\delta}}\right) - \frac{\partial T}{\partial \delta} = (M + M_s)\,\ddot{\delta} + C\dot{\delta} \tag{II.80}$$

Where $[M]$ is obtained from $[M_1]$ and $[M_2]$, $[M_s]$ is obtained from $[M_3]$ and $[M_4]$, and the matrix $[C]$ comes from $[M_5]$. These matrices are:

$$M = \frac{\rho SL}{420}\begin{bmatrix} 156 & 0 & 0 & -22L & 54 & 0 & 0 & 13L \\ 0 & 156 & 22L & 0 & 0 & 54 & -13L & 0 \\ 0 & 22L & 4L^2 & 0 & 0 & 13L & -3L^2 & 0 \\ -22L & 0 & 0 & 4L^2 & -13L & 0 & 0 & -3L^2 \\ 54 & 0 & 0 & -13L & 156 & 0 & 0 & 22L \\ 0 & 54 & 13L & 0 & 0 & 156 & -22L & 0 \\ 0 & -13L & -3L^2 & 0 & 0 & -22L & 4L^2 & 0 \\ 13L & 0 & 0 & -3L^2 & 22L & 0 & 0 & 4L^2 \end{bmatrix} \tag{II.81}$$

$$M_s = \frac{\rho I}{30L}\begin{bmatrix} 36 & 0 & 0 & -L & -36 & 0 & 0 & -3L \\ 0 & 36 & 3L & 0 & 0 & -36 & 3L & 0 \\ 0 & 3L & 4L^2 & 0 & 0 & -3L & -L^2 & 0 \\ -3L & 0 & 0 & 4L^2 & 3L & 0 & 0 & -L^2 \\ -36 & 0 & 0 & 3L & 36 & 0 & 0 & 3L \\ 0 & -36 & -3L & 0 & 0 & 36 & -3L & 0 \\ 0 & 3L & -L^2 & 0 & 0 & -3L & 4L^2 & 0 \\ -3L & 0 & 0 & -L^2 & 3L & 0 & 0 & 4L^2 \end{bmatrix} \tag{II.82}$$

$$C = \frac{\rho I\Omega}{15L}\begin{bmatrix} 0 & -36 & -3L & 0 & & 36 & -3L & 0 \\ 36 & 0 & 0 & -3L & -36 & 0 & 0 & -3L \\ 3L & 0 & 0 & -4L^2 & -3L & 0 & 0 & L^2 \\ 0 & 3L & 4L^2 & 0 & 0 & -L^2 & -L^2 & 0 \\ 0 & 36 & 3L & 0 & 0 & -36 & 3L & 0 \\ -36 & 0 & 0 & 3L & 36 & 0 & 0 & 3L \\ 3L & 0 & 0 & L^2 & -3L & 0 & 0 & -4L^2 \\ 0 & 3L & -L^2 & 0 & 0 & -3L & 4L^2 & 0 \end{bmatrix} \tag{II.83}$$

II.6.1.2.2 Shaft Strain Energy: The strain energy of the rotating shaft is expressed from equation II.41 which gives. in compact form

$$U_s = \frac{EI}{2}\int_0^L \left[\delta u^T \frac{d^2N_1^T}{dy^2}\frac{d^2N_1}{dy^2}\delta u + \delta w^T \frac{d^2N_2^T}{dy^2}\frac{d^2N_2}{dy^2}\delta w\right]dy \tag{II.84}$$

After integration on U_s becomes:

$$U_s = {}^1\!/_2\delta u^T\left[K_1\right]\delta u + {}^1\!/_2\delta w^T\left[K_2\right]\delta w \tag{II.85}$$

where $[K_1]$ and $[K_2]$ are the classical stiffness matrices.The shear effect is not taken into account.

$$[K_1] = \frac{EI}{L^3}\begin{bmatrix} 12 & -6l & -12 & -6l \\ -6l & 4l^2 & 6l & 2l^2 \\ -12 & 6l & 12 & 6l \\ -6l & 2l^2 & 6l & 4l^2 \end{bmatrix} \tag{II.86}$$

$$[K_2] = \frac{EI}{L^3}\begin{bmatrix} 12 & 6l & -12 & 6l \\ 6l & 4l^2 & -6l & 2l^2 \\ -12 & -6l & 12 & -6l \\ 6l & 2l^2 & -6l & 4l^2 \end{bmatrix} \tag{II.87}$$

The elementary stiffness matrix of strain energy is as follows:

$$K = \frac{EI}{L^3}\begin{bmatrix} 12 & 0 & 0 & -6L & -12 & 0 & 0 & -6L \\ 0 & 12 & 6L & 0 & 0 & -12 & 6L & 0 \\ 0 & 6L & 4L^2 & 0 & 0 & -6L & 2L^2 & 0 \\ -6L & 0 & 0 & 4L^2 & 6L & 0 & 0 & 2L^2 \\ -12 & 0 & 0 & 6L & 12 & 0 & 0 & 6L \\ 0 & -12 & -6L & 0 & 0 & 12 & -6L & 0 \\ 0 & 6L & 2L^2 & 0 & 0 & -6L & 4L^2 & 0 \\ -6L & 0 & 0 & 2L^2 & 6L & 0 & 0 & 4L^2 \end{bmatrix} \tag{II.88}$$

It is often necessary to take into account the shear effect that modifies the classical stiffness matrix. It has the expression:

$$a = \frac{12EI}{GS_r l^2} \tag{II.89}$$

$$G = \frac{E}{2\left(1+\nu\right)} \tag{II.90}$$

With ν represents Poisson's ratio, S_r is the reduced section and G represents the shear modulus

Taking the effect of shear into account, the classical stiffness matrix becomes as

follows:

$$K = \frac{EI}{(1+a)\,L^3}\begin{bmatrix} 12 & 0 & 0 & -6L & -12 & 0 & 0 & -6L \\ 0 & 12 & 6L & 0 & 0 & -12 & 6L & 0 \\ 0 & 6L & (4+a)L^2 & 0 & 0 & -6L & (2-a)L^2 & 0 \\ -6L & 0 & 0 & (4+a)L^2 & 6L & 0 & 0 & (2-a)L^2 \\ -12 & 0 & 0 & 6L & 12 & 0 & 0 & 6L \\ 0 & -12 & -6L & 0 & 0 & 12 & -6L & 0 \\ 0 & 6L & (2-a)L^2 & 0 & 0 & -6L & (4+a)L^2 & 0 \\ -6L & 0 & 0 & (2-a)L^2 & 6L & 0 & 0 & (4+a)L^2 \end{bmatrix} \tag{II.91}$$

II.6.1.3 Mass unbalance

By applying the Lagrange's equations to the expression kinetic energy of the unbalance equation II.47, we find:

$$\frac{d}{dt}\left(\frac{\partial T}{\partial \dot{\delta}}\right) - \frac{\partial T}{\partial \delta} = -m_u d\Omega^2 \begin{bmatrix} \sin\Omega t \\ \cos\Omega t \end{bmatrix} \tag{II.92}$$

With:

$$\delta = [u, w]^T \tag{II.93}$$

II.6.1.4 bearing

The main characteristics of stiffness and damping are related to strength, deformations, and velocities; the influence of inclination and bending moment are usually ignored. The matrices were obtained directly from equation II.48 and II.49, which gives:

$$\begin{cases} F_u = -K_{xx}u - K_{xz}w - c_{xx}\dot{u} - c_{xz}\dot{w} \\ F_w = -K_{zz}w - K_{zx}u - c_{zz}\dot{w} - c_{zx}\dot{u} \end{cases} \tag{II.94}$$

As $F_\psi = F_\theta = 0$, we have:

$$\begin{Bmatrix} F_u \\ F_\theta \\ F_w \\ F_\psi \end{Bmatrix} = -\begin{bmatrix} k_{xx} & 0 & k_{xz} & 0 \\ 0 & 0 & 0 & 0 \\ k_{zx} & 0 & k_{zz} & 0 \\ 0 & 0 & 0 & 0 \end{bmatrix}\begin{Bmatrix} u \\ \theta \\ w \\ \psi \end{Bmatrix} - \begin{bmatrix} c_{xx} & 0 & c_{xz} & 0 \\ 0 & 0 & 0 & 0 \\ c_{zx} & 0 & c_{zz} & 0 \\ 0 & 0 & 0 & 0 \end{bmatrix}\begin{Bmatrix} \dot{u} \\ \dot{\theta} \\ \dot{w} \\ \dot{\psi} \end{Bmatrix} \tag{II.95}$$

The first matrix represents stiffness, and the second matrix represents the damping characteristics. These matrices are typically asymmetric and can vary significantly with changes in rotation speed (*i.e.*$k_{xz} \neq k_{zx}$ and $c_{xz} \neq c_{zx}$).

II.6.2 Equations of motion

The system of equations will be classically obtained by applying Lagrange's equations. The system of general equations of motion is given after collecting the initial matrices as follows:

$$[M]\left\{\ddot{\delta}\right\} + ([C] + [G(\Omega)])\left\{\dot{\delta}\right\} + [K]\{\delta\} = \{F(t)\} \tag{II.96}$$

With

$$F(t) = F_1 + F_2 \sin \Omega t + F_3 \cos \Omega t + F_4 \sin s\Omega t \\ + F_5 \cos s\Omega t + F_6 \sin \omega t + F_7 \cos \omega t \tag{II.97}$$

$\{\delta\}$ represents the vector containing all nodal displacements $[M]$ is the global symmetric mass matrix, $[C]$ is the global asymmetric damping matrix, $[G(\Omega)]$ is the global non-symmetric gyroscopic matrix, which is a function of the velocity Ω, and includes the gyroscopic effect, and $[K]$ is the global asymmetric stiffness matrix. $\{F(t)\}$ the force vector. includes a constant vector F_1. for example. to the gravity influence, F_2, F_3 and F_4, F_5 Representing respectively the mass unbalance and asynchronous forces, F_6 and F_7 Representing harmonic forces fixed in space.

II.7 Conclusion

In this chapter, our primary focus has been on modelling the dynamic behaviour of flexible rotors, analytically developing the equations of motion, enhancing our understanding of deformable rotors, and improving the modelling of various components in the model. We started with a simplified model by specifying its kinetic and strain energies, and then introduced the Rayleigh-Ritz method to shed light on the unique dynamic behaviour of rotors. This approach not only provided valuable insights but also contributed to our understanding of excitation responses. Furthermore, we delved into modelling the dynamic behaviour of flexible rotors using the finite element method, known for its accuracy in solving real systems. The finite element model was constructed by applying Lagrange's equations and extracting the relevant system characteristic matrices. However, it's worth noting that the most challenging aspect lies in solving the resulting equations. In the rotor dynamics literature, specialised solution methods like the Newmark method and the pseudo-conditional method are commonly employed.

CHAPTER III

Description and Design of the draft fan model FN 280

Contents

III.1 Introduction

In this chapter, a brief description of the rotor model to be studied in this thesis, namely the centrifugal fan FN280 cement suction, was presented. The various parts of the fan were designed by SOLIDWORKS 2022 software, except for the blade, because of the unavailability of its data and the impossibility of drawing it directly due to the complexity of its shape, so we relied on reverse engineering technology to create the 3D CAD model of the blade, and we analyzed the data obtained by comparing the scanning data and the CAD model using the GEOMAGIC CONTROL X 2022 softwar.

III.2 Description of draft fan

The studied rotor is a centrifugal fan of the FN280 type for transporting hot gases with limited granular content. It is of the suction type without an inlet box, and it works in the cement factory (see figure III.1 and figure III.2)

Figure III.1: Images of cement draft fan FN280

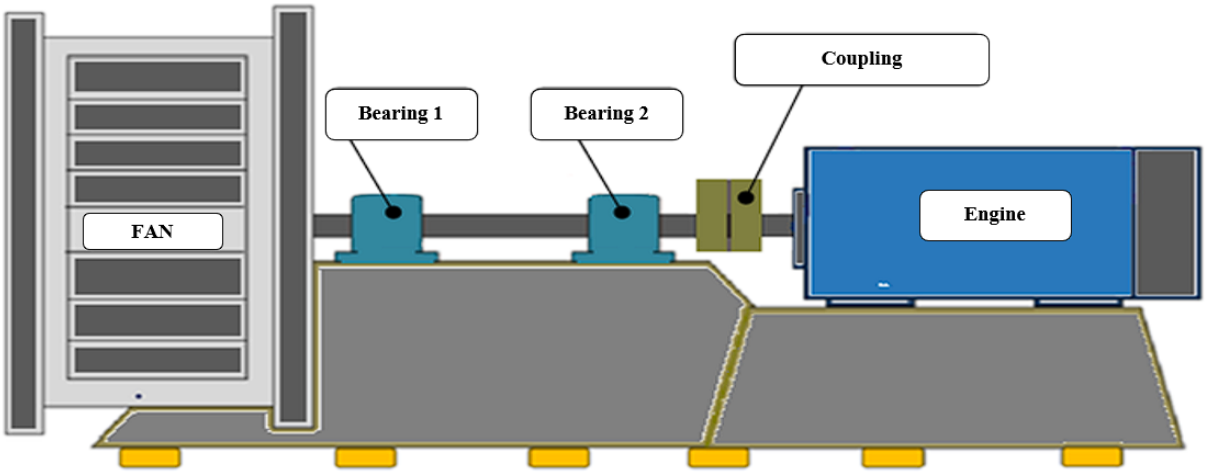

Figure III.2: Cement fan diagram

Figure III.3 is an assembly drawing of the fan, showing the fan's elements.

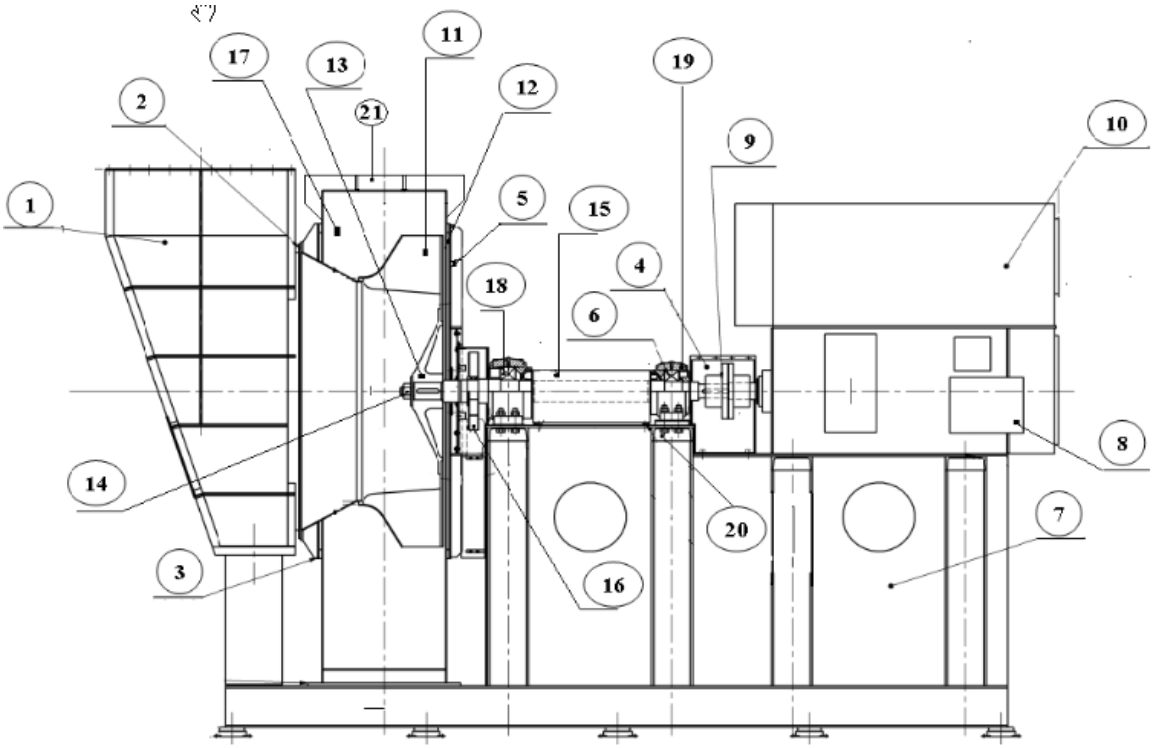

Figure III.3: Assembly drawing of the FN280 fan

- (01) Fan casing and outlet
- (02) Coned inlet
- (03) Conical dish (front cheek)
- (04) Cover coupling

- (05) Base (rear flange)
- (06) Bearing (22328/C3)
- (07) Motor pedestal
- (08) Motor
- (09) Flexible coupling
- (11) Impeller
- (12) Stuffing rope
- (13) Impeller mounting
- (14) Nut
- (15) Shaft
- (16) Cooling fan
- (17) Casing
- (18) Bearing (22332/C3)
- (19) Bearing cat housings FLS
- (20) Stool
- (21) Inspection hatch

The fan consists of the impeller (11) with assembly hub (13), shaft (15), cooling (16), bearing (18) and (06) and casing (17) with front flange (03), rear flange (05) and suction roof (02).

The impeller (11) is designed as a closed impeller consisting of a cast hub (13) to which the impeller itself is bolted.

The fit between shaft and hub (13) is a sliding fit, h/h. The impeller has undergone dynamic balancing.

The shaft is constructed of shaft steel. The bearing (18) and (06) have spherical thrust roller bearings. Basic designation 22332 with C3 sail for the bearing (18) and 22328 with C3 sail for the bearing (06). They are fretted onto the shaft. One of them, designed as a guide bearing, is mounted near the engine. The other is mobile in his body.

Both of these bearing are mounted in cast FLS bearing bodies (19), mounted on the stool (20). A cooling turbine (16) is mounted on the shaft near the casing since the fans must work at temperatures above 125°C. The fan casing is made up of the casing itself (17), front flange (03), rear flange (05) and suction roof (02). The fan casing, sealed with a packing rope (12), is equipped with an inspection batch (21). The front flange is bolted to the casing.

III.2.1 Technical characteristics of the FN280 fan

The propeller mainly consist of an ABB motor, a flexible coupling, and a turbine with blades mounted on a shaft equipped with two SKF bearing equipped with ball bearings on tapered rollers. Table III.1 and III.2 show the technical data for the propeller and motor.

Table III.1: Fan technical data

Type		FN280
Number of blades		16
Temperature		84°C
Speed		985 RPM
Roller bearings	bearing 1	22328/C3
	bearing 2	22332/C3

Table III.2: Motor technical data

Mark		ABB
Power		500 KW
Tension		11000 V
Weight		53 Kg
Intensity		33 A
Speed		995 RPM
Roller bearings	DE 1	6324/C3
	NDE	6326/C3

III.2.2 Principle of operation

Moving air from one location to another by creating a differential pressure that create an air current.

- The control motor drives the fan rotor
- The fan returns the air to the outside thanks to centrifugal force

- The creates a negative static pressure (Ps) at the fan inlet
- Atmospheric pressure (Pa) forces air into the inlet
- The air leaving the fan has positive pressure
- Total Pressure = Dynamic Pressure + Static pressure ($Pt = Ps + Pd$)

III.3 Modeling of rotor

To do numerical simulations of the dynamic behavior of the fan FN280, it requires the existence of a 3D CAD model of the fan. The SOLIDWORKS 2022 design software was chosen to design the various component parts of the fan except for the blade because there is no design for it or its own data, and given the geometric characteristics of the blade and its complexity, reverse engineering was used to create and develop a 3D CAD model for the FN280 fan impeller blade.

III.3.1 Revers engineering

Reverse engineering (RE), also called revers design, is a process used in various fields such as civil architectural, mechanical, ... etc. RE is generally defined as the process of making it possible to analyze an existing physical object to determine the specifications and designs needed to reproduce or modify it. It's a reverse design process. More specifically, reverse engineering is the basic concept of manufacturing a part based on it original or physical model without the use of a technical drawing [100].

RE in the field of mechanical engineering is defined as the activity through which it is possible to produce a CAD model (computer-aided design) of a physical object [101]. RE It is also considered a part of a comprehensive process that starts with digitizing the object to be studied and ends with generating a point cloud. Reverse engineering is related to the prototype, standards, or industrial needs. These fields use geometry. Return for various industrial reasons. The reverse engineering process goes through several stages to reach the final result, represented by a three-dimensional CAD model. Figure III.4 represents a simple diagram of the different stages of the reverse engineering process.

Figure III.4: Working process

III.3.2 The blade scanning using the CMM machines

In the process of scanning the FN280 intake fan blade, we employed a Coordinate Measuring Machine (CMM). In the process of scanning the FN280 intake fan blade, we employed a Coordinate Measuring Machine (CMM) (see Figure III.5). The measurements are obtained using a probe attached to it. The probe typically has a small ball at the end of the column with a known diameter. The measurement values are taken in the XYZ space after verifying the CMM connection, which has been programmed to make contact with the part to be scanned. The most common type of probe is a bridge that contains three axes (XYZ).

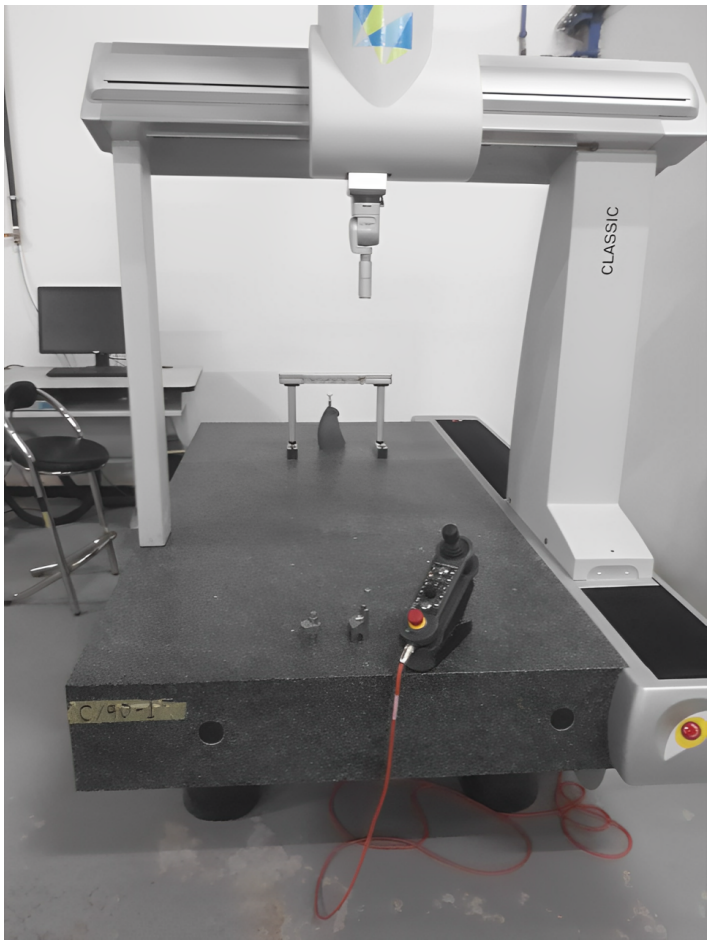

Figure III.5: Coordinate measuring machine (CMM)

Prior to commencing the blade scanning procedure, it was imperative to select the appropriate scanning tools, calibrate them, and establish the blade's position on the CMM table, as depicted in Figure III.6. The scanning data was acquired using a touch-trigger probe, which meticulously scanned both the upper and lower surfaces of the blade, including the engagement surface. Subsequently, the data collected during the scanning process was transformed into digital form, represented as a point cloud, the Figure III.7 digital data (point cloud) of the intake fan blade, utilizing the PC-DMIS program, showcasing a minimal standard deviation of 0.1 microns.

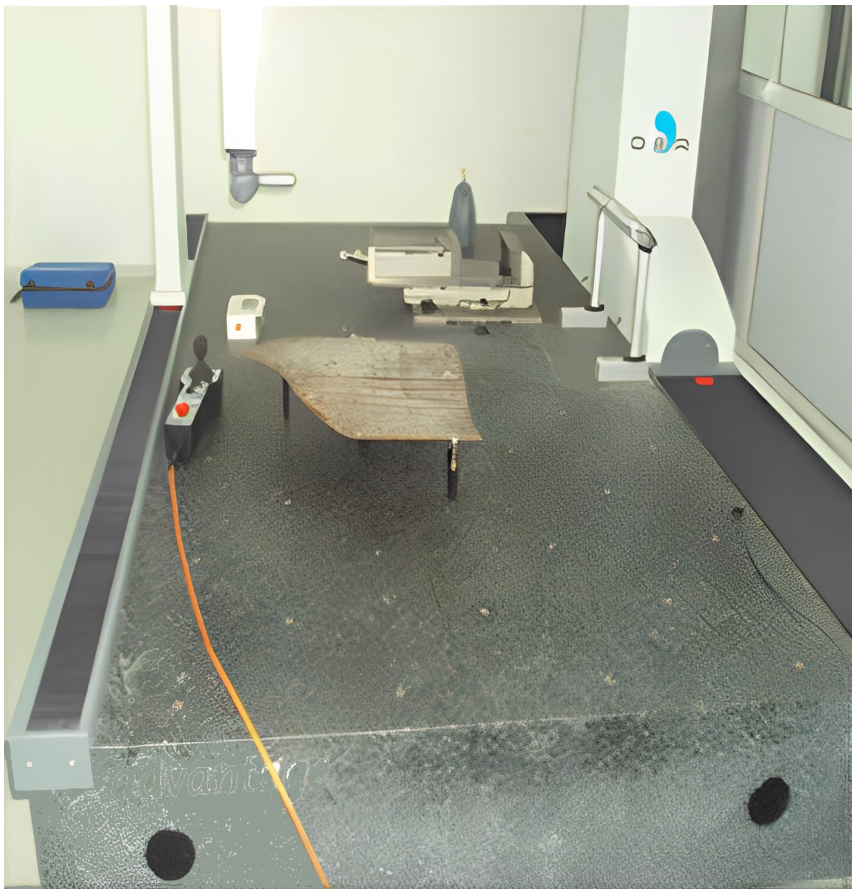

Figure III.6: Alignment of the fan blade on the CMM table

PC-DMIS is a CMM program used to measure various parts, from simple to complex sawn as the most complex aerospace and automotive components, and its user interface shows the position of the blade on the CMM table [102].

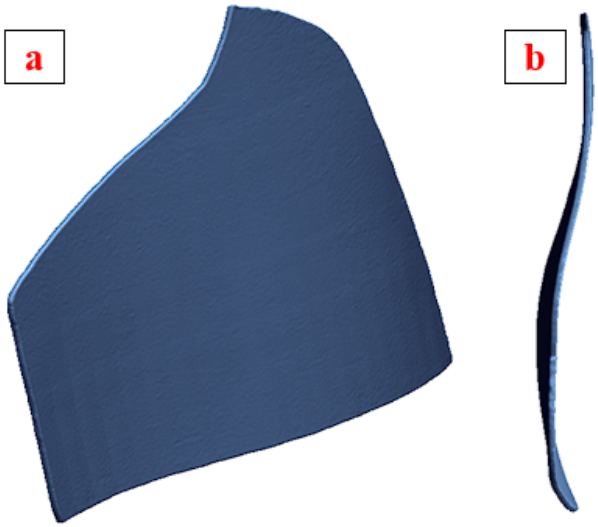

Figure III.7: digital data (point cloud) of the fan blade

After collecting the fan blade scan data and converting it into point cloud data using PC-DMIS software, the scans are saved in STL format. These STL files are then

exported to the scanning/revers engineering program for further processing, ultimately leading to the creation of the final CAD model of the fan blade. In our case, we employed the GEOMAGIC DESIGN X program, although other programs such as RAPIDFORM or GOM Inspect are available in the market.

III.3.3 3D modeling of the scanning data using GEOMAGIC DESIGN X 2019

3D scanning data, also known as a point cloud, is a data type consisting of a set of 3D vertices, with each vertex representing a specific position on the blade's surface. Since most 3D applications cannot directly utilize point cloud, they need to be converted into other formats, such as mesh or CAD models, typically through mesh modeling or revers design processes. In our case, we converted the point cloud data into a mesh using the CMM software , PC-DMIS.

In addition, this data is raw information, and the mesh must be optimized before starting to use the 3D scanning data provided by the CMM. This data is processed using features available in GEOMAGIC DESIGN X 2019 in order to optimize the mesh at the blade level.

This inverse design strategy depends on the type of scan data and the complexity of the shape. Since the surface of the FN280 intake fan blade is not uniform, the leading and trailing edge surface is distorted, causing the data to include distortions as well. We used a hybrid modeling technique in this process, which is a technique that relies on mixing both parametric modeling technique and surface mounting technique. This method consists of several sub-methods [103]. The surface mounting method was used, as it is a powerful method, it is necessary to clarify the mesh areas to apply the surface mounting technique. Therefore, we used the Auto Segment tool in the GEOMAGIC DESIGN X software automatically identify and detect surfaces, as shown in figure III.8.

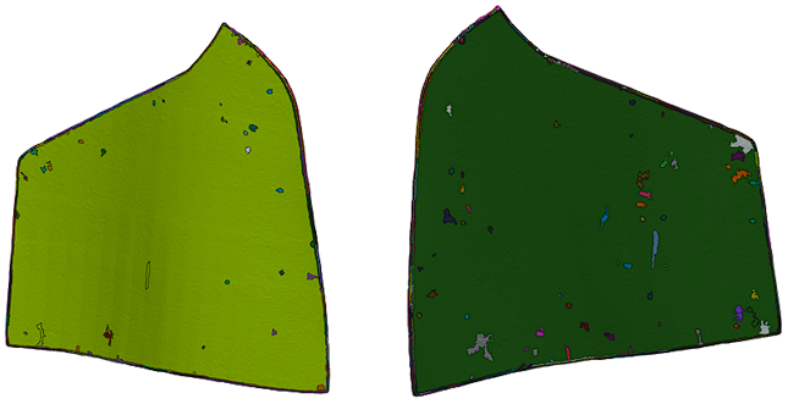

Figure III.8: Extract regions

To work with the surface installation technique, the mesh fit tool is used to create surfaces on the suction and pressure side of the FN280 fan blade. The permissible deviation is set to 0.0001, and the number of control point to 160 in order to better the ISO lines (see Figure III.9) in order to envelop the entire mesh area as is shown in Figure III.9c. As for creating the other surface of the blade, the leading surface and the shroud,

as shown in figure III.9d, it was done by creating a three-dimensional mesh drawing curve with nodes connected to concave mesh areas only.

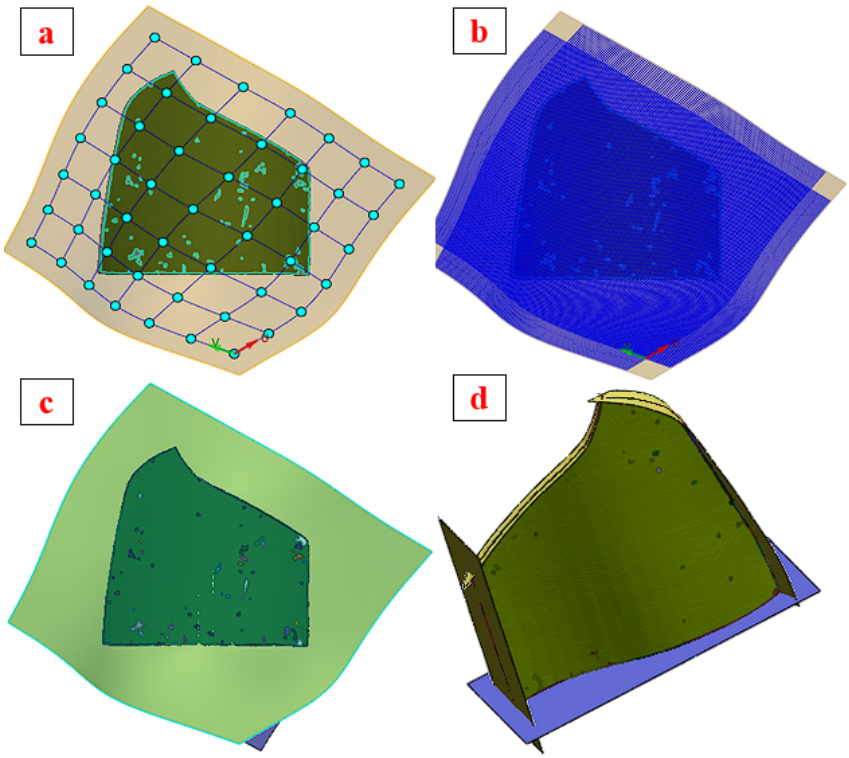

Figure III.9: Stages of creating Blade surfaces manually using mesh fit a) Fitting Region, b) ISO lines, c) surface fitting of suction and pressure side d)surface-cut

By feeding all the created surface and plans, a CAD model of the blade is obtained. Figure III.10a shows the blade model and figure III.10b shows the final CAD model of the fan blade.

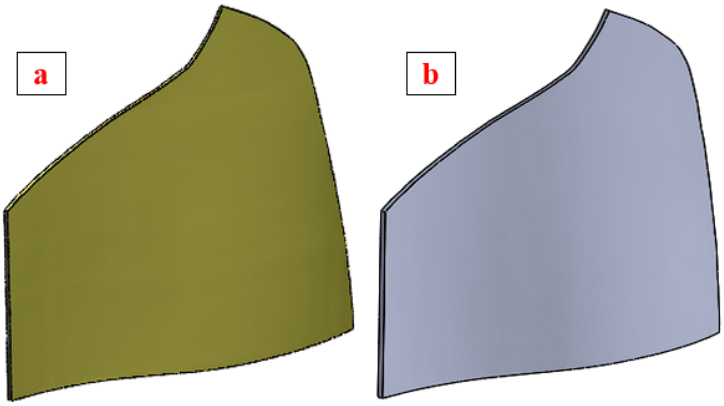

Figure III.10: a) The blade surfaces model final, b) The final CAD model of the fan blade

III.4 Accuracy analyses

The accuracy of the 3D CAD model of the suction fan blade, extracted from GEOMAGIC DESIGN X and created based on the data (point cloud) recorded by the CMM scanning

devise, was analyzed and evaluated using GEOMAGIC CONTROL X software, which is part of the GEOMAGIC software package. THE GEOMAGIC CONTROL X software is employed to monitor various dimensions of manufactured parts, aiding in the analysis of any part defects and facilitating the comparison of inspection results to ensure product quality. Additionally, it leverages 3D survey data to conduct precise dimensional measurements.

Before starting comparison and evaluating the accuracy of the model, you must retrieve the 3D CAD model of the blade and the STL file containing the scanned data of the blade of the GEOMAGIC CONTROL X as show in the figure III.11

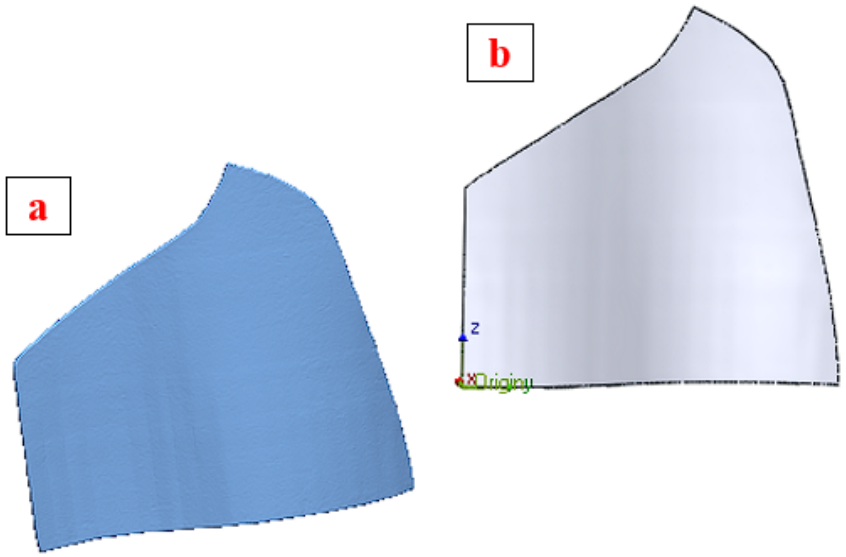

Figure III.11: a) cloud point , b) 3D CAD model of the blade

The initial step involves comparing the 3D model the blade with the scanned STL data file. Both the CAD and STL file need to be aligned. For this purpose, the GEOMAGIC CONTROL X software provides several specialized tools for automatic alignment. In this case, the initial Alignment tools was utilized, ensuring automatic alignment as depicted in the figure III.12a.

According to the report generated by the program and illustrated in Figure III.12b, the overall distribution of the line indicates that the maximum deviation of the measured data for the CAD model was +0.0785 mm, while the minimum deviation was -0.0785 mm, The average deviation for the entire CAD model was 0.0012mm. These small deviation values are considered acceptable, considering the functional requirements of the blade. Base on this information, the initial step of the analysis and evaluation process was successfully completed.

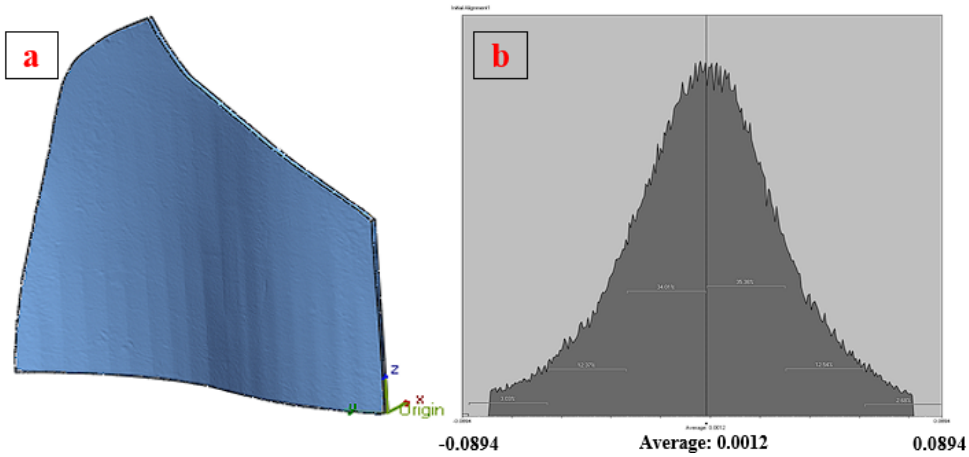

Figure III.12: a) alignment. b) Total distributions of 3D comparison errors

Using the 3D comparison tool 3D compare provided by the programme, which is used to verify the accuracy of the model by calculating and displaying the shape and shape of the deviation between the CAD and the STL file, the tool also allows us to adjust the allowable deviation. In our case, the allowable deviation of the model was set to -0.2 mm to +0.2 mm. The color diagram was displayed to show the accuracy levels of the different surfaces of the blade (see the figure III.13), where the in green indicates the surface that are within the previously specified tolerance limits, the range in red indicates the surface that have been modeled more than their original value, and the range in blue indicates the surface that have been modeled less than their original value.

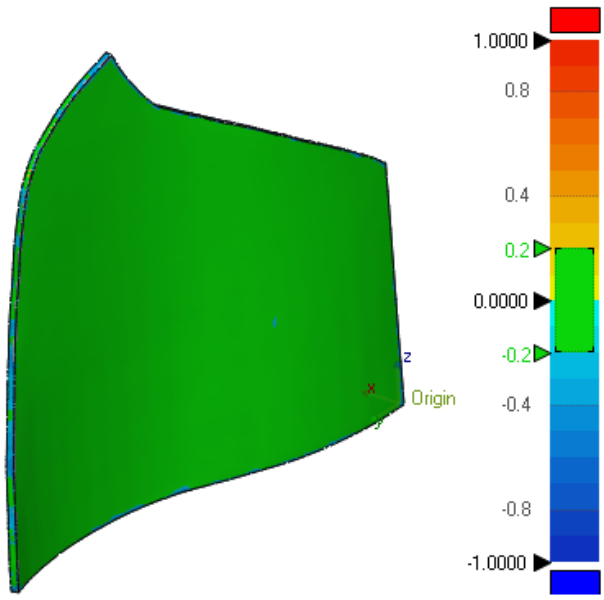

Figure III.13: 3D comparison deviation chromatograms

The 3D compare tool was also used to measure the deviation in 20 points at different locations on the blade surfaces, and also the points allow us to identify the position of the largest line as shown in Figure III.14, we note that there are some points where the deviation value is greater than the previously specified tolerance value, and most of the deviation values for these points are negative, and this indicates that they are in a blue-colored area where the surface that has been modeled is less than its original value, and

this is due to the foot of the blade and the scraping process to remove rust from the blade surfaces that was done before in addition, the areas where it has been determined that the error rate is large are at the bottom and top of the blade, which are areas that will be scanned It is welded to the fan assembly, so it does not affect the performance of the fan.

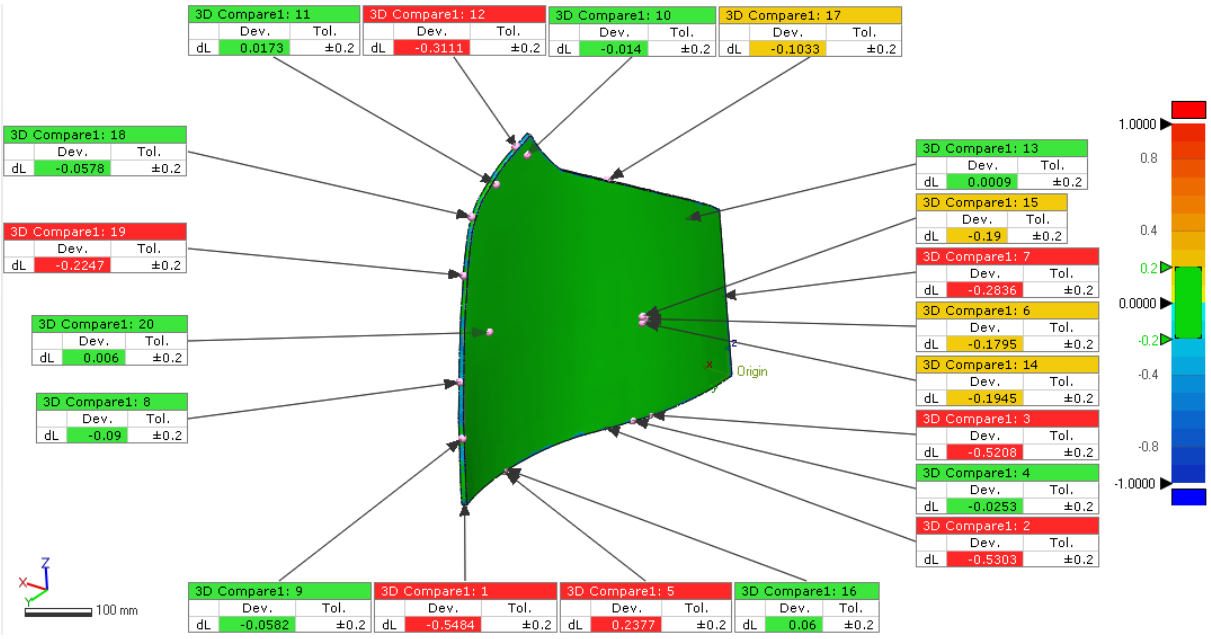

Figure III.14: 3D comparison deviation at 20 point

Figure III.15 shows the total distribution of the three-dimensional comparison line of the CAD model and the STL file of the blade. The figure also shows the deviation, the value of which was previously set from -0.2 mm to +0.2 mm, and the average error is -0.0061 mm. The error is distributed mainly in the range of -0.2166 mm to 0.202166 mm.

Table III.3 shows the total error of the CAD model. From the table, we can see that the reconstructed model has 2.3056% of the error, and 1.806% of it is less than the deviation decrease.

Table III.3: The total errors

Error		Deviation	
Maximum (mm)	-0.6092	Tolerance (%)	97.6944
Minimum (mm)	0.6092		
average (mm)	-0.0061	Out of tolerance (%)	2.3056
RMS	0.0704		
standard deviation	0.0702	Less than the lower deviation (%)	1.8066

Table III.4 taken from the report extracted from the CONTROL X program, where it shows the results of comparing the data from the 20 points previously specified in Figure III.14 so that it shows us the coordinates of each point on the CAD model on the XYZ axes and compares them with the coordinates obtained from the point cloud, which are significantly identical, and also shows the deviation values of each point.

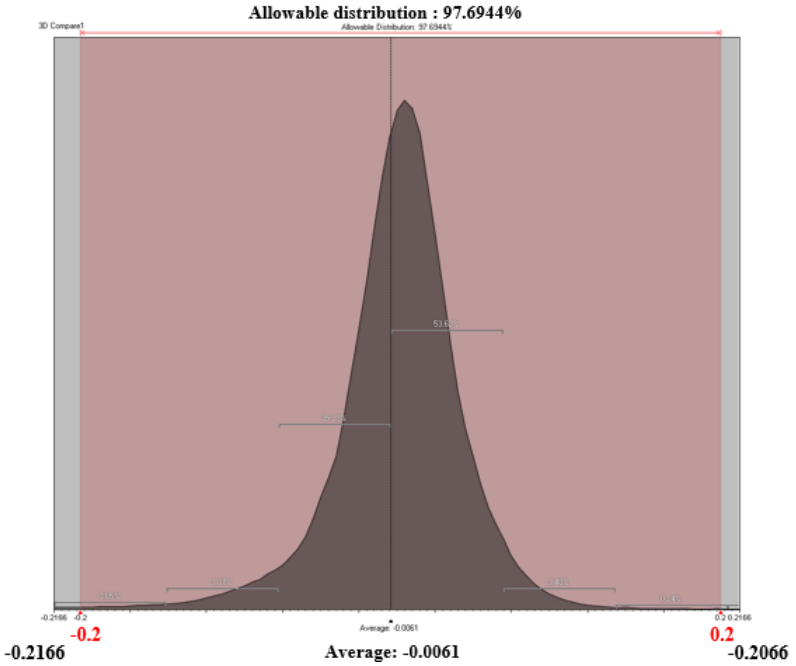

Figure III.15: The total distribution of the 3D comparison error

Name	Tol.	Dev.	Ref. Pos.			Meas. Pos.		
			X	Y	Z	X	Y	Z
3D Compare1: 1	±0.2	-0.5484	92.4823	523.0454	0	92.0929	522.941	0.3719
3D Compare1: 2	±0.2	-0.5303	59.2627	227.9211	0	59.1487	227.9792	0.5146
3D Compare1: 3	±0.2	-0.5208	24.2034	162.4855	-0.0818	24.1693	162.4991	0.4377
3D Compare1: 4	±0.2	-0.0253	35	190	0.0276	35.0226	189.9893	0.0237
3D Compare1: 5	±0.2	0.2377	102	416	0.1086	102.0225	416.0001	-0.128
3D Compare1: 6	±0.2	-0.1795	23.5243	160	160	23.6914	159.9347	159.9941
3D Compare1: 7	±0.2	-0.2836	4.2978	0.0001	130.0001	4.1397	0.2356	130.0025
3D Compare1: 8	±0.2	-0.09	100	506.1805	190	99.9681	506.0978	189.9847
3D Compare1: 9	±0.2	-0.0582	90	522.0359	105	90.0552	522.0189	104.9928
3D Compare1: 10	±0.2	-0.014	87.8035	332.2967	495.4345	87.8172	332.2941	495.4346
3D Compare1: 11	±0.2	0.0173	97.9174	396.9216	472.1828	97.9003	396.9217	472.1805
3D Compare1: 12	±0.2	-0.3111	96.1186	346.1707	512.8231	95.9744	346.0676	512.5674
3D Compare1: 13	±0.2	0.0009	12.9411	66.5431	286.8673	12.942	66.5429	286.8673
3D Compare1: 14	±0.2	-0.1945	25	164.1985	155	25.1808	164.1271	154.9937
3D Compare1: 15	±0.2	-0.19	25	163.3198	165	25.1768	163.2504	164.9937
3D Compare1: 16	±0.2	0.06	106.2613	410	0	106.2343	410.0006	-0.0535
3D Compare1: 17	±0.2	-0.1033	50.4288	193.9854	399.586	50.3414	194.0353	399.5629
3D Compare1: 18	±0.2	-0.0578	110.9234	441.8896	434.6657	110.8702	441.8717	434.6519
3D Compare1: 19	±0.2	-0.2247	110.8829	468.9684	348.6797	110.7666	468.7795	348.6441
3D Compare1: 20	±0.2	0.006	100	432.5836	240	99.994	432.5838	240.0001

Table III.4: Data taken from a report issued by the program shows the results of comparing the blade at 20 points

III.5 Assembling the rotor

After reverse engineering the fan blade and creating a 3D model of the blade using GEOMAGIC Design X and confirming the accuracy of the blade using GEOMAGIC Control X, 3D models of the rotor components were created to study the dynamic behavior. The SOLIDWORKS program was used to design the main parts shown in Figure III.16,figure III.17, figure III.18, figure III.19 which were also assembled in the same program as shown in figure III.20.

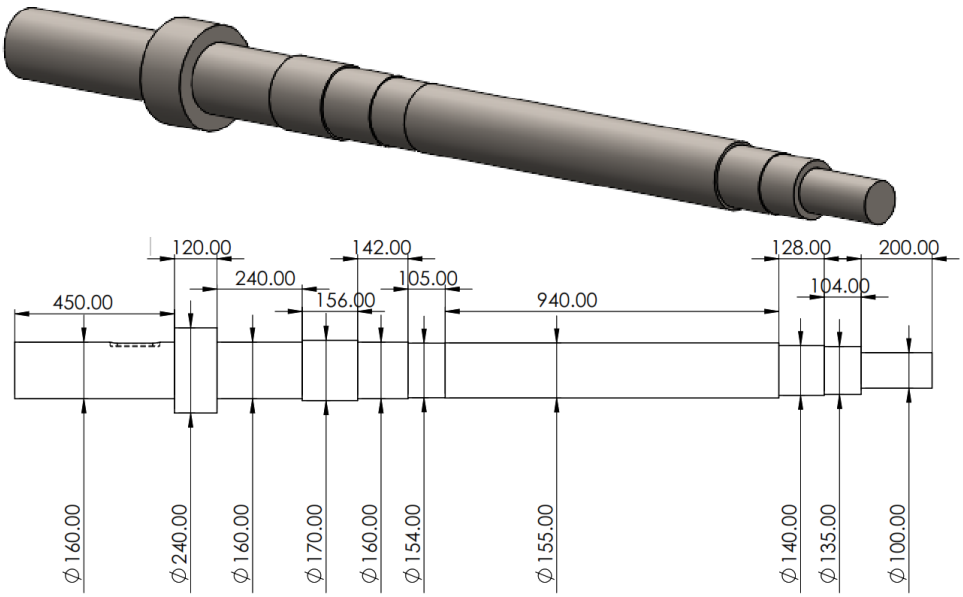

Figure III.16: Rotor shaft

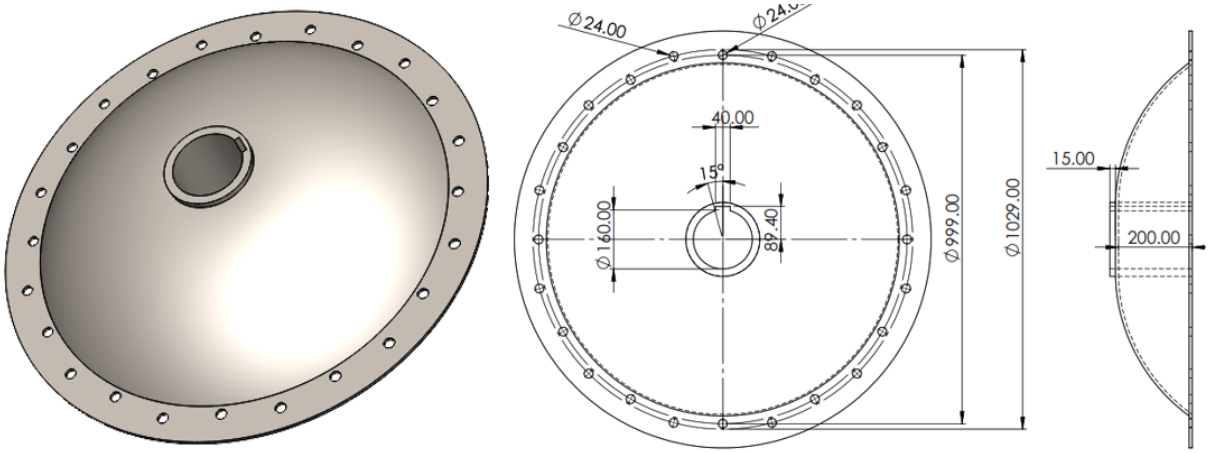

Figure III.17: Moyou

Figure III.18: Frontplate

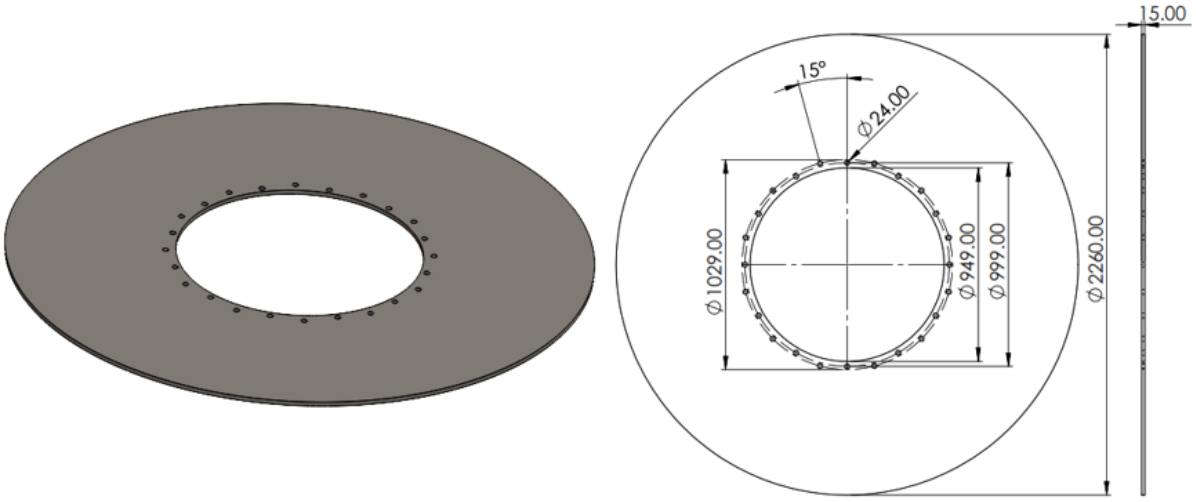

Figure III.19: backtplate

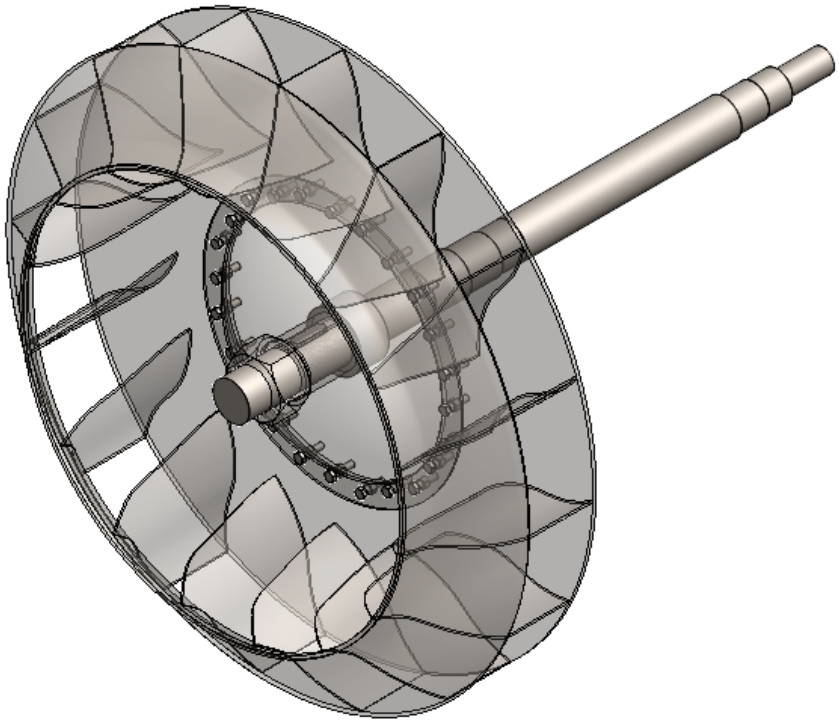

Figure III.20: FN280 centrifugal fan

III.6 Conclusion

This chapter provides a brief description of the rotor under study, which is the FN280 centrifugal fan. Using SolidWorks, we designed all the fan parts except for the impeller blade. Due to the lack of a CAD model and the complexity of its geometric shape, we designed the impeller blade through reverse engineering. The CMM scanned the blade and exported the scanning data to GEOMAGIC Design X. We analyzed any errors and

deviations that may have occurred during this process.

The study showed that the CMM measuring machine greatly helps in obtaining all the complex geometric details of any engineering object with very high accuracy, which leads to reducing the time required for design, provided the correct invention of the modeling strategy.

CHAPTER IV

Numerical simulation of the dynamic behavior of an industrial rotor (cement drag fan FN 280)

Contents

IV.1 Introduction

Numerical simulation has been known for a long time as one of the most important tools used to calculate structural dynamics and vibrations, especially after the technological advances that have occurred in the field of computation and computational machinery. Nowadays, there are many diverse programmes that allow dynamic calculation and simulation of rotating structures. We mention some of these programmes, such as ANSYS, ABAQUS, and COMSOL, in addition to MATLAB and others.

In our study, the numerical calculation code ANSYS was used, which is considered one of the most effective and widely used programs. Its analysis is based on the FEM to solve various problems in many industrial fields. In recent years, the computational capabilities of rotational dynamics have greatly improved, taking into account the needs of analysis and reducing computational time.

The main objective in this part of the study that we conducted was, on the one hand, to understand the vibration and dynamic behavior of the rotation represented in the cement extraction fan that was referred to in the previous chapter, and on the other hand, to study the effect of the wear of the fan blades on the critical speeds by conducting a modal analysis and harmonic analysis as mentioned in this chapter.

IV.2 Frame of reference in ANSYS

To analyze rotating structures, the choice of the frame of reference is very important. This choice determines the type of analysis that can be conducted, as additional conditions emerge in the equations of motion based on the selected reference frame. The ANSYS program provides two types of reference frames: a fixed reference frame and a rotating reference frame [61, 72, 104].

IV.2.1 Stationary frame of reference (SRF)

The use of a stationary reference frame means that the reference analysis system is attributed to the global coordinate system, which is considered a fixed coordinate system. where the gyroscopic moments resulting from the nodal rotation are included in the damping matrix in this analysis system, and from it, the equation of movement becomes of the form:

$$[M]\{\ddot{u}\} + ([C] + [C_{gyro}])\{\dot{u}\} + ([B] + [K])\{u\} = \{f\} \tag{IV.1}$$

Where $[M]$ is the mass matrix, $[K]$ is the stiffness matrix, $[C]$ is the damping matrix, $[C_gyro]$ is the gyroscopic matrix, and $[B]$ is the rotating damping matrix.

IV.2.2 Rotating frame of reference (RRF)

The use of a rotating reference frame means that the analysis reference system is linked to a rotating coordinate system, where all parts of the model rotate at the same rotation speed, and the coordinate system itself is also rotated. The equation of movement for the rotating reference frame is modified due to the inclusion of the Coriolis term, describing

angular velocities and accelerations. Therefore, the modified equation of movement for the rotor is as follows:

$$[M]\{\ddot{u}\}([C]+[C_{cori}])\{\dot{u}\}+([K]+[K_{spin}])\{u\}=\{f\} \quad \text{(IV.2)}$$

Where $[M]$ is the mass matrix, $[K]$ is the stiffness matrix, $[C]$ is the damping matrix, $[C_corio]$ is the Coriolis matrix, and $[K_spin]$ is spin softening matrix.

IV.2.3 The difference between a rotating and stationary frame of reference

There is a significant difference between the stationary reference frame and the rotating reference frame used in the ANSYS software. Table IV.1 provides a brief comparison between them.

Table IV.1: The difference between a Stationary and rotating frame of reference

Stationary frame of reference	**Rotating frame of reference**
The structure should be symmetrical about the axis of rotation.	Structure does not need to be axisymmetric about the axis of rotation.
It cannot use static analysis	Can use static analysis
Campbell's diagram can be used	Campbell's diagram cannot be used
It supports rotating structures that rotate at different speeds, each on a different axis of rotation	Supports only one rotating structure
Only one part can rotate and the other can be stationary	All parts in the model rotate

IV.3 Types of rotor dynamic analysis in ANSYS Workbench

Dynamic analysis is a technique used to determine the dynamic behavior of a structure or component, especially when the structure's inertia (mass effect) and damping are significant important role. In ANSYS calculation code, there are three types of dynamic analysis:

IV.3.1 Modal analysis

Modal analysis is performed to determine and study vibration characteristics, which include natural frequencies and modes shapes, and this information is one of the key parameters in the design of structures for dynamic analysis conditions. With regard to rotating structures, modal analysis can predict the vibration behavior of the rotating structure. It introduces the effect of gyroscopic forces resulting from rotational speeds "In this conditional system. These effects lead to a change in the damping of the system, and the damping can also be changed when a bearing is present. Since the natural frequencies change with rotational speed, it makes it difficult to calculate the correct natural frequencies for multi-bearing rotor systems [105].

IV.3.2 Harmonic response analysis

Performing harmonic analyses allows us to determine and study the response of the rotating structure to a harmonic force that varies sinusoidal over time, allowing us to verify whether the rotating structure design will successfully avoid resonance and other harmful forced vibration effects. In ANSYS, there are three methods to calculate the response of harmonic forces: the full method, the reduced method, and the mode superposition method. Here we will focus on describing the full method and the mode superposition method only, as they operate within the fixed reference framework that has been used in all models presented in this thesis.

IV.3.2.1 The full method

The complete method is used to obtain the harmonic response through a direct solution of the simultaneous equations of motion. In addition, this method enables us to relate conformational analysis to structural responses to static structural analysis [106].

The full method is the easiest to use, as it does not require consideration of any major degrees of freedom as in other methods. It uses the mass matrix completely without approximations and makes use of the same solvers as static calculation procedures. The complete method allows us to solve problems with symmetric and asymmetric matrices.

Since tolerance problems have non-symmetric matrices, and when the shapes of the elements are not ideal, this method works well. For these reasons, this method was used to solve rotor dynamics problems in this thesis. Although this method takes longer to perform calculations because it requires a large amount of computer memory, it provides high accuracy. It also does not allow for linear planning.

IV.3.2.2 The Mode Superposition method

The mode superposition method is one of the methods through which the response of harmonic forces can be used by performing the necessary linear combinations of the eigen solutions obtained by using modal analysis to obtain the mode shapes. This makes the mode superposition method much faster than other methods of solving most problems. This method also allows the application of element loading applied in the modal analysis to the harmonic analysis.

Since the rotational speed is not constant, as positions change with speed due to the gyroscopic effect, this method allows only a constant rotational speed to be applied. In addition, the Coriolis effect cannot be activated. Therefore, it is preferable to choose the complete method to solve problems and study the behavior of rotor dynamics.

IV.4 Rotor dynamic analysis methodology using ANSYS Workbench

To perform numerical simulations of rotary dynamics analysis using the ANSYS Workbench in general, a series of steps or procedures must be followed. These steps can be

represented in a flowchart of rotary dynamics analysis using the ANSYS Workbench figure IV.1.

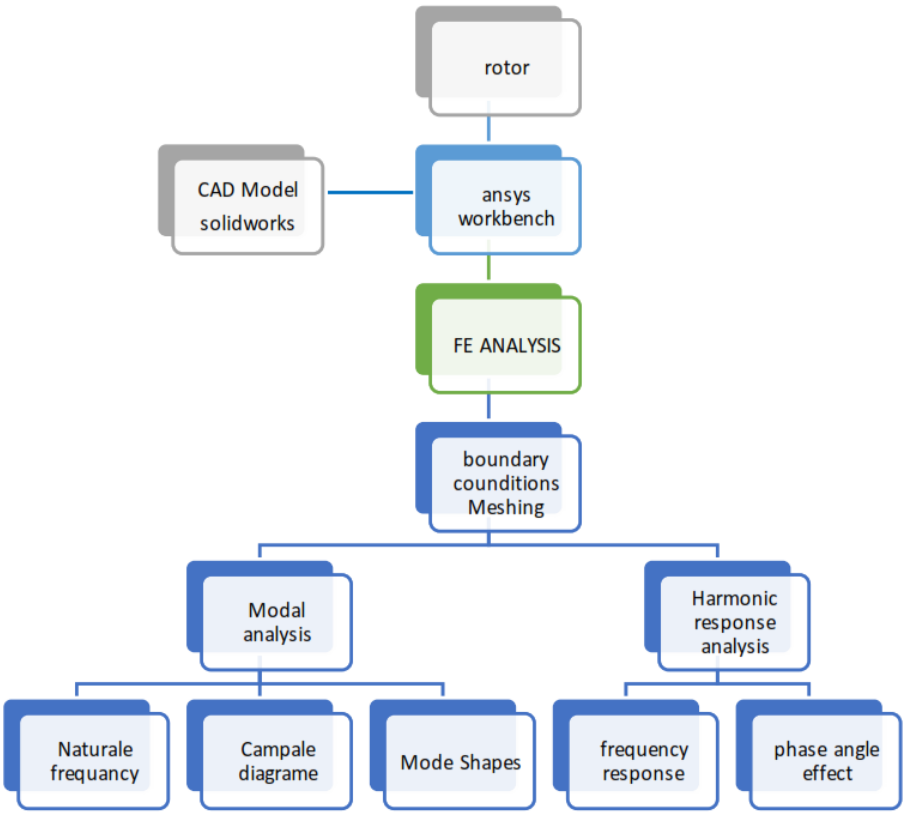

Figure IV.1: Rotor dynamic analysis methodology using the ANSYS Workbench

IV.5 Boundary conditions

IV.5.1 For Modal analysis

After modeling the rotor structure (see Chapter 3) and importing it into ANSYS Workbench, we will explain the boundary conditions that can be applied depending on the operating conditions of the rotor model being studied. We will apply these conditions in the case of integrity of the fan blades and in another case when the blades are damaged as a result of corrosion.

We will restrict the rotational and transnational movements on the Z axis (axis of rotation) and keep the rotational and transnational movements on the X and Y axes free by applying the remote displacement condition at the location of each bearing. Bearings were created on the bearing ground on the connection context tab in the X-Y plane. The bearings are also marked on their positions on the shaft, and additionally, data on the stiffness and damping for each bearing is entered, as shown in Table IV.2, as Figure IV.2 shows the boundary conditions of the rotor.

Considering that the rotation speed of 985 rpm is the operating speed of the rotor (centrifugal fan FN280), the modal analysis was performed using three different speeds.

The first speed is estimated at 100 rpm, the second speed is estimated at 600 rpm, and finally the third speed is estimated at 1200 rpm.

Table IV.2: Bearing data

bearing	Stiffness	Damping
Bearing 1	K11= 32000[k/mm]	C11= 3.3[N. s/mm]
	K22 =12000[k/mm]	C22 =1.5[N.s/mm]
Bearing 2	K11 =38900[k/mm]	C11= 2.6[N. s/mm]
	K22 =16000[k/mm]	C22 =1.5[N.s/mm]

IV.5.2 For harmonic response

Harmonic response analysis applies the same boundary conditions for displacement operations as applied in modal analysis, where we have restricted the retracting rotational movements on the Z-axis and kept them free to the X-axis and Z-axis by applying the remote displacement condition at the location of each bearing. The simulation of harmonic response analysis was carried out in a frequency domain starting from 0 to 70 Hz. This domain was specifically selected due to the values of natural frequencies obtained through modal analysis, and 2.333 Hz was set as a step size for a total of 30 steps. To extract results at critical frequencies, due to the possibility of resonance and variation in masses due to cement dust, the blades are asymmetric in mass, so they were converted into a point mass located in the center of the position of mass, where an unbalanced force was applied to the center of the disk in both cases in order to study its effect on the fan when the blades are worn.

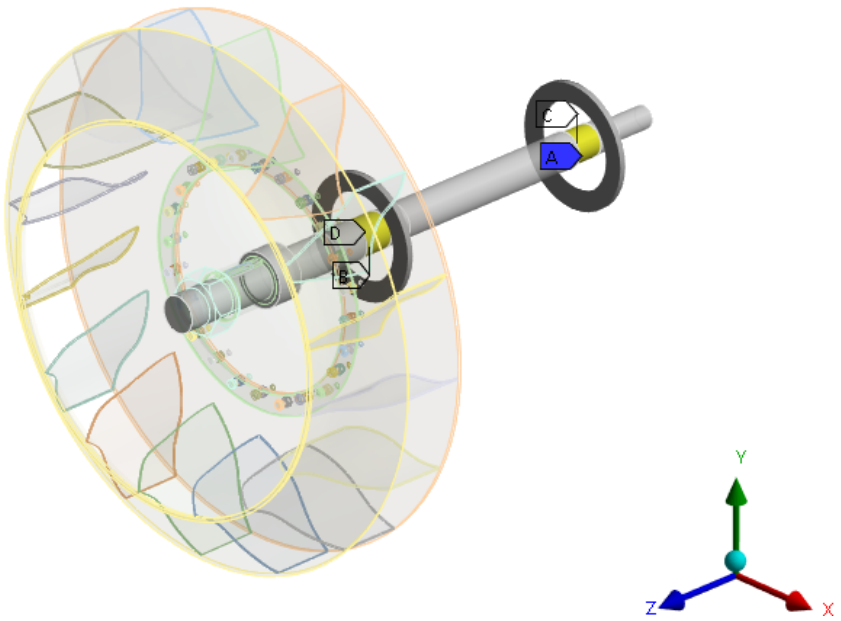

Figure IV.2: Boundary conditions applicable to the rotor

IV.6 Meshing

The meshing process is a critical and important process within ANSYS, so it must be accurate to obtain a simulation with accurate results using FEM. The grid consists of elements with nodes that are used to represent the geometric figure, and they vary according to the type of element used.

By using the principle of performing calculations within a limited number of elements and interpolating the results to the entire volume, it may pose a challenge if it is a continuous object due to the large number of degrees of freedom enjoyed by any continuous object; however, the strategic use of the meshing process proves its effectiveness in reducing degrees of freedom and preventing them from becoming infinite. Several meshing methods are available in ANSYS Workbench including among them are mechanical method, tetrahedra method and hexahedra dominances method [107, 108].

The shaft components have been meshed using element type SOLID185, which can be utilized in mixed forging to simulate deformations of nearly in-compressible elastic material (see figureIV.3). For blade modeling, the parts contact surfaces are initially built using the CONTA174 and TARGT170, elements and the connected individually. Additionally, the bearings are meshed using the COMBI214 element [109].

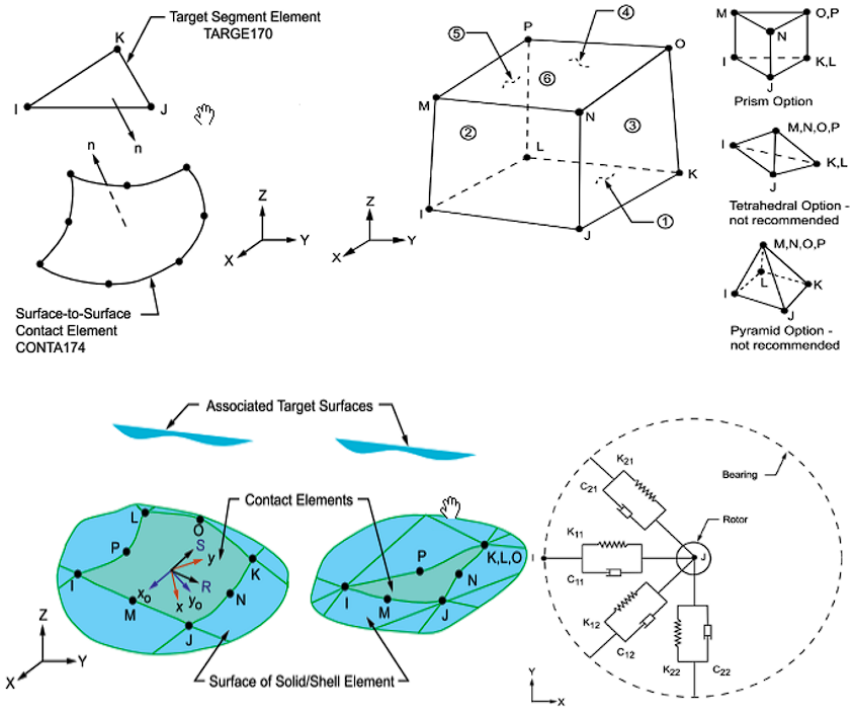

Figure IV.3: Types of elements used in the meshing process

A meshing of the model contains 531.890 elements and 239.491 nodes, as seem in the figure depicted in figure IV.4.

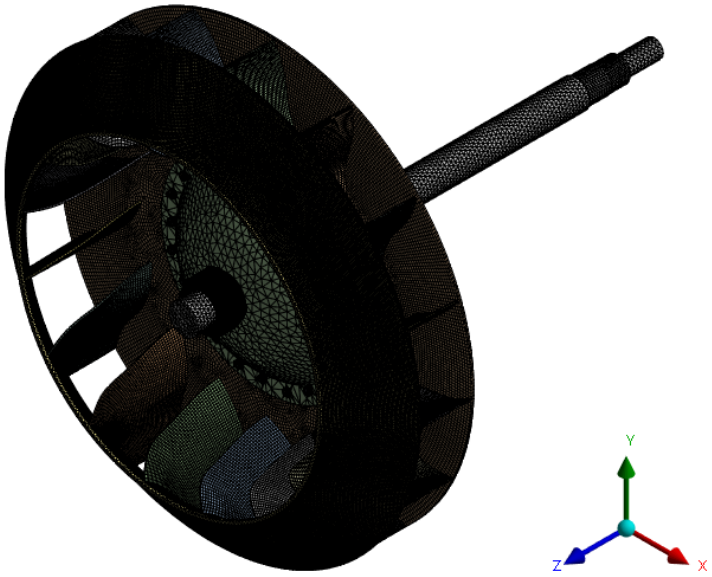

Figure IV.4: Full image for mesh rotor

IV.7 Results

IV.7.1 Modal analysis

Numerical simulation of modal analysis was carried out using different speeds: 100 rpm, 600 rpm, and 1200 rpm. These speeds were chosen due to the fact that the rotor's operating speed is 985 rpm. Four modes were identified at each speed, which were considered sufficient for conducting the modal analysis. Based on these parameters, the natural frequencies of the rotor were extracted, as shown in the table IV.3. The Campbell diagram was also extracted, and it was noted that the values of the recorded frequencies are close except for the frequency recorded in the fourth mode at a speed of 1200 RPM, where the value of the natural frequency was higher than the values in the other modes.

Table IV.3: Natural frequencies

mode number	Rotation speed [RPM]	Natural frequency [Hz]
1	100	12.775
2		16.857
3		27.826
4		30.153
1	600	12.712
2		16.677
3		23.338
4		36.52
1	1200	12.448
2		15.911
3		19.959
4		45.71

IV.7.1.1 The Campbell diagram

The modal analysis of the rotor allows us to extract the Campbell diagram shown in Figure IV.5, which is used to examine the evolution of natural frequencies relative to the different rotational speeds of the rotor and also allows us to extract critical speeds; in addition, it determines the threshold of stability.

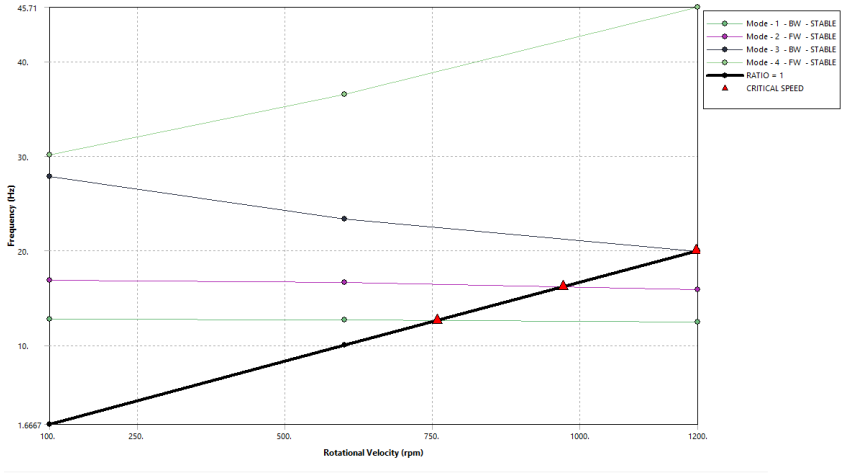

Figure IV.5: Campbell Diagram

After obtaining the Campbell diagram, it was noted that there are three critical speeds: the first is estimated at about 758.54 rpm with a natural frequency of 12.775 Hz; the second is 972.12 rpm with a natural frequency of 16.667 Hz; and the last is estimated at 1198.2 rpm with a frequency of 19.959 Hz is close to that of the manufacturer (1280 RPM), with an error of 6.4 %. It was also noted that the rotor is in a stable state, as shown in Table IV.4. Besides, the table also shows the values indicating the stability and rotation in each mode.

Table IV.4: Critical speeds and mode stability

Mode	**Whirl Direction**	**Mode Stability**	**Critical Speed**	**100. rpm**	**600. rpm**	**1200. rpm**
1	BW	STABLE	758.54 rpm	12.775 Hz	12.712 Hz	12.448 Hz
2	FW	STABLE	972.12 rpm	16.857 Hz	16.677 Hz	15.911 Hz
3	BW	STABLE	1198.2 rpm	27.826 Hz	23.338 Hz	19.959 Hz
4	FW	STABLE	NONE	30.153 Hz	36.52 Hz	45.71 Hz

IV.7.1.2 Mode Shapes

Figures IV.6, IV.7, and IV.8 show the modes shapes (rotor vibration modes) obtained from the modal analysis at various speeds of 100 rpm, 600 rpm, and 1200 rpm, respectively.

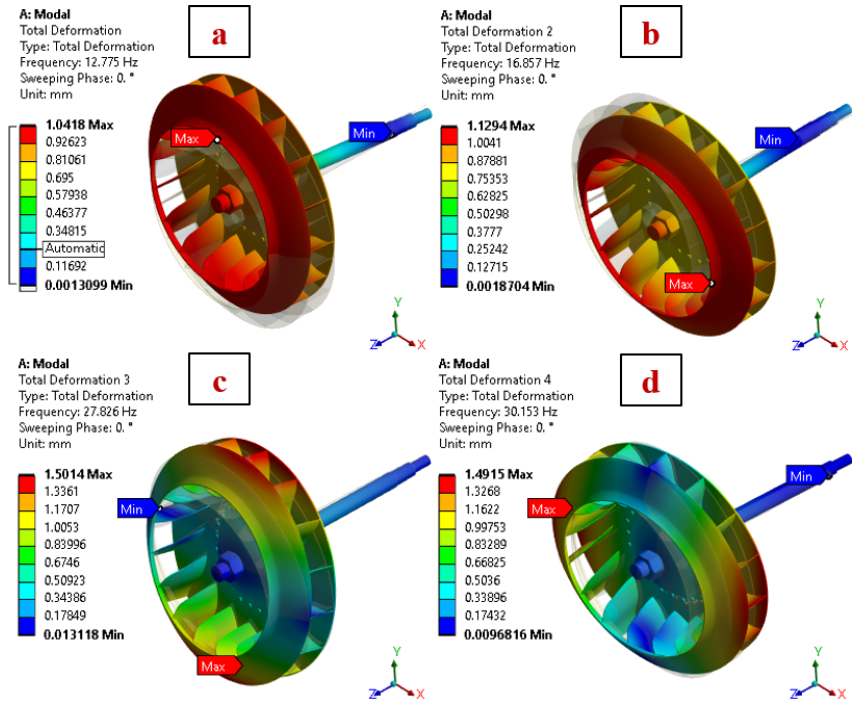

Figure IV.6: Mode shapes at a rotation speed of 100 rpm: a) Mode 1, b) Mode 2, c) Mode 3, d) Mode 4

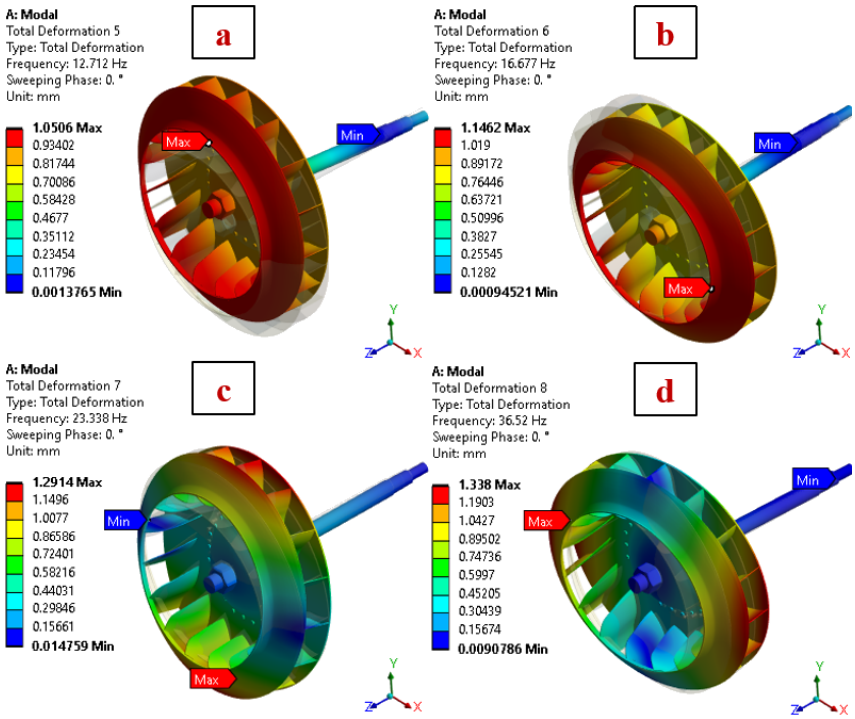

Figure IV.7: Mode shapes at a rotation speed of 600 rpm: a) Mode 1, b) Mode 2, c) Mode 3, d) Mode 4

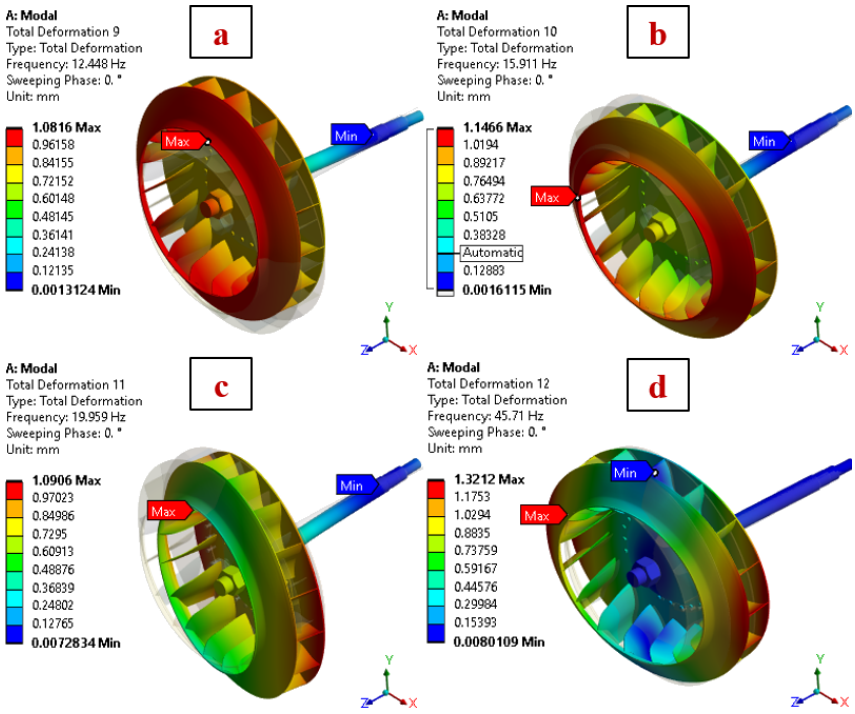

Figure IV.8: Mode shapes at a rotation speed of 1200 rpm: a) Mode 1, b) Mode 2, c) Mode 3, d) Mode 4.

Regarding the vibration mode obtained from the results, it was observed that the maximum deformation remains constant at all different rotation speeds. The maximum deformation occurs at a rotation speed of 100 rpm, with a value ranging from 1.0418 mm to 1.5014 mm from the first to the fourth mode.
As for the rotation speed of 600 rpm per minute, the maximum value of deformation is from 1.0506 to 1.338 mm from the first to the fourth mode, and the third rotation speed of about 1200 revolutions per minute is from 1.0816 to 1.3212 mm from the fourth mode. The results show us that the maximum deformation value in different vibration modes and different speeds is very small compared to the size of the rotor.

IV.7.2 Harmonic analysis

The analysis of the harmonic response of the rotor allowed us to determine its deformation and interface, and the effect of the phase angle resulting from the balanced and unbalanced forces that effect on the rotor system was extracted from the simulation results. In addition, a harmonic response analysis was performed to show the frequency response resulting from the application of an unbalanced force of 12.5 kg.Mm

IV.7.2.1 Frequency response

The figures IV.9, IV.10, and IV.11 show the results of the deformation amplitude resulting from the simulation of harmonic response analysis in the X-axis, Y-axis, and Z-axis directions.

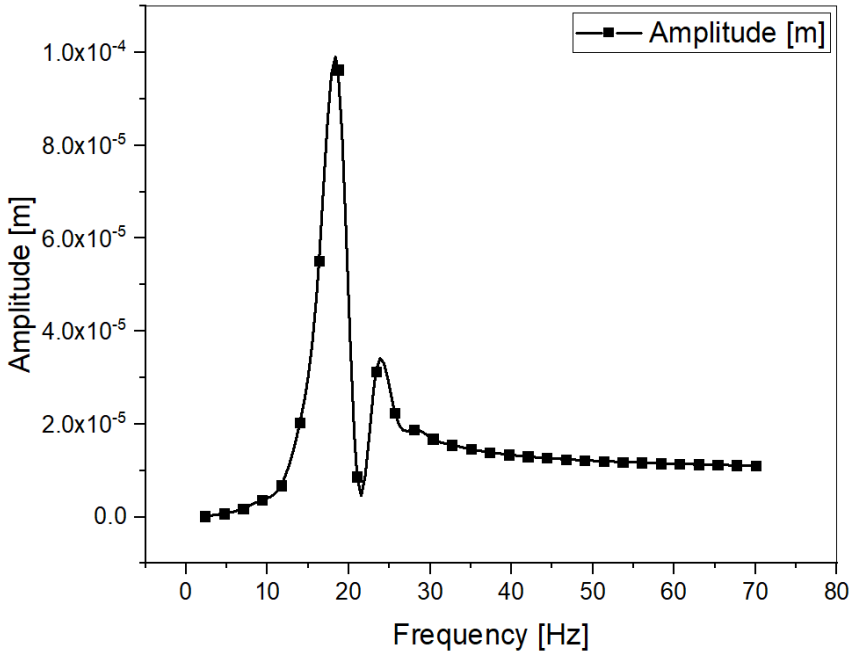

Figure IV.9: Frequency response on X

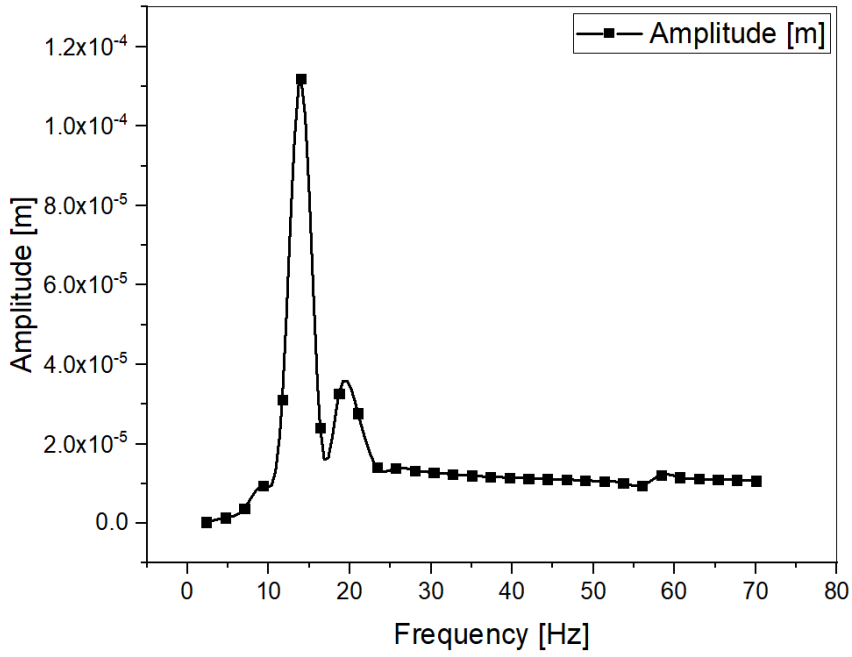

Figure IV.10: Frequency response on Y

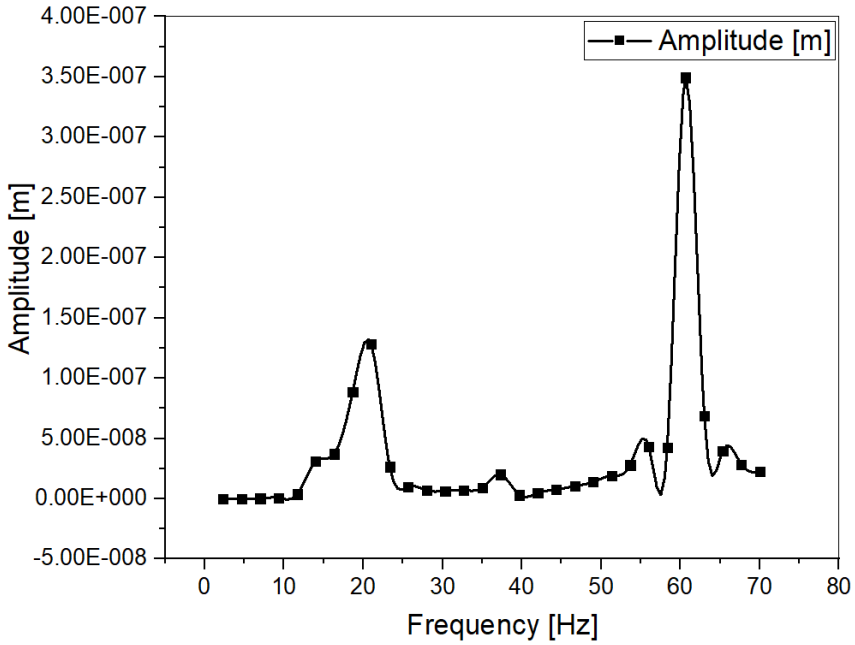

Figure IV.11: Frequency response on Z

We can conclude from the results obtained from the numerical simulation that the maximum amplitude of deformation in the X-axis direction is estimated at 9.6346 e-005m and was obtained near the frequency of 18.667 Hz (see Figure IV.9), and this value is close to the natural frequencies of Mode 3; in the Y-axis direction, the maximum amplitude of deformation is 1.1213 e-004m and is at a frequency of 14 Hz (see Figure IV.10), which is a value close to the natural frequency of the first mode; either in the direction of the Z-axis, the maximum deformation amplitude was 3.4939 e-007 m, as shown in Figure IV.11.

IV.7.2.2 Phase angle effect on deformation

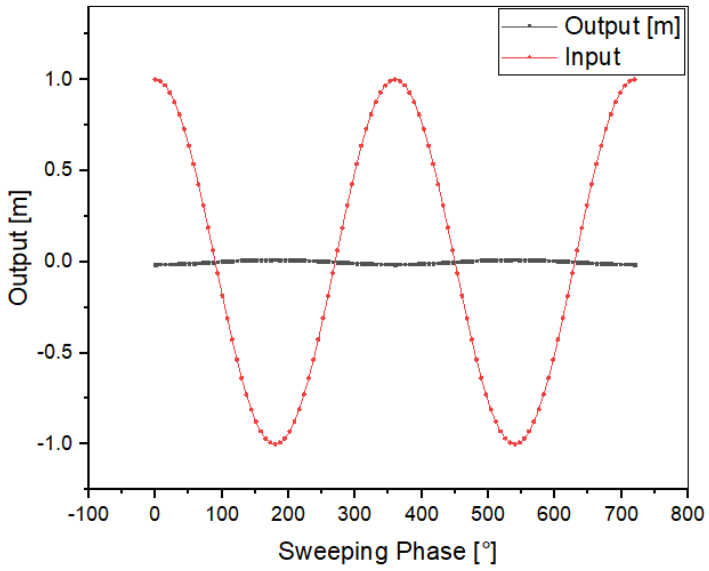

Figure IV.12: Phase angle effect on X

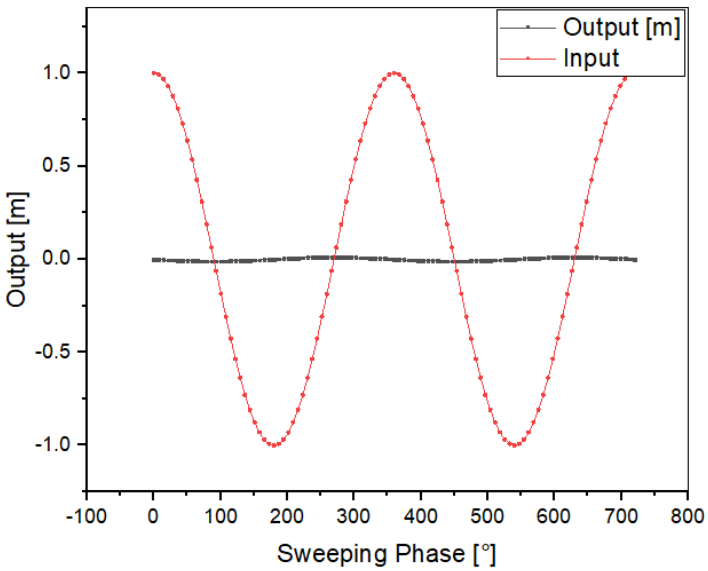

Figure IV.13: Phase angle effect on Y

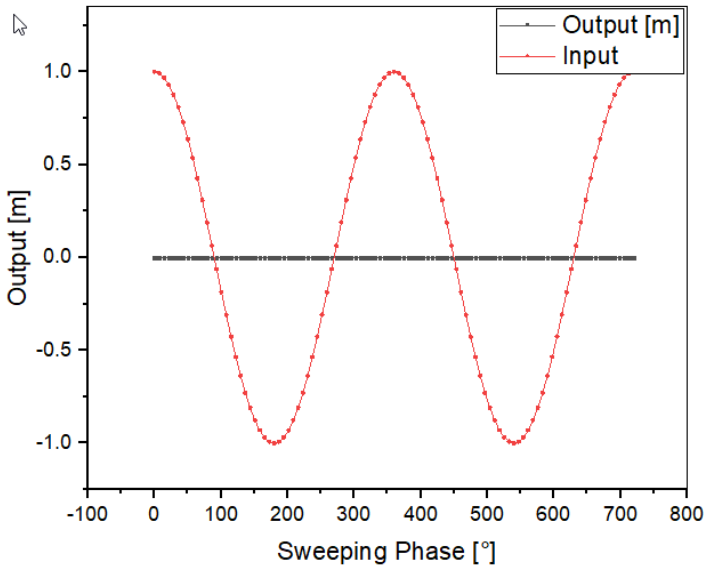

Figure IV.14: Phase angle effect on Z

Figures IV.12, IV.13, and IV.14 show the maximum values of the maximum phase angle in the three directions, respectively: in the direction of the X-axis, it reached -179.78° at a frequency of 45.71 Hz, in the other direction, its maximum value reached about 90.25° at a frequency of 45.71 Hz, and finally, in the direction of the Z-axis, at a frequency of 45.71 Hz, the phase angle reached a maximum value of 129.02.

IV.8 Analysis of the fan in the presence of corroded blades

The FN280 centrifugal fan operates under difficult operating conditions due to the nature of the work it performs in the movement of hot gases, which in turn contain limited cement

dust, and as a result, corrosion of the blades of the fan impeller is produced over time, as figure IV.15 shows images of blade corrosion in fact. To make a numerical simulation and do modal analysis and analysis of the harmonic response of the fan in case the blade is worn out as a result of wear, we tried to design the worn blades to resemble their shape in reality after wear, and due to the fact that the shape of the wear in the blades was random and of different sizes, the SOLIDWORKS program was used for easy handling, and the component parts of the fan were assembled as shown in Figure IV.16.

Figure IV.15: Photos showing worn blades as a result of corrosion

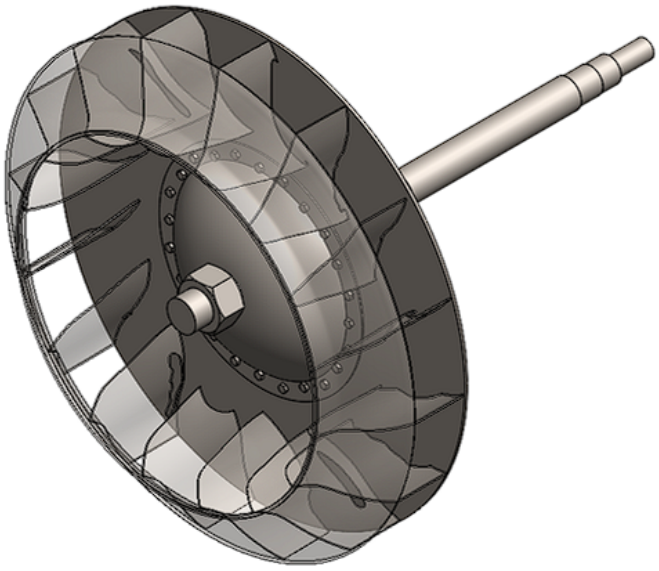

Figure IV.16: 3D model of the fn280 fan with corroded blades

IV.8.1 Meshing the fan in the presence of corroded blades

The meshing of the fan in the presence of worn blades was carried out in the same way and with the same settings, where the SOLID185 element was used to model the fan, which allows simulating deformations of almost incompressible elastic materials. In this case, problems were encountered with the difficulty of mesh worn blades. Contact surfaces were also created first at the sites of the parts connected individually by the conta174 element and the TARGE170 element, and for bearings, the COMBI214 element was used.

Figure IV.17 the fan entanglement in the case of worn blades, where 531,210 elements and 238,299 nodes were created due to the change in The shape of the blade, the number of elements, and the number of nodes created differed.

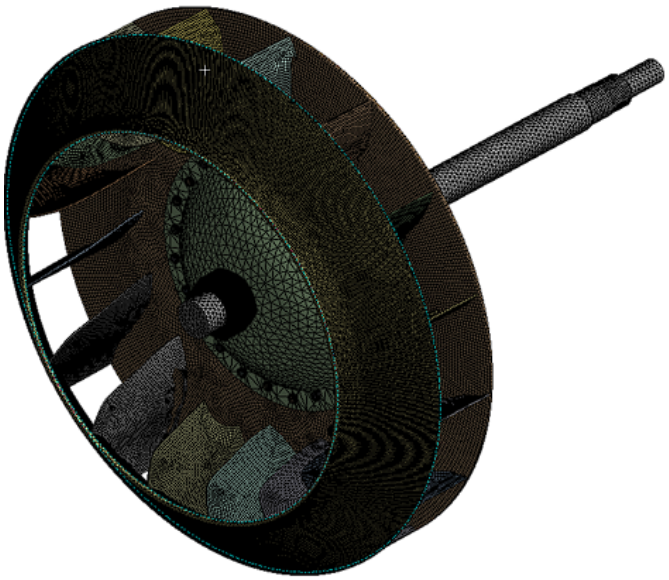

Figure IV.17: A full picture of the rotor mesh in the presence of corroded blades

IV.8.2 Results

IV.8.2.1 Modal Analysis

The modal analysis was carried out under the same boundary conditions that were applied earlier at three different speeds: 100 rpm, 600 rpm, and 1200 rpm. The same number of vibration modes was also used, and the natural frequencies shown in Table IV.5 were obtained, which show the values of natural frequencies in different modes and rotational speeds of the fan with worn blades. It was noted that the frequency values The fourth mode had a large frequency value at a rotation speed of 1200 rpm relative to the same mode at other speeds in addition to natural frequencies. The Campbell diagram and the position forms of the rotor were also extracted.

IV.8.2.1.1 Campbell diagram The Campbell diagram shown in Figure IV.18, which shows the evolution of the natural frequencies of the fan in the case of the presence of worn blades, was extracted for the fan rotor speeds, and using the diagram, the critical speeds and the stability threshold were extracted.

In this case, it is noted that there are only two critical speeds: the first is 806.88 rpm at a natural frequency of 13.478 and the second is 1065.9 rpm at a natural frequency of about 10.87. It is also noted that the rotor is in a stable state, as shown in Table IV.6.

IV.8.2.1.2 Mode shapes Figures IV.19, IV.20, and IV.21 show the modes shapes (rotor vibration modes) obtained from the modal analysis at various speeds of 100 rpm, 600 rpm, and 1200 rpm, respectively.

Table IV.5: Natural frequencies

Mode number	Rotation speed [RPM]	Natural frequency [Hz]
1	100	13.501
2		18.155
3		30.945
4		33.399
1	600	13.478
2		18.071
3		26.252
4		39.62
1	1200	13.39
2		17.677
3		22.077
4		48.477

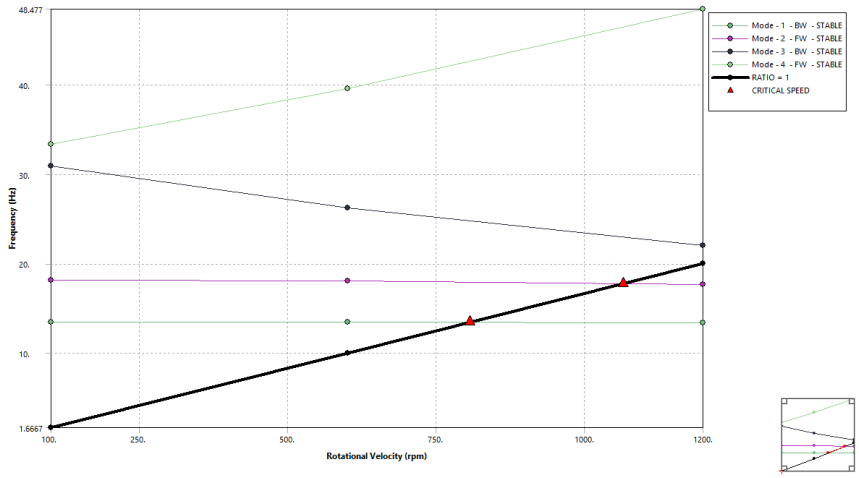

Figure IV.18: Campbell diagram

Table IV.6: Critical speeds and mode stability

Mode	Whirl Direction	Mode Stability	Critical Speed	100. rpm	600. rpm	1200. rpm
1	BW	STABLE	806.88 rpm	13.501 Hz	13.478 Hz	13.39 Hz
2	FW	STABLE	1065.9 rpm	18.155 Hz	18.071 Hz	18.677 Hz
3	BW	STABLE	NONE rpm	30.945 Hz	26.252 Hz	22.077 Hz
4	FW	STABLE	NONE	30.399 Hz	36.62 Hz	45.477 Hz

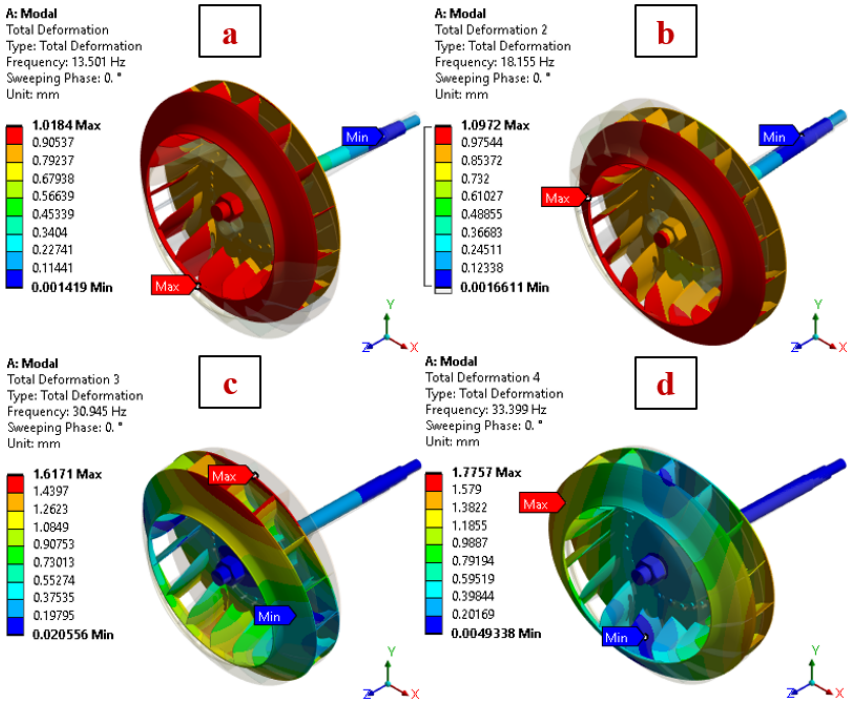

Figure IV.19: Mode shapes at a rotation speed of 100 rpm: a) Mode 1, b) Mode 2, c) Mode 3, d) Mode 4

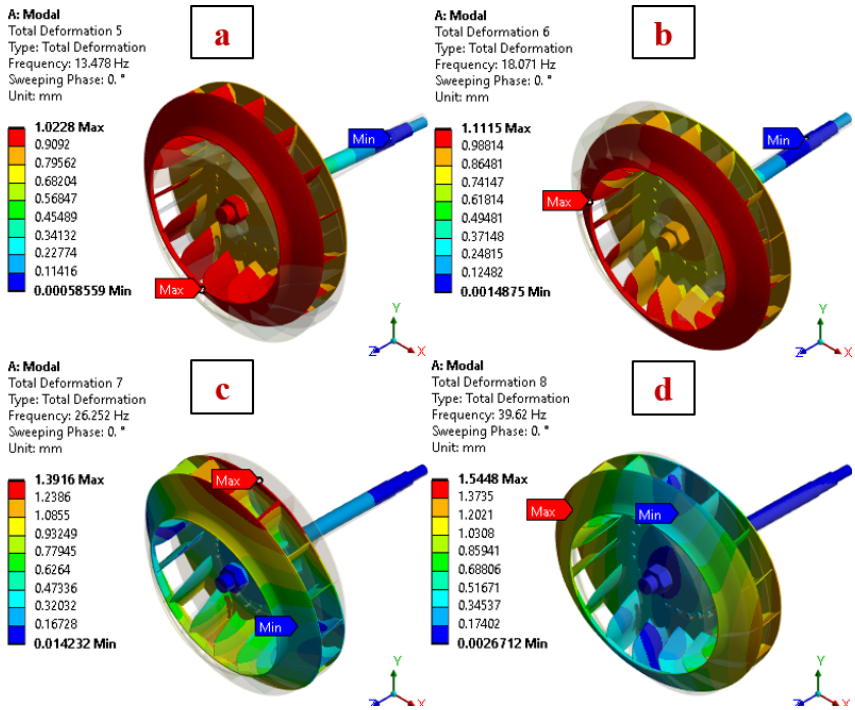

Figure IV.20: Mode shapes at a rotation speed of 600 rpm: a) Mode 1, b) Mode 2, c) Mode 3, d) Mode 4

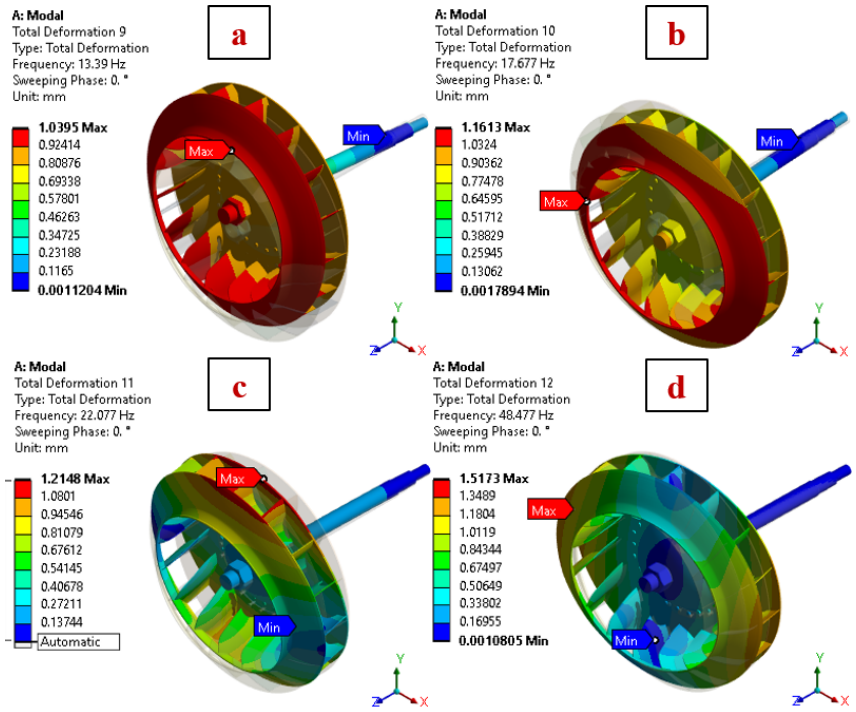

Figure IV.21: Mode shapes at a rotation speed of 1200 rpm: a) Mode 1, b) Mode 2, c) Mode 3, d) Mode 4

Regarding the vibration mode obtained from the results, it was observed that the maximum deformation remains constant at all different rotation speeds. The maximum deformation occurs at a rotation speed of 100 rpm, with a value ranging from 1.0184–1.7757 mm from the first to the fourth mode.

As for the rotation speed of 600 rpm per minute, the maximum value of deformation is from 1.0228–1.5448 mm from the first to the fourth mode, and the third rotation speed of about 1200 revolutions per minute is from 1.0395–1.5173 mm from the fourth mode. The results show us that the maximum deformation value in different vibration modes and different speeds is very small compared to the size of the rotor

IV.8.2.2 Harmonic analysis

IV.8.2.2.1 Frequency response Figures IV.22, IV.23, and IV.24 show the results of the deformation amplitude resulting from the simulation of harmonic response analysis in the X-axis, Y-axis, and Z-axis directions.

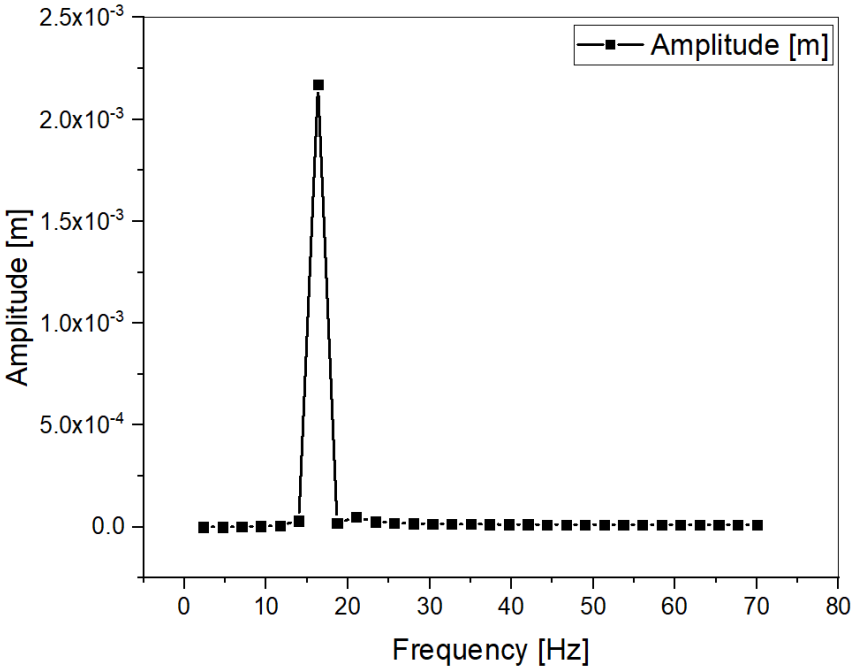

Figure IV.22: Frequency response on X

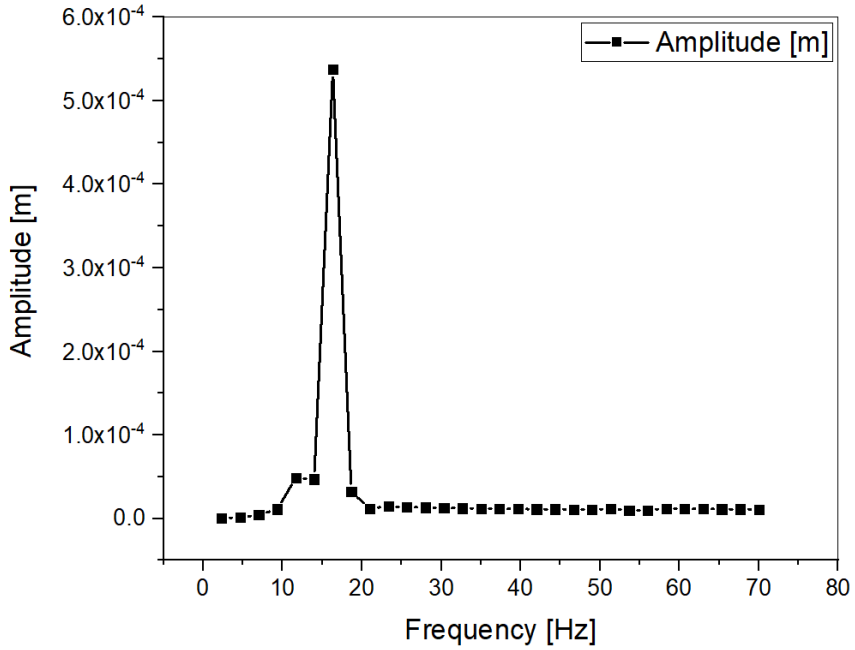

Figure IV.23: Frequency response on Y

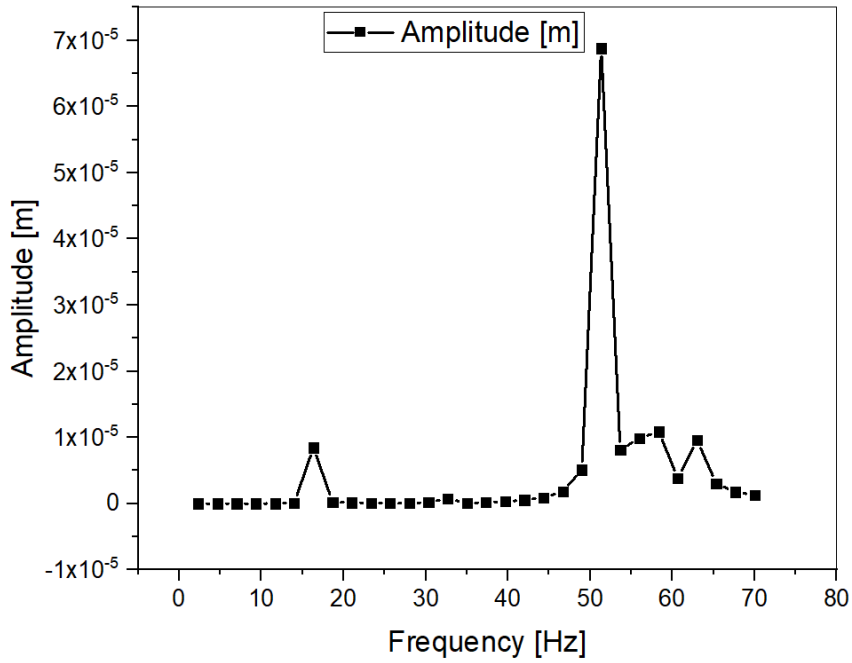

Figure IV.24: Frequency response on Z

We can conclude from the results obtained from the numerical simulation that the maximum amplitude of deformation in the X-axis direction is estimated at 2.1737e–003 m and was obtained near the frequency of 16.33 Hz (see Figure IV.22), and this value is close to the natural frequencies of Mode 2; in the Y-axis direction, the maximum amplitude of deformation is 5.3828e–004 m and is at a frequency of 44.33 Hz (see Figure IV.23), which is a value close to the natural frequency of the 4 mode; either in the direction of the Z-axis, the maximum deformation amplitude was 6.8784e–005 m, as shown in Figure IV.24, and it appears near the frequency 51.33 Hz and is close to natural frequencies of order 4.

IV.8.2.2.2 Phase angle effect on deformation Figures IV.25, IV.26, and IV.27 show the maximum values of the maximum phase angle in the three directions, respectively: in the direction of the X-axis, it reached 179.57° at a frequency of 49 Hz; in the other direction, its maximum value reached about 89.82° at a frequency of 49 Hz; and finally, in the direction of the Z-axis, at a frequency of 40.241° Hz, the phase angle reached a maximum value of 49.

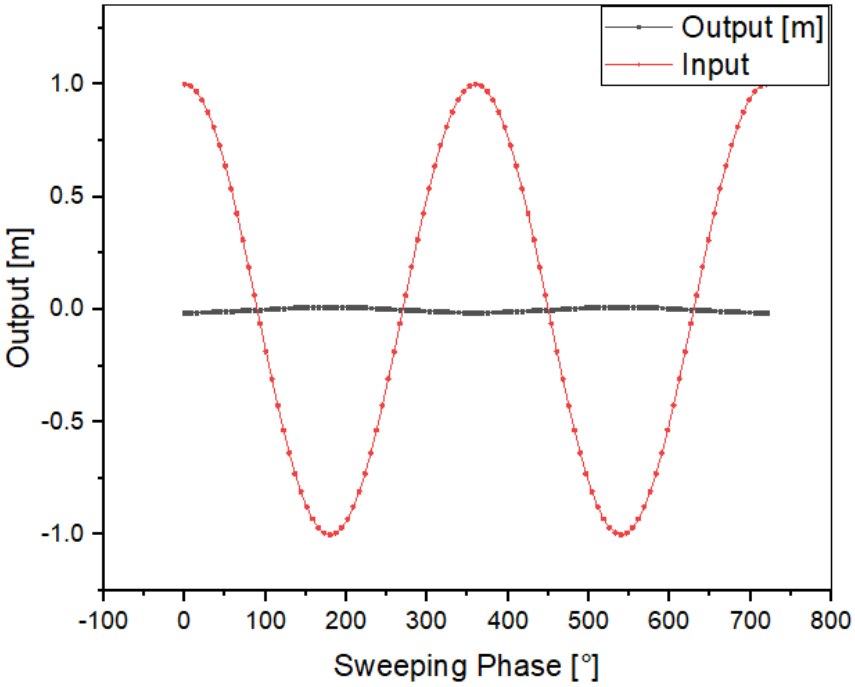

Figure IV.25: Phase angle effect on X

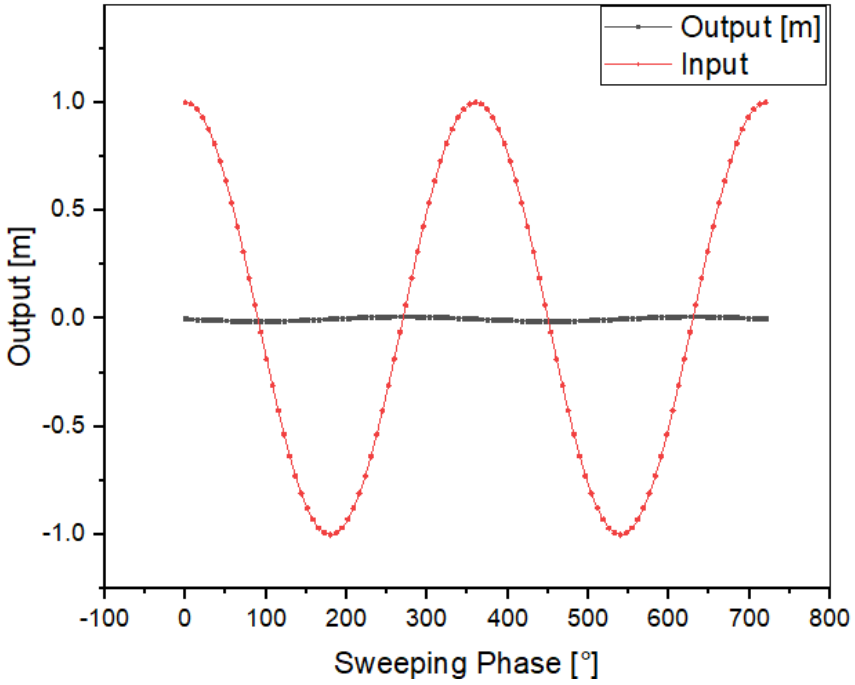

Figure IV.26: Phase angle effect on Y

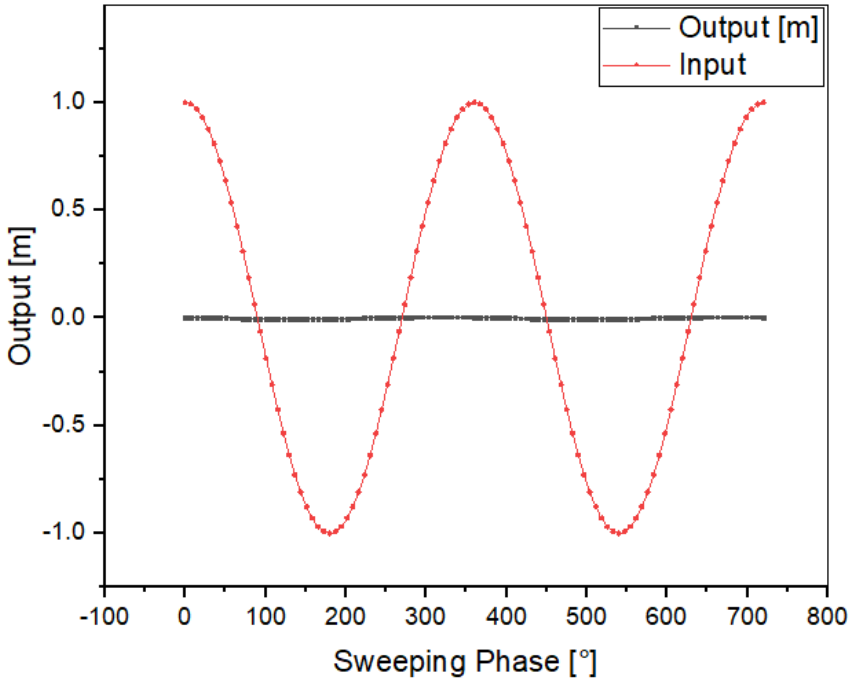

Figure IV.27: Phase angle effect on Z

IV.9 Conclusion

A numerical simulation of the dynamic behavior of a rotary system represented by a centrifugal fan of the FN280 type installed in a cement plant was carried out, where we performed modal analysis and harmonic response analysis in two cases, the case of the fan when there are worn impeller blades as a result of wear and in the case of the fan in the presence of intact blades, the simulation was performed at three different speeds 100 rpm 600 rpm 1200 rpm and it was considered that four main modes at each sufficient rotational speed vibration and extraction of the Campbell diagram to calculate the critical velocities in each case in addition to calculating the nature frequencies and comparative results were drawn The following are the following:

- The simulation results showed that the natural frequencies and maximum distortions are greater in the case of the fan when the blade is worn.
- Having extracted the Campbell diagram, three critical speeds were found, which occurred in the operating range in the case when the blade is intact, but in the case when the blade is worn out, we got only two critical speeds due to unbalance.
- The results of the analysis of the harmonic response showed that due to the unbalanced force applied to the disk, the vibration amplitude was very high and it was noted that the values of the maximum amplitude of deformation are different in each case and in all directions

CHAPTER V

Fluid-structure interaction and fatigue life of a FN280 fan

Contents

V.1 Introduction

The vibration of the rotor system is related to the operation stability and safety of centrifugal fans and is mostly due to the complex flow interaction and large structural load. Centrifugal fans are used in many industrial fields and a variety of rotating machines (industrial fans) can often withstand a very large number of load cycles with little or no maintenance.

When designing rotating machines, structural vibrations must be taken into account because they can cause failure due to dynamic instability or fatigue. Fatigue is an area under research and development in the field of rotating machines. It is common for rotating machines, such as fans and turbines, to be subjected to fluid flow. The passage of this flow through the rotating machines creates pressure fluctuations, which in turn lead to varying loads over time [110, 111]. In this chapter, we study the possibility of estimating the fatigue limit of the centrifugal fan studied in this work, FN280, based on the fluid-structure interaction using the Ansys Workbench program.

V.2 FSI Method

FSI simulation is a category of Multi-physics where fluid dynamics and structural mechanics are the coupled systems involved, and the coupling process is represented by interactions between circumferential flow or internal flow and moving or deformable structures. Both the physical fields and the governing equations, as well as the boundary conditions, must be satisfied simultaneously, and the simultaneous presence of structures and fluids leads to interaction surfaces between the two at these surfaces.

The procedures used to solve FSI problems numerically are divided into homogeneous methods, partitioned methods, and homogeneous methods. Fluid and solid equations are solved using a single algorithm (one homogeneous matrix), while partitioned methods are the opposite of homogeneous methods. The equations of different fields are solved separately and in sequential order, with coupling achieved. Through repetition. In this project, the split approach was performed, which in turn is divided into one-way coupling and two-way coupling.

In the one-way coupling FSI simulation used in this study, the fluid field is solved separately without taking structural deformation into account, which means that we can solve the CFD independently until we reach convergence. After that, the structural analysis is performed by transferring the data, which are the pressure loads, from the CFD. to the structural field. The schematic diagram of the one-way coupling method is shown in figure V.1.

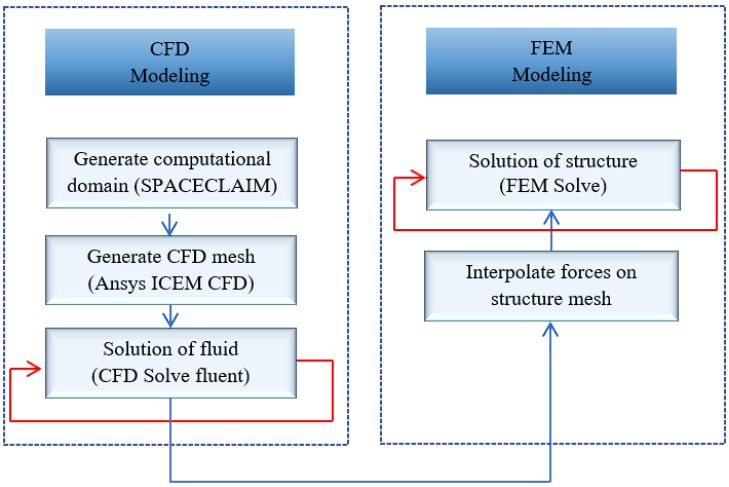

Figure V.1: The schematic diagram of the one-way coupling

V.3 CFD analysis

V.3.1 Mathematical model formulation

Fluid dynamics is a branch of physics that relies on three fundamental principles: conservation of energy, conservation of mass, and momentum conservation. The mathematical expression of mass preservation is defined as follows [111]:

$$\frac{\partial \rho}{\partial t} + \nabla . (\rho \vec{v}) = S_m \tag{V.1}$$

Equation V.1 is the general form of the mass conservation equation, and it is applicable to both compressible and incompressible fluid flows. In this equation, t represents time, ρ represents fluid density, and $\vec{v}$ represents velocity. Additionally, S_m denotes the mass that is introduced into the continuous phase of the secondary dispersed phase, as well as any user-defined sources [112].

The energy conservation equation is written in the following form:

$$\frac{\partial}{\partial t} (\rho \vec{v}) + \nabla . (\rho \vec{v} \vec{v}) = -\nabla p + \nabla . (\overline{\overline{\tau}}) + \rho \overrightarrow{g} + \overrightarrow{F} \tag{V.2}$$

p is static pressure, $\overline{\overline{\tau}}$ is a stress tensor, and $\rho \overrightarrow{g}$ is gravitational body force, and $\overrightarrow{F}$ is external body forces; it also contains other model dependent source terms such as porous media and user defined sources.

The stress tensor $\overline{\overline{\tau}}$ is given by [113] :

$$\overline{\overline{\tau}} = \mu \left[\left(\nabla \overrightarrow{v} + \nabla \overrightarrow{v}^T \right) - \frac{2}{3} \nabla . \overrightarrow{v} I \right] \tag{V.3}$$

μ is the molecular viscosity, I is the unit tensor, and the second term on the right-hand side is the effect of volume expansion.

To simulate the turbulent flow, the turbulent $k - \omega$ SST model was used since it is computationally less expensive and provides relatively good results compared to other

models. The $k-\omega$ SST model is a two component, hybrid viscosity model that combines the $k-\omega$ and $k-\epsilon$ models. It combines the prediction of the free flow of the $k-\epsilon$ model with the good behavior of the $k-\omega$ model. In the very region, the kinetic energy is given perturbation k and the perturbation-specific dissipation rate ω by transfer equations [114]:

$$\frac{\partial(\rho k)}{\partial t} + \nabla(\rho U k) = \nabla(\Gamma_k \nabla k) + \widetilde{P}_k - D_k \tag{V.4}$$

$$\frac{\partial(\rho \omega)}{\partial t} + \nabla(\rho U \omega) = \nabla.(\Gamma_\omega \nabla k) + P_\omega - D_\omega + Y_\omega \tag{V.5}$$

Where Γ_k and Γ_ω is the effective diffusivity of the k turbulent energy, and ω represent the specific dissipation rate, $\widetilde{P}_k$ and P are the turbulence production terms, D_k and D_ω the terms represent the dissipation of the disorder.

V.3.2 Computational domain of the Fan

Due to the application of the one-way coupling FSI method in this study, therefore, the fluid field must be solved independently until we reach convergence. Thus, it is necessary to create a computational field that includes the inlet and outlet pipes and the impeller. The SPACECLAIM software was used to extract the fluid field and model the flow parts. A straight section was added at the top of the inlet. In order to eliminate the interference of the physical model in the numerical calculation and allow the development of a larger length of the flow, its length was extended to twice the diameter of the inlet, and to prevent backflow at the outlet, the outlet was extended to four times the diameter of the outlet. Figure V.2 shows the complete computational scope of the fan.

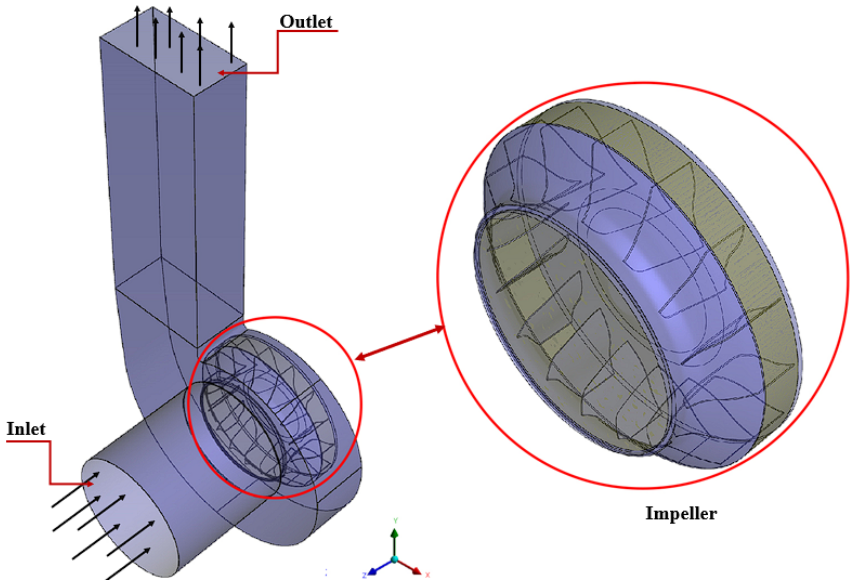

Figure V.2: Computational domain for the fan

V.3.3 Meshing procedure

The meshing was created in the field of fluids using the ICEM CFD ANSYS program. To enable the rotation of the fan, the fluid field was divided into different areas, and

due to the complexity of the computational field and the large curvature of the impeller, Blade, an irregular tetrahedral grid was used in areas with complex geometry, that is, not all areas in the computational field, and the areas of the various parts of the centrifugal fan (blade surface, casing neck, and blade passage inside the impeller) are of the same importance in numerical simulation, so the density of the grid focuses on these areas with a smooth transition from low to high grid density, and to allow the flow to pass during the stable of the boundaries of different cells of the rotating and stationary sphere interfaces were used. The mismatched network. Figure V.3 shows a view of the entire computational domain mesh.

Figure V.3: View of the entire computational domain mesh

The sawn layer elements are created around the blade surfaces in order to meet the mesh accuracy requirements for the SST k- model. The distance of the first sawn layer to the wall area has been adjusted after conducting several simulations. This mesh setup ensures that the value Y+ distance between the wall and the first layer in the mesh is within the specified range, which is Y>=1+ for the SST turbulence model, and the minimum number of sawn layers, which is 12 normal sawn layers on the wall of each boundary layer. Figure V.4 shows a cross-section of the impeller mesh as well as the exact mesh in the area near the wall for the blade surface for numerical simulations and published classes. The value of +Y is also observed on the high- and low-pressure surfaces of the blade along the simulation process [115].

To ensure the mesh's accuracy, the necessary number of cells was determined by considering the direction of the power column (Wshaft) as an indicator for an independent grid solution. This was done in a steady-state simulation, focusing on a fixed blade step position and the design flow rate (Qd). Table V.1 shows the results obtained numerically for the network. Through the table, we note that when the number of nodes is greater than 5.57 million, the numerical results become unaffected by network optimization, so we used 5574675 nodes to reduce the computational burden.

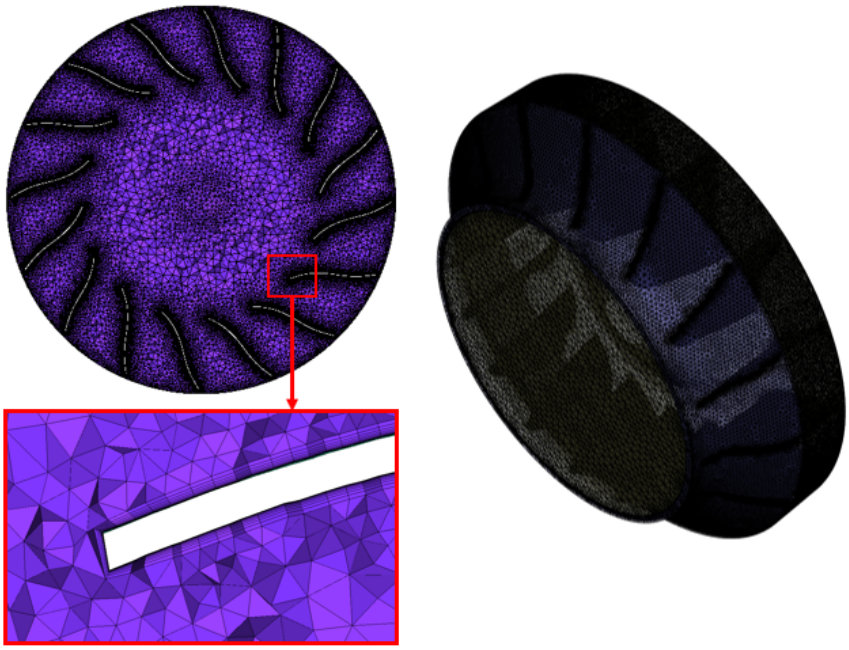

Figure V.4: View of the entire computational domain mesh

Table V.1: mesh density relative to W_shaft

number of nodes (Million)	4.3	5.1	5.57	5.58	5.98
W_shaft , [kw]	495.3	492.1	488.4	488.1	487.9

V.4 Structural calculation

V.4.1 FEM Meshing

As for the solid domain, since the centrifugal fan is influenced by the structural load applied to it, resulting from the pressure contours in fluid dynamics analysis, a suitable geometric mesh was developed using unstructured tetrahedral solid elements. Due to the fan's complex design, the SOLID185 element was employed, which comprises three-dimensional elements defined by 8 degrees of freedom at each node in addition to the connecting elements [109]. This was achieved using the ANSYS MESHING program, and the total number of elements in the mesh is more than 0.53 million, as shown in V.5.

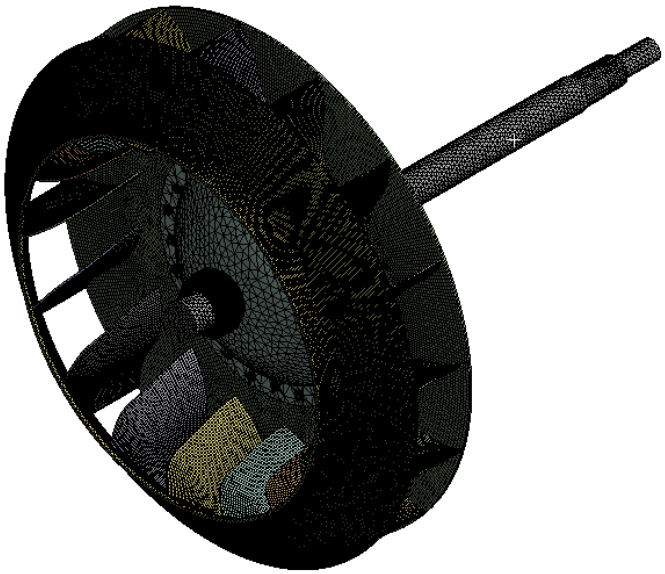

Figure V.5: Meshes for structure

V.4.2 Boundary condition FEA

In the analysis of the transient structure, the rotor shaft (centrifugal fan) was constrained and loaded. The loads of the fan system include the external and internal pressure of the fluid on the fan and the centrifugal force generated by the rotation of the fan. The centrifugal force determines the speed of the rotating subsystem; the operating speed value of the fan is 985 rpm, and its direction is consistent with the direction of rotation of the fan. The flow field pressure is obtained by loading the flow domain calculation results and transferring them to the fan structure via the solid-liquid coupling interface. The cylindrical support of the propeller shaft bearings has been simplified, and the cylindrical support of the shaft bearings has been added for axial and diagonal restraints. Figure V.6 shows boundary annotations to simulate transient structural analysis.

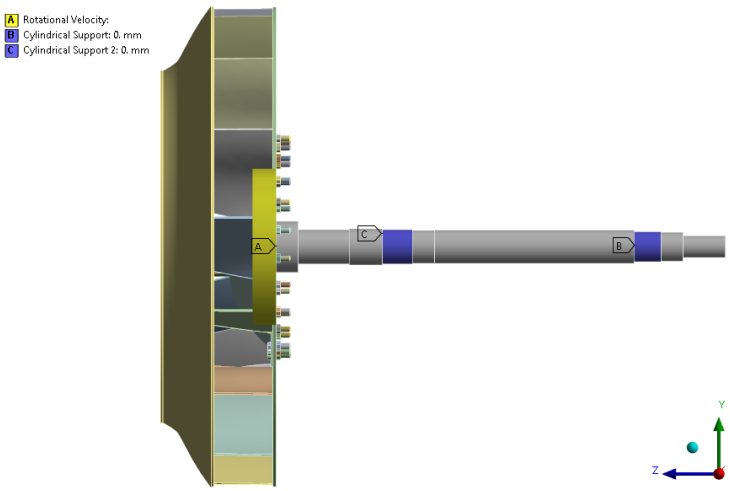

Figure V.6: Boundary conditions applied to the fan

V.5 Results and discussion

V.5.1 CFD

To better understand the flow and structural behavior of the centrifugal fan, three cross sections Z1, Z2, and Z3 were created on the rotation axis at different areas of the impeller, where Z1 = 0.04m, Z2 = 0.14 m, and Z3 = 0.24 m, as shown in Figure V.7, in order to show the static pressure contours and flow velocity in different areas of the impeller and the casing area, according to the design flow rate, and the results were shown using the CFD POST program.

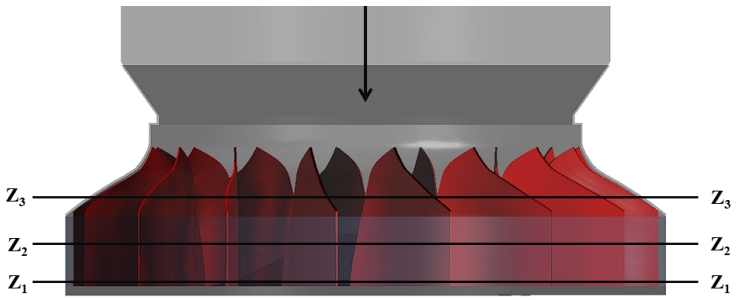

Figure V.7: Cross sections Z1, Z2, and Z3

Figures V.8, V.9, and V.10 show the contours of pressure at the level of the cross sections Z1, Z2, and Z3, respectively. The figure depicts that the pressure has almost the same distribution in Z1 and Z2, and the difference is in the maximum and minimum values, as it appears from the figure that the pressure increases as the impeller enters the outlet, and the pressure value is at its maximum at the neck of the casing. When the impeller rotates, this results in the conversion of dynamic pressure into static pressure along the length of the housing, with a high-pressure gradient in the radial direction.

As for the distribution of pressure on the cross-section Z3, it is slightly different, especially at the tip of the housing flap, where it is at the lowest value due to its location, which is at the top of the impeller blade, and the pressure is lower than that when compared to Z1 and Z2.

As for the blade passages (from blade to blade) of the impeller, the pressure on the suction side is lower than on the pressure side of the blade, as at the tip of the front edge of the blade, the pressure is at its lowest value. It can also be noted that when the blade passes in front of the cover tongue, the pressure is higher, and when the blade rotates, from the neck of the casing to the large discharge section of the helix, the pressure decreases. This is due to the asymmetric helix geometric design, which in turn leads to the pressure being distributed on the blades in an irregular state.

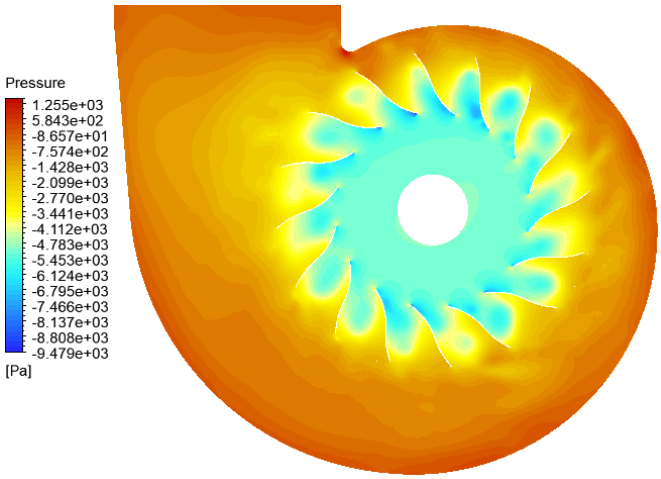

Figure V.8: Pressure contours on cross section Z1

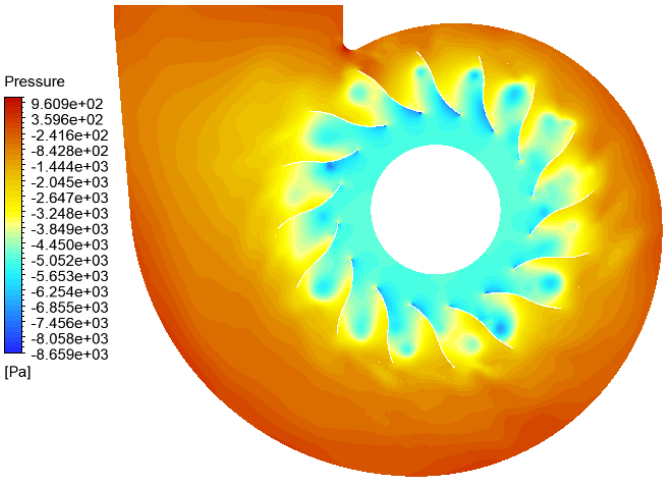

Figure V.9: Pressure contours on cross section Z2

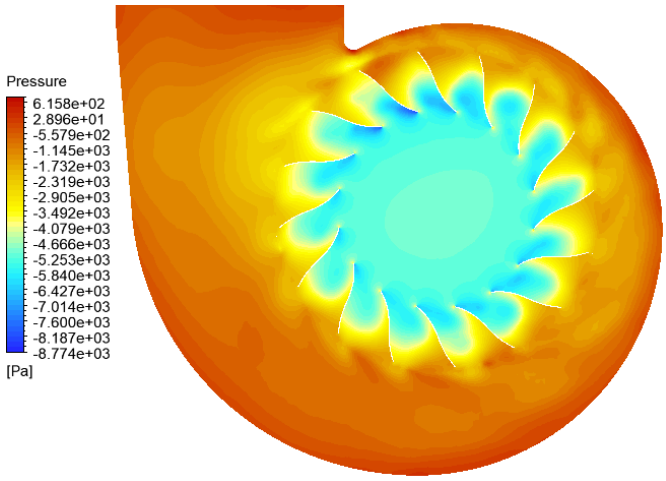

Figure V.10: Pressure contours on cross section Z3

Figures V.11, V.12, and V.13 show the velocity contours across three different segments, Z1, Z2, and Z3, respectively, and the field of the impeller shell with the design

flow. According to the velocity contours figures, there appear to be differences in the distribution and values of the flow velocity in the three sections, where the lowest velocity values are found in the cap tongue in Z1 and Z2, while in Z3, in the same area, there are high flow velocity values. This is due to the large curvature of the blade, and there are also high flow velocity values with different values for each sector at the leading edges, also near the pressure side of the blade, and also at the impeller outlet. The velocity distribution also indicates that there are interruptions in most of the passages between the blades (from blade to blade), which are immediately after the leading edge of the blade. Therefore, during the design stage, the shape of the blade entry angle should be taken into account due to its significant influence on the flow in the passages between the blades and at the impeller inlet. The area of the cap tongue is a resting point and is also associated with the separation of the flow present in all passages and in the three sectors, which is caused by the inappropriate blade entry angle and high bending of the blade, which causes the incoming flow not to be directed around the impeller blade.

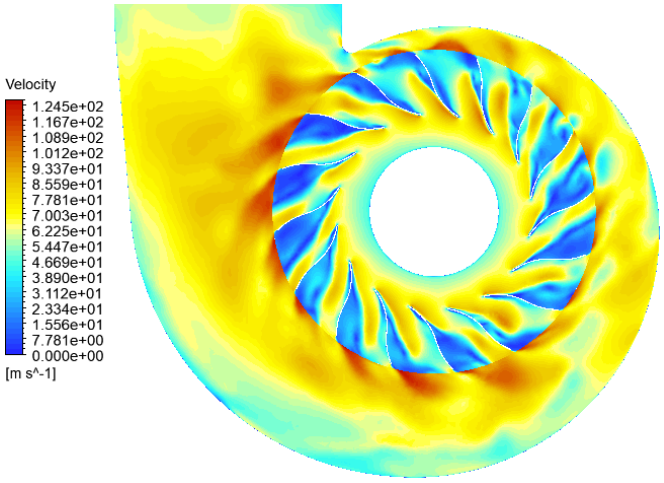

Figure V.11: Velocity contours on cross section Z1

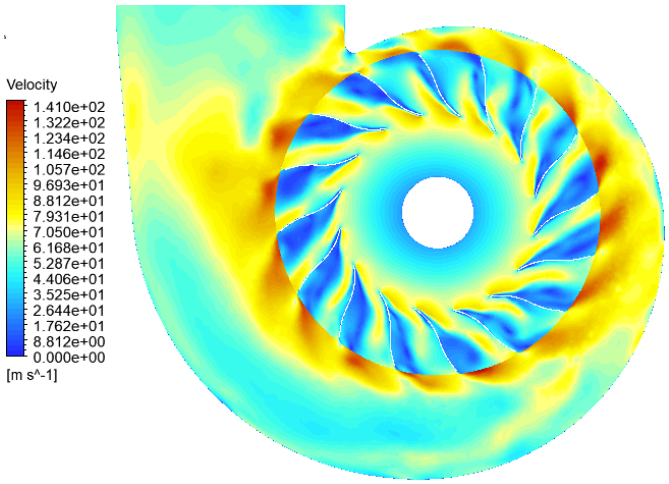

Figure V.12: Velocity contours on cross section Z2

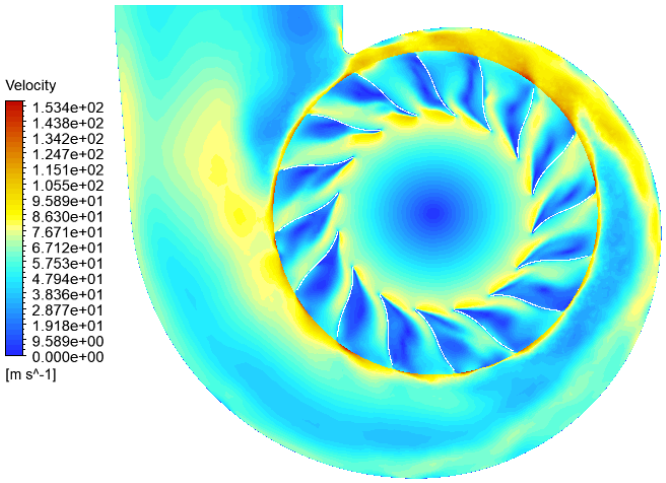

Figure V.13: Velocity contours on cross section Z3

V.5.2 Results Finite elements method

FSI simulations, using a one-way coupling approach, provide valuable and detailed insights into the structural response of various components of a centrifugal fan to aerodynamic loads generated during the analysis of a transient computational fluid dynamics simulation. This is achieved by submitting results from the independent FEM. The results of the transient structural analysis are presented, including the displacement domain and the results of the stress domain analysis. In addition, transient structural analysis provides a fatigue limit estimate, which helps in assessing whether fluid pressure should be included in the fatigue limit estimate.

Figure V.14 shows the overall deformation features of the rotor system. It appears from the figure that the maximum deflection is at the leading edge of the impeller blades, with the largest deformation value of 5.008 mm. The deformations were evaluated to be very small compared to the dimensions of the fan. Figure V.15 shows the time history of the maximum total deformation, which shows a decrease in the maximum value of deformation due to the stability of the rotating system.

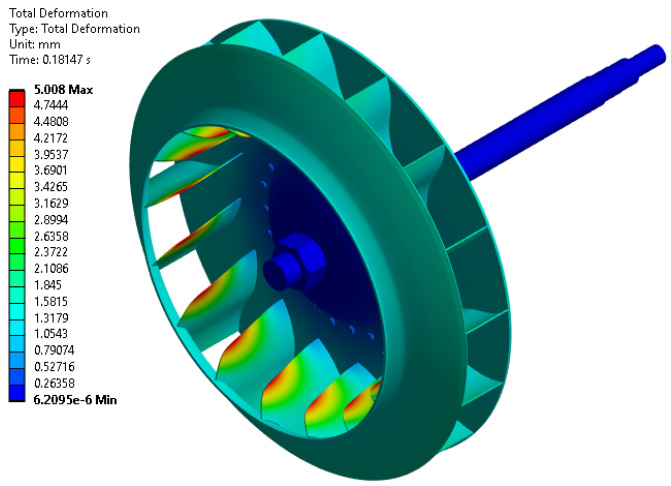

Figure V.14: Contour of the total deformation of the rotor

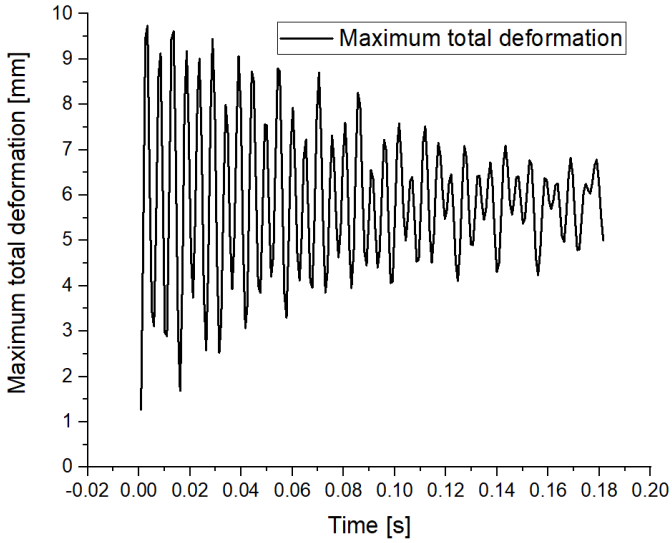

Figure V.15: Time history of maximum total deformation

Figure V.16 shows the navigator of the stress load based on the equivalent von-Mises stress of the rotor, which is part of the maximum stress failure theory. Through the pressure distribution, we can see that the region with the highest stress is located near the contact zone between the blades and the front and rear panels. The maximum stress value reaches 866.94 MPa and is This value varies with time, as shown in figure V.17.

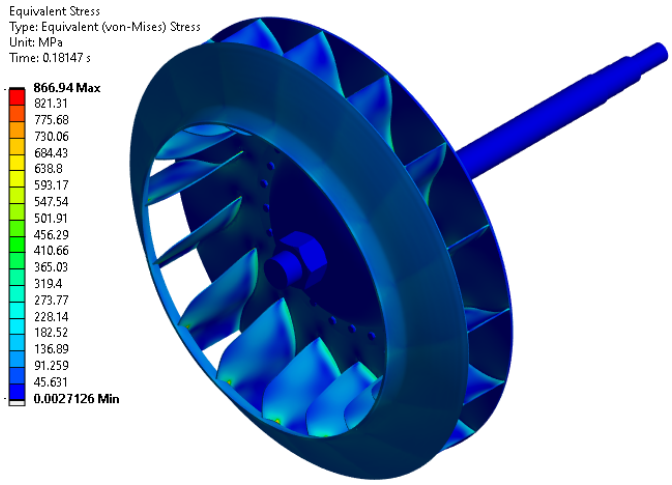

Figure V.16: Contour of the equivalent von Mises stress of the rotor

Fatigue is considered a weakening of the material that results from repeated application of loads, and it can also be considered crack growth since when a load is applied each time, the cracks grow slightly. Average stress and alternating stress are parameters that have a significant impact on the fatigue life of the fan, as fatigue strength increases with a decrease in alternating stress and/or average stress, and fatigue strength decreases with an increase in one or both of them. To verify the fatigue behavior for the current study, a lifetime fatigue model was used to conduct fatigue analysis. The model does not differentiate between crack initiation and propagation, and the fatigue life determines the total life of the joint and is based on the S-N curve of the material, which is often established from experimental tests. The fatigue life model also deals with high cycle

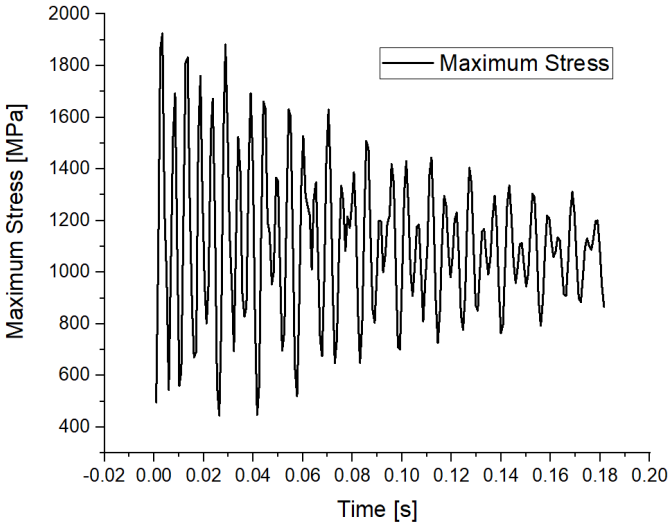

Figure V.17: Time history of maximum equivalent von Mises stress

stress, and the stress ratio $R = \sigma_m in/\sigma_m ax$ is used.

In ANSYS, the fatigue and stress model for the fatigue unit allows the inclusion of average stress effects through direct interpolation between the experimental S-N data. Due to the unavailability of this experimental data, experimental relationships can be used that work to use the experimental relationships for the properties of static materials with the S-N data, which enables us to calculate the average stress effects. The Gerber equation was used because the fan used in the current study is made of iron. It was also used in the fatigue analysis as a stress element to convert the multi-axial stress obtained from the FEA to the uniaxial stress state for the experimental fatigue data, which is the equivalent stress (von-mises).

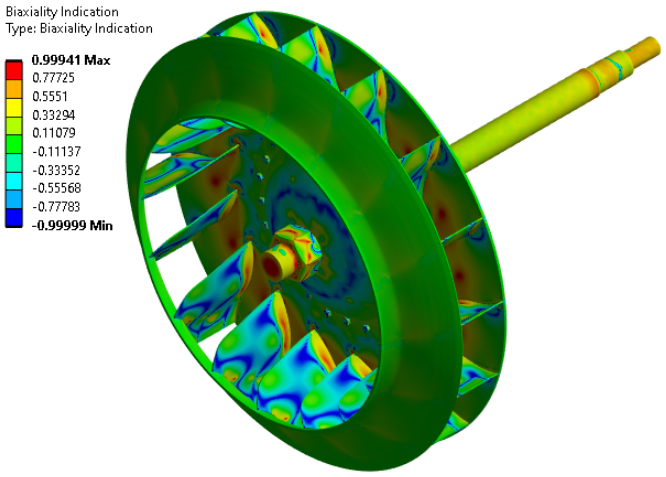

Figure V.18: Biaxiality indication for the rotor

Figure V.18 shows a biaxial indicator diagram for a centrifugal fan. It is defined as the smallest main pressure divided by the largest, ignoring the one closest to zero. It shows that the green color is at the majority of the fan, which corresponds to a biaxial signal (0), which indicates a uniaxial stress state. The color blue with a biaxial signal (-1)

corresponds to pure shear, and red (1) corresponds to the pure biaxial state. Figure V.19 shows the fatigue factor for the safety of the centrifugal fan. This safety factor relates to fatigue failure. We can see from the figure that the maximum factor of safety is 15, and values lower than 1 indicate failure before reaching the design life. The results of the contour plot for fatigue damage were also shown. For the fan shown in figure V.20, which is defined as the design life divided by the available life.

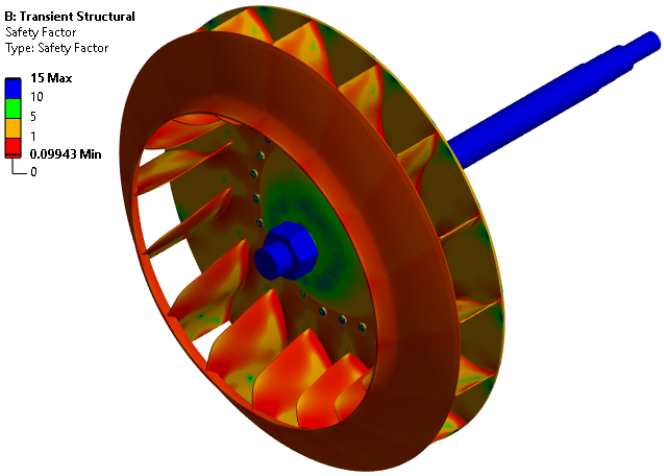

Figure V.19: Fatigue factor of safety for the rotor

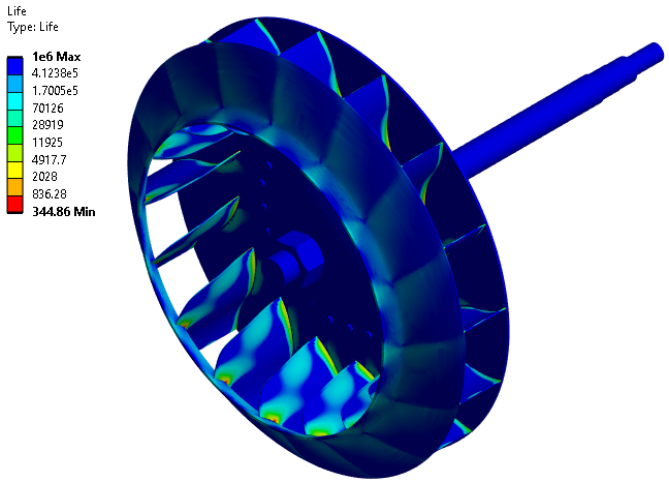

Figure V.20: fatigue damage

V.6 Conclusion

3D FSI simulations were conducted using the ANSYS Workbench platform, employing a one-way interaction approach. Unstable flow simulations were executed with Fluent ANSYS, while the structural domain was analyzed using transient structural ANSYS. The objective of this study is to enhance the capability of performing numerical simulations for fluid-structure interactions in centrifugal fans and to explore the potential improvement in fatigue analysis and the lifespan of the centrifugal fan through these simulations. This is crucial, as the fatigue assessment method typically considers centrifugal loads resulting

solely from the fan's inertia. Therefore, in this study, we consider the possibility of the fan's lifespan being influenced by pressure loads caused by the liquid. The FN280 centrifugal fan installed at the cement plant was selected.

The results of numerical simulations indicate that the compressive loads exerted by the fluid on the fan structure have a minimal effect on the life of the studied fan. Additionally, the structural deformations caused by fluid loads are insignificant, given that the rigidity of the fan, made of iron material, surpasses that of liquid loads. The primary weakness of this study lies in the lack of data to validate the results, which is considered a topic for future work.

General conclusion

This work aims to evaluate the contributions to the analysis of the dynamic and vibration behavior of elastic rotors, and various aspects were addressed. A strategy was presented to better understand the vibrations phenomena to the equations of motion of the rotor by considering the important phenomena that affect the dynamic behavior, including gyroscopic impact, unbalance, and internal damping, which allows us to study the unbalance in a diagnostic test that should take into account the gyroscopic effect, especially in the study of scaling the shafts of rotating machines.

A finite element model has been developed and modeled for real systems due to the fact that it is more accurate and makes it possible to study all rotor vibration modes. In addition, it is modular as it allows adding stiffness and external forces at each node to be studied based on their individual characteristics, where we have identified the different matrices for the dynamic parameters of freedom.

To study the behavior of the rotor dynamics, the dynamic analysis of the centrifugal fan (cement draft fan FN280) was performed using ANSYS WORKBENCH, where all the different parts of the fan were designed by SOLIDWORKS except for the blade because we do not have data about it, so we used reverse engineering technology by extracting the data for the blade (point cloud) by CMM and we created a 3D model of the blade and analyzed the accuracy of the model in comparison between the survey data and the CAD model by calculating deviations by GEOMAGIC CONTROL X.

We carried out a numerical simulation of the dynamic behavior of the fan using modal analysis and this was done at three different rotational speeds and four main modes were considered at each rotational speeds to reduce the time and computational ability, critical speeds were extracted through the Campbell diagram and determine the displacements and vibration modes and a simulation of harmonic response analysis was performed and the results confirmed that the rotor response to the excitation force of unbalance type good results, and the same modal analysis and harmonic response analysis were addressed, but in the case where the fan blades are worn out as a result of corrosion caused by air hot, loaded with cement dust particles. After the work of the simulations, the following conclusions were drawn:

- The simulation results showed that the natural frequencies and maximum deformations are greater in the case when the blade is worn in all modes.
- After we extracted the Campbell diagram, three critical speeds were found, which occurred in the operating range in the case when the blades are intact, and the

value of the maximum critical speed is close to the critical speed provided by the manufacturer with an error of 6.4%, but in the case when the blades are corroded, only two critical speeds were obtained, and the maximum critical speed was less than a the critical speed when the blades were intact, due to the unbalance that limited the result of the corroded.

- In the harmonic analysis, the intensity of the vibrations caused by the unbalanced force was very high; the maximum values of the excitation frequency and the maximum vibration response were different in the two cases.

3D FSI simulations were performed using the ANSYS WORKBENCH platform by using a one-way coupling approach, and the FLUENT ANSYS was used to simulate unstable flow, while the transient structural ANSYS was used to analyze the structural field. The objective of these simulations is to enhance the ability to perform FSI simulations on rotating machines and explore the potential improvement in fatigue analysis and age estimation of rotors. The results of numerical simulations indicate that the pressure loads exerted by the fluid on the blade structure have a minimal effect on the life of the fan. In addition, the results also showed that the structural deformations caused by pressure loads are insignificant due to the rigidity of the fan made of iron, which exceeds the rigidity of pressure loads.

Future work

In future work, I will investigate the influence of bearing type on fan performance, in addition to the impact of varying the number of blades on critical speeds.
Additionally, an will be made to simulate the FSI two-way coupling to study the effect of fluid on the vibrations and stability of the fan.

Bibliography

[1] E. Novillo, *Dynamics of Rotating SDOF Systems*. Springer Science & Business Media, 2005.

[2] M. I. Friswell, J. E. Penny, S. D. Garvey, and A. W. Lees, *Dynamics of rotating machines*, 2010.

[3] A. Batailly and S. Cogan, "Modélisation et étude de la dynamique complexe d ' un système bi-rotor aubagé couplé," 2019.

[4] Siemens AG, "Siemens STC-SV centrifugal compressors with vertically split casing," 2005. [Online]. Available: https://www.yumpu.com/en/document/read/12343389/siemens-stc-sv-centrifugal-compressors-with-vertically-split-casing

[5] M. T. Schobeiri, Meinhard T and Schobeiri, *Gas Turbine Design, Preliminary Considerations*. Springer, 2018.

[6] H. Cao, L. Niu, S. Xi, and X. Chen, "Mechanical model development of rolling bearing-rotor systems: A review," *Mechanical Systems and Signal Processing*, vol. 102, pp. 37–58, 2018. [Online]. Available: https://doi.org/10.1016/j.ymssp.2017.09.023

[7] M. B. Wagner, A. Younan, P. Allaire, and R. Cogill, "Model reduction methods for rotor dynamic analysis: A survey and review," *International Journal of Rotating Machinery*, vol. 2010, 2010.

[8] C. Meher-Homji, "The Historical Evolution of Turbomachinery," *PROCEEDINGS OF THE 29TH TURBOMACHINERY SYMPOSIUM*, pp. 281–322, 2000. [Online]. Available: http://turbo-lab.tamu.edu/proc/turboproc/T29/t29pg281.pdf

[9] A. D. Dimarogonas, "A Brief History of Rotor Dynamics," *Rotordynamics '92*, pp. 1–10, 1992.

[10] W. M. Rankine, "On the centrifugal force of rotating shafts," *an Nostrand's Eclectic Engineering Magazine (1869-1879)*, vol. 1, no. 7, p. 598, 1869.

[11] A. Stodola, *Steam Turbines with an appendix on gas turbines and the future of heat engines*. D. Van Nostrand Company, 1905.

[12] H. Gash, R., Nordmann, R., & Pfützner, *Rotordynamik. 2., vollständing neu bearbeitete und erweiterte Auflage*. Springer, Berlin, 2006.

[13] S. Dunkerley, "VIII. On the whirling and vibration of shafts," *Philosophical Transactions of the Royal Society of London.(A.)*, pp. 279—-360, 1894.

[14] H. H. Jeffcott, "XXVII. The lateral vibration of loaded shafts in the neighbourhood of a whirling speed.—The effect of want of balance," *The London, Edinburgh, and Dublin Philosophical Magazine and Journal of Science*, vol. 37, pp. 304—-314, 1919.

[15] V. J. Loewy, Robert G and Piarulli, "Dynamics of rotating shafts," vol. 4, 1970.

[16] J. M. Vance, F. Y. Zeidan, and B. G. Murphy, *Machinery vibration and rotordynamics*. John Wiley & Sons, 2010.

[17] W. Campbell, "Protection of steam turbine disk wheels from axial vibration," Tech. Rep. 11, 1924.

[18] D. M. Smith, "The motion of a rotor carried by a flexible shaft in flexible bearings," vol. 142, pp. 92—-118, 1933.

[19] B. L. Newkirk and H. D. Taylor, "Shaft whipping due to oil action in journal bearings," *General Electric Review*, vol. 28, no. 8, pp. 559–568, 1925.

[20] S. TIMOSHENKO, *VIBRATION PROBLEMS IN ENGINEERING*, second edi ed., NEW YORK, 1937.

[21] G. Bolotin, Vladimir Vasil evich and Hermann, *Nonconservative Problems of the Theory of Elastic Stability*, 1963. [Online]. Available: www.samizday.ru/reprint

[22] E. Gunter, "Dynamic stability of rotor-bearing systems," *Library*, vol. 113, p. 231, 1966. [Online]. Available: http://www.getcited.org/pub/101249161

[23] C. Hummel, "Kritische Zahlen als Folge der Nachgiebigkeit des Schmiermittels im Lager," *PhD diss., ETH Zurich*, 1926.

[24] H. Holzer, *Die Berechnung der Drehschwingungen und ihre Anwendung im Maschinenbau*, 1921.

[25] O. Reynolds, "IV. On the theory of lubrication and its application to Mr. Beauchamp tower's experiments, including an experimental determination of the viscosity of olive oil," *Philosophical transactions of the Royal Society of London*, vol. 177, pp. 157–234, 1886.

[26] W. Harrison, "The hydrodynamical theory of lubrication with special reference to air as a lubricant," 1913.

[27] D. Robertson, " XII. Whirling of a journal in a sleeve bearing ," *The London, Edinburgh, and Dublin Philosophical Magazine and Journal of Science*, vol. 15, no. 96, pp. 113–130, 1933.

[28] M. Kirk, R Gordon and Simpson, "Full load shop testing of 18,000-hp gas turbine driven centrifugal compressor for offshore platform service: Evaluation of rotor dynamics performance," *NASA. Lewis Research Center Instability in Rotating Machinery*, 1985.

[29] A. Brown, RD and Hart, "A Novel Form of Damper for Turbo-machinery," in *NASA Conf. Publ*, 1986, vol. 2443, pp. 1–23.

[30] H. Wsyssmann, "Theory and measurements of labyrinth seal coefficients for rotor stability of turbocompressors," *NASA. Lewis Research Center Rotordynamic Instability Problems in High-Performance Turbomachinery,*, pp. 237–258, 1987.

[31] E. H. Miller, "Rotor stabilizing labyrinth seals for steam turbines," *General Electric Co,*, no. December 13, 1983.

[32] J. Nan, M. Wang, T. Zan, and J. Zhang, "Vibration characteristics analysis of a high-speed horizontal machining center," *Advanced Materials Research*, vol. 472-475, pp. 849–852, 2012.

[33] M. P. Khan, Mohd Maaz Dr. P Shailesh2 and 1P.G, "ROTOR DYNAMIC ANALYSIS OF DRIVING SHAFT OF DRY SCREW VACUUM PUMP," *International Research Journal of Engineering and Technology (IRJET)*, vol. 06, no. 9, pp. 1965–1979, 2019.

[34] D. S. Khamari, P. S. Kar, S. Jena, J. Kumar, and S. K. Behera, "Rotordynamic Analysis of High-Speed Rotor Used in Cryogenic Turboexpander Using Transfer Matrix Method," *Lecture Notes in Mechanical Engineering*, no. January, pp. 129–140, 2021.

[35] T. Y. Yukio Ishida, *Related Titles Principles of Turbomachinery Critical Component Wear in Heavy Duty Engines Machinery Vibration and Rotordynamics Handbook of Noise and Vibration Mechanical Vibrations : Active and Passive Control*, 2012.

[36] R. Yang, Y. Jin, L. Hou, and Y. Chen, "Advantages of pulse force model over geometrical boundary model in a rigid rotor–ball bearing system," *International Journal of Non-Linear Mechanics*, vol. 102, pp. 159–169, 2018. [Online]. Available: https://doi.org/10.1016/j.ijnonlinmec.2018.03.011

[37] H. Q. Guan, K. Feng, Y. L. Cao, M. Huang, Y. H. Wu, and Z. Y. Guo, "Experimental and theoretical investigation of rotordynamic characteristics of a rigid rotor supported by an active bump-type foil bearing," *Journal of Sound and Vibration*, vol. 466, p. 115049, 2020. [Online]. Available: https://doi.org/10.1016/j.jsv.2019.115049

[38] C. Baum, H. Hetzler, S. Schröders, T. Leister, and W. Seemann, "A computationally efficient nonlinear foil air bearing model for fully coupled, transient rotor dynamic investigations," *Tribology International*, vol. 153, no. May 2020, 2021.

[39] Y. Yuan, R. Chen, and P. Li, "Trim investigation for coaxial rigid rotor helicopters using an improved aerodynamic interference model," *Aerospace Science and Technology*, vol. 85, pp. 293–304, 2019. [Online]. Available: https://doi.org/10.1016/j.ast.2018.11.044

[40] L. Li, M. Chen, F. Wang, and A. Xu, "The Influence of Rotor Adjustment Parameters on the Dynamic Balance of a Scale-Model Rigid Variable Speed Rotor," *Applied Sciences (Switzerland)*, vol. 12, no. 23, 2022.

[41] M. Rezaee, M. Mohammad Ettefagh, and R. Fathi, "Dynamics and stability of non-planar rigid rotor equipped with two ball-spring autobalancers," *International Journal of Structural Stability and Dynamics*, vol. 19, no. 2, pp. 1–27, 2019.

[42] R. Siva Srinivas, R. Tiwari, and C. Kannababu, "Application of active magnetic bearings in flexible rotordynamic systems – A state-of-the-art review," *Mechanical Systems and Signal Processing*, vol. 106, pp. 537–572, 2018. [Online]. Available: https://doi.org/10.1016/j.ymssp.2018.01.010

[43] R. Tiwari and P. Kumar, "An innovative virtual trial misalignment approach for identification of unbalance, sensor and active magnetic bearing misalignment along with its stiffness parameters in a magnetically levitated flexible rotor system," *Mechanical Systems and Signal Processing*, vol. 167, no. PA, p. 108540, 2022. [Online]. Available: https://doi.org/10.1016/j.ymssp.2021.108540

[44] J. Liu, C. Tang, and G. Pan, "Dynamic modeling and simulation of a flexible-rotor ball bearing system," *JVC/Journal of Vibration and Control*, vol. 28, no. 23-24, pp. 3495–3509, 2022.

[45] S. Ran, Y. Hu, and H. Wu, "Design, modeling, and robust control of the flexible rotor to pass the first bending critical speed with active magnetic bearing," *Advances in Mechanical Engineering*, vol. 10, no. 2, pp. 1–13, 2018.

[46] R. Ebrahimi, M. Ghayour, and H. M. Khanlo, "Nonlinear dynamic analysis and experimental verification of a magnetically supported flexible rotor system with auxiliary bearings," *Mechanism and Machine Theory*, vol. 121, pp. 545–562, 2018. [Online]. Available: https://doi.org/10.1016/j.mechmachtheory.2017.11.018

[47] I. Pavlenko, A. Verbovyi, C. Neamţu, V. Ivanov, O. Ciszak, and J. Trojanowska, "Fractional-order mathematical model of single-mass rotor dynamics and stability," *Alexandria Engineering Journal*, vol. 76, pp. 91–100, 2023.

[48] S. Lei and A. Palazzolo, "Control of flexible rotor systems with active magnetic bearings," *Journal of Sound and Vibration*, vol. 314, no. 1-2, pp. 19–38, 2008.

[49] P. C. Hughes, "Spacecraft attitude dynamics," 2012.

[50] L. Atepor, "Vibration analysis and intelligent control of flexible rotor systems using smart materials," *Thesis*, no. October, 2010. [Online]. Available: http://theses.gla.ac.uk/593/

[51] R. Gustavsson, "Modelling and analysis of hydropower generator rotors," Ph.D. dissertation, Luleå tekniska universitet, 2005.

[52] M. Eissa and N. A. Saeed, "Nonlinear vibration control of a horizontally supported Jeffcott-rotor system," *JVC/Journal of Vibration and Control*, vol. 24, no. 24, pp. 5898–5921, 2018.

[53] A. K. Darpe, K. Gupta, and A. Chawla, "Transient response and breathing behaviour of a cracked Jeffcott rotor," *Journal of Sound and Vibration*, vol. 272, no. 1-2, pp. 207–243, 2004.

[54] M. A. AL-Shudeifat, "New backward whirl phenomena in intact and cracked rotor systems," *Journal of Sound and Vibration*, vol. 443, pp. 124–138, 2019.

[55] J. Jiang and H. Ulbrich, "Stability analysis of sliding whirl in a nonlinear Jeffcott rotor with cross-coupling stiffness coefficients," *Nonlinear Dynamics*, vol. 24, no. 3, pp. 269–283, 2001.

[56] F. Boy, *Modelling the Rotordynamics of Saturated Electrical Machines due to Unbalanced Magnetic Pull*. BoD–Books on Demand, 2020.

[57] M. P. Boyc, *Gas Turbine Engineering Handbook, Fourth Edition*, 2011.

[58] E. C. D. Nantes, "Dynamique Non Linéaire Des Rotors," Ph.D. dissertation, 2005.

[59] E. Swanson, C. D. Powell, and S. Weissman, "A practical review of rotating machinery critical speeds and modes," *Sound and Vibration*, vol. 39, no. 5, pp. 10–17, 2005.

[60] F. C. Nelson, "Rotor dynamics without equations," *International Journal of COMADEM*, vol. 10, no. 3, pp. 2–10, 2007.

[61] T. D. Canonsburg, "Rotordynamic Analysis Guide," *Knowledge Creation Diffusion Utilization*, vol. 15317, no. April, pp. 724–746, 2009.

[62] M. L. Adams, *Rotating machinery vibration: From analysis to troubleshooting, second edition*, 2009.

[63] N. A. Saeed and M. Kamel, "Active magnetic bearing-based tuned controller to suppress lateral vibrations of a nonlinear Jeffcott rotor system," *Nonlinear Dynamics*, vol. 90, no. 1, pp. 457–478, 2017.

[64] A. Alsaleh, H. M. Sedighi, and H. M. Ouakad, "Experimental and theoretical investigations of the lateral vibrations of an unbalanced Jeffcott rotor," *Frontiers of Structural and Civil Engineering*, vol. 14, no. 4, pp. 1024–1032, 2020.

[65] H. Yao, Y. Cao, Z. Ding, and B. Wen, "Using grounded nonlinear energy sinks to suppress lateral vibration in rotor systems," *Mechanical Systems and Signal Processing*, vol. 124, pp. 237–253, 2019. [Online]. Available: https://doi.org/10.1016/j.ymssp.2019.01.054

[66] N. A. Saeed and A. Kandil, "Lateral vibration control and stabilization of the quasiperiodic oscillations for rotor-active magnetic bearings system," *Nonlinear Dynamics*, vol. 98, no. 2, pp. 1191–1218, 2019. [Online]. Available: https://doi.org/10.1007/s11071-019-05256-3

[67] M. A. Mokhtar, A. Kamalakar Darpe, and K. Gupta, "Investigations on bending-torsional vibrations of rotor during rotor-stator rub using Lagrange multiplier method," *Journal of Sound and Vibration*, vol. 401, pp. 94–113, 2017. [Online]. Available: http://dx.doi.org/10.1016/j.jsv.2017.03.026

[68] C. Liu and D. Jiang, "Torsional vibration characteristics and experimental study of cracked rotor system with torsional oscillation," *Engineering Failure Analysis*, vol. 116, no. July, p. 104737, 2020. [Online]. Available: https://doi.org/10.1016/j.engfailanal.2020.104737

[69] B. Xiang and W. Wong, "Electromagnetic vibration absorber for torsional vibration in high speed rotational machine," *Mechanical Systems and Signal Processing*, vol. 140, p. 106639, 2020. [Online]. Available: https://doi.org/10.1016/j.ymssp.2020.106639

[70] J. HONG, P. YU, Y. MA, and D. ZHANG, "Investigation on nonlinear lateral-torsional coupled vibration of a rotor system with substantial unbalance," *Chinese Journal of Aeronautics*, vol. 33, no. 6, pp. 1642–1660, 2020.

[71] Y. Cao, H. Yao, J. Dou, and R. Bai, "A multi-stable nonlinear energy sink for torsional vibration of the rotor system," *Nonlinear Dynamics*, vol. 110, no. 2, pp. 1253–1278, 2022. [Online]. Available: https://doi.org/10.1007/s11071-022-07681-3

[72] D. Srikrishnanivas, "Rotor Dynamic Analysis of RM12 Jet Engine Rotor using ANSYS," *Master's Degree Thesis*, pp. 1–78, 2012.

[73] H. Sugimoto, M. Miyoshi, and A. Chiba, "Axial Vibration Suppression by Field Flux Regulation in Two-Axis Actively Positioned Permanent Magnet Bearingless Motors with Axial Position Estimation," *IEEE Transactions on Industry Applications*, vol. 54, no. 2, pp. 1264–1272, 2018.

[74] G. Nan, M. Tang, E. Chen, and A. Yang, "Nonlinear dynamic mechanism of rolling element bearings with an internal clearance in a rotor-bearing system," *Advances in Mechanical Engineering*, vol. 8, no. 11, pp. 1–9, 2016.

[75] M. Tiwari, K. Gupta, and O. Prakash, "Effect of radial internal clearance of a ball bearing on the dynamics of a balanced horizontal rotor," *Journal of Sound and Vibration*, vol. 238, no. 5, pp. 723–756, 2000.

[76] P. H. Jain and S. P. Bhosle, "Analysis of Effects of Radial Clearance and Unbalance on Vibration Responses of a Rotor-Bearing System," *International Journal of Engineering Trends and Technology*, vol. 70, no. 1, pp. 327–347, 2022.

[77] J. J. Sinou and F. Thouverez, "Experimental study of a flexible rotor and its dependency on the rolling-bearing temperature," *International Journal of Rotating Machinery*, vol. 2006, pp. 1–8, 2006.

[78] G. Scurria, Leoluca and Bertini, Leonardo and Heirman, "Development of modeling techniques for rolling element bearings," *UNIVERSITÀ DI PISA*, 2016.

[79] A. G. M. Michell, A. Kingsbury, and A. Their, "Fundamentals of Thrust Bearings," *Hydrodynamic Lubrication*, pp. 47–61, 2006.

[80] ALBERT KINGSBURY, "THRUST-BEARING." Tech. Rep. [Online]. Available: https://patents.google.com/patent/US1102276A/en

[81] A. Guo, X. Wang, J. Jin, D. Y. Hua, and Z. Hua, "Experimental test of static and dynamic characteristics of tilting-pad thrust bearings," *Advances in Mechanical Engineering*, vol. 7, no. 7, pp. 1–8, 2015.

[82] S. Berger, O. Bonneau, and J. Frêne, "Influence of axial thrust bearing defects on the dynamic behavior of an elastic shaft," *Tribology International*, vol. 33, no. 3-4, pp. 153–160, 2000.

[83] O. V. Antonova, A. I. Borovkov, Y. Y. Boldyrev, and I. B. Voynov, "Optimum design of hydrodynamic thrust bearings with Rayleigh's pocket profiles," *8th International Conference on Computational Methods for Coupled Problems in Science and Engineering, COUPLED PROBLEMS 2019*, pp. 434–440, 2021.

[84] A. F. Storace, D. Sood, J. P. Lyons, and M. A. Preston, "Integration of magnetic bearings in the design of advanced gas turbine engines," *Proceedings of the ASME Turbo Expo*, vol. 2, no. October 1995, 1994.

[85] M. Granström, "Design and Analysis of a 1-DOF magnetic bearing," 2011.

[86] J. Lauridsen, "Control Design of Active Magnetic Bearings for Rotors Subjected to Destabilising Seal Forces-Theory and Experiment," *Citation*, 2017. [Online]. Available: www.mek.dtu.dk

[87] S. Marx and C. Nataraj, "Suppression of base excitation of rotors on magnetic bearings," *International Journal of Rotating Machinery*, vol. 2007, 2007.

[88] I. Arredondo, J. Jugo, and V. Etxebarria, "Modeling and control of a flexible rotor system with AMB-based sustentation," *ISA Transactions*, vol. 47, no. 1, pp. 101–112, 2008.

[89] D. N. Nagarkar and Z. J. Khan, "Wind Power Plant Using Magnetic Levitation Wind Turbine," *International Journal of Engineering and Innovative Technology (IJEIT)*, vol. 3, no. 1, pp. 324–326, 2013.

[90] B. Bou-Saïd, G. Grau, and I. Iordanoff, "On nonlinear rotor dynamic effects of aerodynamic bearings with simple flexible rotors," *Journal of Engineering for Gas Turbines and Power*, vol. 130, no. 1, pp. 0–9, 2008.

[91] M. Nagesh, "Rotordynamic Design Analysis of a Squeeze Film Damper Test Rig," 2017. [Online]. Available: http://rave.ohiolink.edu/etdc/view?acc_num=ucin14915608677634

[92] J. Nelson, HD and McVaugh, "The dynamics of rotor-bearing systems using finite elements," pp. 98(2): 593–600, 1976.

[93] G. Genta, "Whirling of unsymmetrical rotors: A finite element approach based on complex co-ordinates," *Journal of Sound and Vibration*, vol. 124, no. 1, pp. 27–53, 1988. [Online]. Available: http://dx.doi.org/10.1016/S0022-460X(88)81404-4

[94] M. Boiangiu, V. Ceausu, and C. D. Untaroiu, "A transfer matrix method for free vibration analysis of Euler-Bernoulli beams with variable cross section," *JVC/Journal of Vibration and Control*, vol. 22, no. 11, pp. 2591–2602, 2016.

[95] N. O. MYKLESTAD, "A New Method of Calculating Natural Modes of Uncoupled Bending Vibration of Airplane Wings and Other Types of Beams," *Journal of the Aeronautical Sciences*, vol. 11, no. 2, pp. 153–162, 1944.

[96] S. Zhou and J. Shi, "Active balancing and vibration control of rotating machinery: A survey," *Shock and Vibration Digest*, vol. 33, no. 5, pp. 361–371, 2001.

[97] Z. Dakel, "Stabilité et dynamique non linéaire de rotors embarqués," Ph.D. dissertation, Lyon, INSA, 2014.

[98] M. Lalanne and G. Ferraris, "Rotordynamics prediction in engineering," *(No Title)*, 1998.

[99] S. Appliqu and I. Toulouse, "Muhammad Rizwan SHAD Modélisation et Analyse du Comportement Dynamique Non-linéaire des Rotors Modeling and Analysis of Nonlinear Dynamic Behavior of Rotors," 2011.

[100] S. Ali, "La rétro-conception de composants mécaniques par une approche" concevoir pour fabriquer"," Ph.D. dissertation, Université de Technologie de Troyes, 2015.

[101] V. Raja and K. J. Fernandes, *Reverse engineering: an industrial perspective*. Springer Science & Business Media, 2007.

[102] HEXAGON, "PC-DMIS - Manuel de formation Niveau I," 2016.

[103] D. Systems, "User Guide Geomagic Design X," no. November, 2013. [Online]. Available: www.geomagic.com/

[104] M. A. . R2, "Advanced Analysis Guide," *ANSYS® Academic Research Mechanical*, no. January, 2019.

[105] J. Samuelsson, "Rotordynamisk analys av 3D-modellerad gasturbinrotor i ANSYS Rotor dynamic analysis of 3D-modeled gas turbine rotor in ANSYS," 2009.

[106] Ansys, "Workbench User ' s Guide 2021-R2," no. July, 2021.

[107] B. Grunwald, "Vibration analysis of shaft in solidworks and ansys," 2018.

[108] H. I. Mansoora, M. Al-Shammari, and A. Al-Hamood, "Theoretical analysis of the vibrations in gas turbine rotor," in *IOP Conference Series: Materials Science and Engineering*, vol. 671, no. 1. IOP Publishing, 2020, p. 012157.

[109] A. inc., "Element Reference," vol. 15317, no. November, p. 9, 2010.

[110] J.-S. Choi, D. K. McLaughlin, and D. E. Thompson, "Experiments on the unsteady flow field and noise generation in a centrifugal pump impeller," *Journal of sound and vibration*, vol. 263, no. 3, pp. 493–514, 2003.

[111] A. Namiranian, "3d simulation of a 5mw wind turbine," 2011.

[112] H. Park, J. Roh, K. cheol Oh, H. Cho, and J. Kim, "Modeling and optimization of water mist system for effective air-cooled heat exchangers," *International Journal of Heat and Mass Transfer*, vol. 184, p. 122297, 2022.

[113] A. Fluent *et al.*, "Ansys fluent theory guide," *Ansys Inc., USA*, vol. 15317, pp. 724–746, 2011.

[114] Y. Liu, "A cfd study of fluid-structure interaction problems for floating offshore wind turbines," 2018.

[115] A. AMOUR and N. MENASRI, "Transient numerical simulation of a large-sized cement-mill fan for performance prediction." *Mechanika*, vol. 29, no. 1, 2023.

Abstract

Rotor dynamics is an important aspect of the design or analysis of any type of rotating machine, as various types of vibrations appear in this mechanical system when the rotor is turned on, which can limit performance or easily lead to disaster. Therefore, the dynamic analysis of the rotor is necessary to ensure proper operation by providing accurate knowledge of the vibration behavior of the rotor system. In this study, scientific techniques for modeling and simulating the vibrations of a rotating system are presented. The equations of vibration motion of the rotor are determined using the Lagrange energy method.

The centrifugal fan installed at the cement factory was selected to be of the FN280 type, equipped with a single wheel with blades mounted on the shaft supported by two bearings. Due to the fact that the manual solution of the equations of motion characterizing the dynamic analysis is considered a difficult task, the dynamic analysis of the cement fan FN280 using the finite element method was performed by the code ANSYS. The various components of the fan are designed using SolidWorks, except for the blade. Due to the lack of design data for it, we resorted to reverse engineering technology, which is also called reverse design. To obtain a 3D model of the blade, we used a CMM machine to scan the blade, and the fan was assembled and a dynamic analysis of the rotor was performed using the ANSYS Workbench. We determined the natural frequencies, extracted the critical speed by means of the Campbell diagram and mode shapes, and also studied the effect of the worn blades on dynamic behavior. In addition, a harmonic response analysis was performed in both cases.

FSI simulation was also applied to the fan to estimate the loads resulting from unsteady flow. This simulation process is carried out using the ANSYS Workbench, which integrates flow simulation and transient analysis simulation using a one-way coupling approach. This approach was chosen because there is very weak interaction between the structural domain and the fluid. The purpose of this simulation is to verify the ability to make a preliminary estimate of the fatigue limit and the effect of pressure loads applied to the structure resulting from unsteady flow on the life of the fan. Results showed that air loads have a negligible effect on fan life.

Résumé

La dynamique du rotor est importante dans la conception ou analyses de tout type de machine tournante, car lors de fonctionnement du rotor, divers types de vibrations apparaissent dans ce système mécanique, ce qui peut limiter les performances ou facilement conduire à un désastre. Par conséquent, l'analyse dynamique du rotor est nécessaire pour garantir un bon fonctionnement en fournissant une connaissance précise du comportement vibratoire du système rotor. il présente des techniques scientifiques de modélisation et de simulation des vibrations d'un système tournant. Les équations du mouvement vibratoire du rotor sont déterminées à l'aide de la méthode énergétique de Lagrange.

Le ventilateur centrifuge installé dans la cimenterie a été choisi comme type FN280, doté d'une roue aubagés montée sur un arbre supporté par deux roulements, sachant que solution manuelle des équations de mouvement caractérisant l'analyse dynamique de système est une tâche difficile, l'analyse dynamique du ventilateur ciment FN280 a été réalisée en utilisant la méthode des éléments finis par le Code ANSYS. Les différents composants du ventilateur ont été conçus sous SolidWorks, à l'exception de la pale nous n'avions pas de données de conception, nous avons eu recours à la technologie de rétro-ingénierie, également appelée conception inversée, pour obtenir un modèle tridimensionnel (CAD) de la pale à l'aide d'une machine MMT pour scanner la pale, assemblez le ventilateur et effectuez une analyse dynamique à l'aide ANSYS WorkBench; nous avons déterminés les fréquences naturelles, et extraction les vitesses critiques en utilisant le diagramme de Campbell, les modes du ventilateur et nous avons étudié l'effet de l'usure des pales sur le comportement dynamique. De plus, une analyse des réponses harmoniques ont étés réalisées dans les deux cas.

La simulation FSI a été également appliquée au ventilateur afin d'estimer les charges résultant d'un écoulement instable. Ce processus de simulation est réalisé à l'aide ANSYS WorkBech, qui intègre la simulation de flux et la simulation d'analyse transitoire en utilisant une approche de couplage unidirectionnel.Cette approche a été choisie car il existe une très faible interaction entre le domaine structural et le fluide. Le but de cette simulation est de vérifier la capacité à faire une estimation préliminaire de la limite de fatigue et de l'effet des charges de pression appliquées à la structure résultant d'un écoulement instable sur le la vie du fan. Les résultats ont montré que les charges d'air ont un effet négligeable sur la durée de vie du ventilateur.

ملخص

تعتبر ديناميكيات الدوار من الامور المهمة في تصميم او تحليل أي نوع من الآلات الدوارة ، حيث تظهر أنواع مختلفة من الاهتزازات في هذا النظام الميكانيكي عند تشغيل الدوار ، مما قد يحد من الأداء أو يمكن أن يؤدي بسهولة إلى كارثة. لذلك ، يعد التحليل الديناميكي للدوار ضروريا لضمان التشغيل السليم من خلال توفير معرفة دقيقة بالسلوك الاهتزازي لنظام الدوار .في هذه الدراسة ، يتم تقديم تقنيات علمية لنمذجة ومحاكاة اهتزازات النظام الدوار. يتم تحديد معادلات الحركة الاهتزازية للدوار باستخدام طريقة طاقة لاغرانج.

تم اختيار مروحة الطرد المركزي المثبتة في مصنع الأسمنت من نوع FN280 ، والمجهزة بعجلة واحدة ذات شفرات مثبتة على العمود المدعوم بمحملين. نظرا لحقيقة أن الحل اليدوي لمعادلات الحركة التي تميز التحليل الديناميكي يعتبر مهمة صعبة، فقد تم إجراء التحليل الديناميكي لمروحة الأسمنت FN280 باستخدام طريقة العناصر المحدودة بواسطة برنامج ANSYS . تم تصميم المكونات المختلفة للمروحة باستخدام SOLIDWORKS ، باستثناء شفرة. لعدم وجود بيانات تصميم لها، لذلك لجأنا إلى تقنية الهندسة العكسية ، والتي تسمى أيضا التصميم العكسي ، للحصول على نموذج ثلاثي الأبعاد للشفرة قمنا باستخدام آلة CMM لمسح الشفرة وتم تجميع المروحة وإجراء التحليل الديناميكي للدوار باستخدام منصة ANSYS WORKBENCH. حددنا الترددات الطبيعية, واستخرجنا السرعات الحرجة عن طريق مخطط كامبل وأشكال الوضع, ودرسنا ايضا تأثير الشفرة المتأكلة على السلوك الديناميكي. بالإضافة إلى ذلك ، تم إجراء تحليل الاستجابة التوافقية في كلتا الحالتين.

كما تم اجراء محاكاة FSI على المروحة من أجل تقدير الأحمال الناتجة عن التدفق غير المستقر. حيث يتم إجراء عملية المحاكاة هذه باستخدام ANSYS WORKBENCH ، الذي يدمج محاكاة التدفق ومحاكاة التحليل العابر باستخدام نهج اقتران أحادي الاتجاه وتم اختيار هذا النهج لوجود تفاعل ضعيف جدا بين المجال الهيكلي والسائل. الهدف من هذه المحاكاة، هو التحقق من القدرة على عمل تقدير أولي لحد التعب وتأثير أحمال الضغط المطبقة على بنية المروحة الناتجة عن التدفق غير المستقر على حياة المروحة. أظهرت النتائج أن أحمال الهواء لها تأثير على عمر المروحة ، اظهرت النتائج ان احمال الهواء لها تاثير ضئيل على عمر المروحة.